

Lawrence Berkeley National Laboratory

Recent Work

Title

Evaluation of alternative horizontal well designs for gas production from hydrate deposits in the Shenhu area, South China Sea

Permalink

<https://escholarship.org/uc/item/6wj065xm>

ISBN

9781617388866

Authors

Zhang, K
Moridis, GJ
Wu, N
[et al.](#)

Publication Date

2010

DOI

10.2118/131151-ms

Peer reviewed

**Evaluation of the Performance of the Oceanic Hydrate
Accumulation at
Site NGHP-02-09 in the Krishna-Godavari Basin During a
Production Test and During Single and Multi Well Production
Scenarios**

George J. Moridis^{1,2}, Matthew T. Reagan^{1*}, Alejandro F. Queiruga¹, and
Ray Boswell³

¹: *Energy Geosciences Division, Lawrence Berkeley National
Laboratory, Berkeley, CA 94720, USA*

²: *Petroleum Engineering Department, Texas A&M University, College
Station, TX 77843, USA*

³: *U.S. Department of Energy, National Energy Technology Laboratory,
Pittsburgh PA 15236, USA*

**: Corresponding author.*

Keywords: Gas hydrates, geomechanical analysis, reservoir
simulation, India National Gas Program

Abstract

The objective of this study is to quantify, by means of numerical simulation, the response of the complex system of gas hydrate accumulations at Site NGHP-02-09, Krishna-Godavari Basin, Indian Ocean, to different production conditions, and to determine the technical feasibility of gas production through depressurization-induced dissociation. The study assesses the suitability of the site for a long-term production test involving a single vertical well, and the long-term potential of the deposit under full-field production using a system of multiple vertical wells. We simulate gas and water flow, estimate the production performance of the accumulation and separately investigate the corresponding geomechanical response of the system. Results indicate that production from Site NGHP-02-09 under the conditions of a long-term field test involving a single vertical well is technically feasible and can yield high gas production rates. However, an inability to fully isolate the water bearing zones results in production that is largely from dissolved gas rather than hydrate dissociation and is thus burdened by excessive water production. Given the estimated physical properties of the reservoir system, Site NGHP-02-09 does not appear to be a promising location for a single-well field test of gas production, but may be a promising production target for full-field production operations using a multi-well system in which exterior wells can mitigate water inflows to allow interior wells to more effectively depressurize the formation and capture methane from

44gas hydrate dissociation. Geomechanical issues need to be carefully
45considered as significant displacements are possible, which can be
46challenging to well construction and stability.

47

48**1. Introduction**

49**1.1. Background**

50The present study focuses on the analysis of a particular oceanic
51hydrate accumulation in the Krishna-Godavari Basin (hereafter referred
52to as the KG Basin) off the eastern coast of India, and its evaluation as
53a potential energy source and a hydrocarbon gas production target.
54More specifically, the hydrate deposit under investigation is located at
55Site NGHP-02-09 in the KG Basin that was recently drilled and cored
56during the National Gas Hydrate Program Expedition 02 (NGHP-02) that
57was conducted from 3-March-2015 to 28-July-2015 (Figure 1).

58The NGHP-02 expedition involved participation and support by a large
59international team representing several government and private
60organizations and included a wide range of investigations. NGHP-02
61downhole logging, coring and formation pressure testing confirmed the
62presence of large, highly saturated, gas hydrate accumulations in
63coarse-grained sand-rich depositional systems throughout the KG Basin
64within the regions defined during NGHP-02 as Area-B, Area-C, and
65Area-E (Figure 1). The existence of a fully developed gas hydrate
66petroleum system was established in Area-C of the KG Basin with the
67discovery of a large slope-basin interconnected depositional system,
68including a sand-rich, gas-hydrate-bearing channel-levee prospect at
69Sites NGHP-02-08 and -09 (*Collett et al., this issue*: Figure 2). The

elevation (measured from the ocean surface) of the upper surface of a system of Hydrate-Bearing Sediments (HBS) in the vicinity of these sites is described in the contour plots of Figure 3. Further analysis of cores and geophysical data collected at these sites yielded important information on the system stratigraphy and hydrate occurrence, revealing a very complicated geology that involved a HBS sequence consisting of alternating layers of high-porosity hydrate bearing sandy layers, hydrate-free intervals of the same water-saturated sandy medium and mud/clay interlayers (Figure 4). Investigation of all available data showed that the gas hydrates at these sites have very desirable reservoir properties, i.e., high gas hydrate saturation S_H and high intrinsic and effective permeability (k and k_{rel} , respectively), making these accumulations ideal candidate sites for consideration of future gas hydrate production testing. The present study focuses its effort on Site NGHP-02-09.

1.2. Objectives

The objective of this study is to quantify, by means of numerical simulation, the response of the complex system of hydrate accumulations at Site NGHP-02-09 to different production conditions in an effort to determine: a) the technical feasibility of gas production through depressurization-induced dissociation, b) the suitability of the site for a production test of several months duration involving a single

92vertical well, and c) the long-term potential of the deposit as a
93hydrocarbon resource in a full-field production operation using a
94system of multiple vertical wells. The study predicts fluid (gas and
95water) flow and production performance of the accumulation through
96the analysis of the coupled flow, thermal and phase-change processes
97that occur during the course of production. These production estimates
98do not incorporate the effects of progressive reservoir compaction
99during depressurization. The corresponding geomechanical response
100of the geologic system is calculated separately, using one-way
101coupling to draw inputs from the production model at certain moments
102in time to provide estimates of the in situ stress fields, formation
103compaction and seafloor subsidence.

104

105**1.3. Cases investigated in this study and general approach**

106We investigated a total of 4 different cases that involved different
107geometries and production scenarios. These were the following:

- 108 (1) The reference case, hereafter referred to as *Case R*, which
109 describes production from a radially infinite-acting (*open*) system
110 using a single vertical well during a long-term (about 180 days)
111 field test. The infinite-acting nature of this system is defined by
112 radial boundaries located at a sufficiently large distance from the

113 single vertical well called by the test design that their conditions
114 and properties remain time-invariant during the test period.
115 Through scoping calculations, we determined that a cylindrical
116 system with a radius $r = 2000$ m satisfies these conditions. Case
117 R is designed to address the issue of suitability of Site NGHP-02-
118 09 as the location for the planned long-term field test of gas
119 production from the hydrate accumulations of the KG Basin.

120 (2) *Case C1*, which describes production operations involving a
121 system of vertical wells on a regular grid. The effect of multiple
122 wells on a regular pattern creates conditions that approach no-
123 flow boundaries of the drainage area of individual wells in the
124 *interior* of the pattern. Here we provide production estimates by
125 assuming no-flow boundaries exist, meaning we model a single
126 interior well as a closed system with no external source of fluid
127 or heat. In Case C1, the distance between wells is 1000 m, the
128 radius of the domain (drainage area) of each interior well is $r =$
129 500 m. Case C1 is designed to evaluate the potential of the
130 hydrate deposit at Site NGHP-02-09 as a target for full-field
131 reservoir development through multiple wells.

132 (3) *Cases C2 and C3* are similar in concept to Case C1, from which
133 they differ in the domain radius ($r = 100$ m and 75 m,
134 respectively). The reason for investigating the three cases is to
135 evaluate the effect of well spacing on the gas production

136 performance from the NGHP-02-09 hydrate deposits under multi-
137 well production operations.

138 All the simulations were conducted using a single set of flow, thermal,
139 and geomechanical properties as reported in companion papers in this
140 Special Volume (ex., *Yoneda et al., this issue-a,b; Waite et al., this*
141 *issue*). Thus, the present study does not include a parametric
142 sensitivity analysis of the system production performance and overall
143 behavior in response to variations in the values of key flow, thermal
144 and geomechanical conditions and properties and does not consider
145 heterogeneity in any of these parameters. The enormous execution
146 time requirements (hundreds of thousands of supercomputer hours
147 and months of wall-clock time – see later discussion) needed to
148 complete the study of the four cases using the standard set of
149 properties and conditions precluded such an activity within the time
150 frame of this study. As a result of the computational costs, it was
151 infeasible to perform fully coupled simulations including geomechanics,
152 and the geomechanical response was estimated by post-processing
153 the results of the costly multiphase flow simulations.

154

1552. **System Description and Production Strategy**

156The discussion and analysis in this section is based on the data
157provided by the entire multinational team involved in the NGHP-02
158scientific expedition and the subsequent study (as summarized in
159Collett *et al.*, *this issue*; Boswell *et al.*, *this issue*; Kumar *et al.*, *this*
160*issue*). The methods used for the measurement and derivation of these
161data—and in the estimation of the relevant parameters, where direct
162measurements were not possible—are beyond the scope of this study
163and are not discussed in detail. Although a very large number of data
164were obtained in the course of the NGHP-02 expedition and the
165subsequent associated work, in the present modeling study we include
166and discuss only the data used in the simulations. The interested
167reader is directed to other relevant papers associated with the NGHP-
16802 expedition.

1692.1. **System description and geometry**

170The water depth at Site NGHP-02-09 of the KG Basin (see Figure 5) is
1712,219.5 m. The available information at the time of the study indicated
172that the hydrate accumulation at a promising location at that site is
173buried under a relatively thin layer of 214.9 m of mud below the sea
174floor (Figures 3, 4, and 5). The complex, 53.6 m-thick system of the
175HBS sequence is characterized by 49 alternating layers of (a) hydrate-
176rich sands, (b) clays (muds) that are nearly devoid of hydrates, and (c)

hydrate-free sands. Figure 5 shows a sketch of this system (based on the most recent data), and provides some basic information on the geology and geometry of the system such as the stratification, the thickness of the various layers and the texture of the corresponding sediments. The base of the gas hydrate stability zone (BGHSZ) is estimated to be well below the base of the hydrate accumulation, i.e., this is a thermodynamically stable system.

This complex, 53.6 m-thick hydrate-bearing system is overlain and underlain by very low-permeability boundaries, i.e., the mud overburden and assumed underburden, respectively (Figure 5). Based on experience gained in earlier studies (Moridis and Reagan, 2007a,b; Moridis et al., 2007; 2009a; 2013) and preliminary scoping calculations, the simulation domain extends from the ocean floor (the upper boundary of the domain) to a depth of 600 mbsf (Figure 5). This was necessary because the consideration of coupled flow, thermal, chemical and the one-way coupling to the geomechanical processes in this numerical study have effects that extend beyond the narrow confines of the hydrate-bearing sediments. The resulting dimensions of the simulation domain provided a representative reservoir description that (a) allowed heat and fluid exchanges between the deposit and its boundaries during the production period and (b) were shown to be sufficiently large to act as true boundaries for all processes considered in this study.

2002.2. Classification of the hydrate deposit at Site NGHP-02-09

201The analysis here hews very close to that of Moridis et al. (2013).
202Based on the geology and stratification indicated by Figure 5, the
203layered structure of the hydrate accumulation at Site NGHP-02-09
204appears to be a combination of Class 2 and 3 systems, but can be
205better considered a hybrid of two hydrate classes (Moridis and Reagan,
2062007a; 2007b Moridis et al., 2011; 2013): (a) Class 2, comprising a
207hydrate-bearing layer (HBL) overlying a zone of mobile water, and (b)
208Class 3, involving HBLs confined between two strata of near-zero
209permeability. Near the top of the HBL sequence, the features of a
210typical Class 2 deposit are dominant because of alternating HBL and
211hydrate free sands. The same can be said about the deeper mud
212interlayers (Figure 5), which are not impermeable. However, because
213of the very low permeability of the muds in the overburden,
214underburden and in the interlayers, the characteristics of a near-Class
2153 deposit are evident toward the bottom of the 53.6 m-thick system.
216Note that, although the water mobility in the mud layers is limited, it is
217not zero, and this has implications in the course of production that will
218be discussed later.

2192.3. Method of production and well design

220Gas production necessitates hydrate dissociation. Because of the
221geology at Site NGHP-02-09 (involving the low-permeability

222overburden, underburden and 14 mud layers in contact with HBLs),
223depressurization is the most effective dissociation strategy for reasons
224explained in detail by Moridis and Reagan (2007a) and Moridis et al.
225(2009b). This is accomplished by constant-pressure production
226(involving a constant bottomhole pressure P_w at the well), which is
227desirable because of its simplicity, its technical and economic
228effectiveness, the fast response of hydrates to the rapidly propagating
229pressure wave, the near-incompressibility of water, and the large heat
230capacity of water. Because of the high initial hydrate saturation S_H in
231the HBL and the very low permeability of the muds in the interlayers,
232the effective permeability k_{eff} at the onset of gas production can be
233very low, and constant-rate production is impractical because the
234associated pressure drop is rapid, large, and very difficult to control,
235with a near certainty of ice formation and severe restriction (or even
236blockage) of flow to the well. On the other hand, pure thermal
237stimulation is an unattractive option because of its limited and ever
238decreasing effectiveness and efficiency (Moridis and Reagan, 2007a).

239The use of horizontal wells was deemed impractical for the planned
240long-term field production test in the KG Basin due to the presence of
241alternating layers of highly permeable hydrate-free sand lenses and
242low intrinsic permeability mud interlayers, and the considerable
243cumulative thickness of the three types of units. Thus, vertical wells
244were used exclusively in the study. The simple well design uses a

245perforated interval that covers the entire 53.6 m-thickness of the
246hydrate-bearing interval. Alternative well completions were
247investigated and rejected that will be discussed later. A significant
248advantage of constant- P_w production is the elimination of the possibility
249of ice formation (with its consequent detrimental effects on
250permeability and gas production) through the selection of an
251appropriate $P_w > P_Q$ (where P_Q is the quadruple point pressure, 2.56
252MPa).

253The use of vertical wells and the absence of any information on
254heterogeneity at the site (in particular) and in the KG Basin (in general)
255led to the use of a cylindrical domain in (r,z) that can be modeled as a
2562D axisymmetric problem. In all studies, the well was located at $r = 0$
257with radius $r_w = 0.1$ m. For the various cases of production we
258investigated, scoping calculations indicated that the domain radii and a
259total thickness of $\Delta z = 600$ m were sufficient to provide constant
260condition boundaries by confirming that the pressure, thermal and
261geomechanical disturbance caused by the bottomhole pressure did not
262reach these boundaries for the duration of the study period.

263

2643. The Numerical Models and Simulation Approach

2653.1. Numerical methodology and codes

266The simulations are performed using the TOUGH+Millstone suite,
267comprised of the integral finite difference method simulator
268TOUGH+HYDRATE and the finite element method simulator Millstone.
269The TOUGH+HYDRATE code (T+H) can model all the known processes
270involved in the system response of natural CH₄-hydrates in complex
271geologic media (Moridis et al., 2014; Moridis and Pruess, 2014). T+H is
272a fully compositional simulator, descended directly from the TOUGH2
273family of codes (Pruess et al., 1999; Pruess, 2003), and it accounts for
274heat and up to four mass components (i.e., H₂O, CH₄, CH₄-hydrate, and
275water-soluble inhibitors such as salts) that are partitioned among four
276possible phases (gas, aqueous liquid, ice, and hydrate). It can describe
27715 possible thermodynamic states (phase combinations) of the
278CH₄+H₂O system and can handle the phase changes, state transitions,
279strong nonlinearities and sharp fronts that are typical of hydrate
280dissociation problems. Because of the very large computational
281requirements that are the norm in hydrate problems, both a serial and
282a parallel version (Zhang et al., 2008) of the code were used in this
283study. The T+H code has been used for a wide range of investigations
284of gas production from hydrates in both oceanic deposits and in
285accumulations associated with the permafrost that cover the entire
286spectrum of hydrate types, i.e., Class 1 (Moridis et al., 2007), Class 2
287(Moridis and Reagan, 2007b; Moridis et al., 2011a; 2011b), Class 3
288(Moridis and Reagan, 2007a; Moridis et al., 2011c), and Class 4

289(Moridis and Sloan, 2007; Li et al., 2010; Moridis et al., 2011d). In
290addition, the code has been used extensively to model natural
291hydrates and environmental impacts (Thatcher et al., 2013; Marin-
292Moreno et al., 2015; Stranne et al., 2016). For this study, we activated
2933 components, 4 phases, and 4 equations to model systems containing
294water, methane, and salt partitioned over gas, liquid, hydrate, and ice
295phases.

296Geomechanical analysis of the new set of hydrate reservoirs is enabled
297by a new geomechanical simulation framework, Millstone (Moridis et
298al., 2017). Millstone solves the incremental stress formulation using
299the Finite Element Method with the standard Galerkin formulation with
300bilinear-quad nodal shape functions for displacement fields and Gauss
301point-centered stresses. A small-deformation linearized strain
302assumption is used at each increment, with elastic moduli that are
303functions of the flow variables. This code introduces two new key
304features: (1) use of a separate mesh for the mechanical solution,
305alleviating the frequent problem of the ill-conditioned linear systems;
306and, (2) formulations for plane-strain and axisymmetry using 2D
307elements (in addition to standard 3D Cartesian formulations). The
308Millstone code yields significant speed improvements by reducing
309system unknowns and improving the stability, conditioning and
310accuracy of the solution compared to earlier used geomechanical
311solvers based upon 3D formulations using one-volume-to-one-element

312coupling schemes. Millstone is typically operated embedded inside of
313the TOUGH+Hydrate simulation loop, wherein it solves the quasistatic
314balance of momentum inside of the nonlinear solution loop of the flow
315solver. The solver iterates between solving displacements and flow
316primary variables, performing interpolations of required fields back-
317and-forth between the two meshes, until convergence for each time
318step.

319The computational cost of the highly-detailed system precluded the
320use of the complete two-way coupling between the flow and
321geomechanics, in which both systems are solved at every step of the
322Jacobian system until convergence. Beyond adding more unknowns,
323the inclusion of geomechanics in a coupled simulation greatly
324increases the cost by both increasing the number of iterations per time
325step (the staggered scheme does not have quadratic convergence)
326and decreasing the size of viable time steps due to the increased
327difficulty of solving the nonlinear equations. A time step sequential
328scheme, in which the geomechanics is solved only once per time step,
329performs worse due to smaller time step requirements.

330Motivated by this problem, a two-stage simulation process was
331developed to estimate the geomechanical response with only one-way
332coupling. The time-varying pressure and saturation fields at snapshots

333from the flow simulation are used to solve the total stress and
334displacements. The complete analysis procedure has four stages:

3351. Preprocessing to generate meshes and input files,
3362. Running TOUGH+Hydrate on HPC resources to solve multiphase,
337 multicomponent flow,
3383. Running Millstone on workstation to solve displacements and
339 stresses resulting from depressurization and hydrate dissociation,
340 and
3414. Postprocessing to calculate additional quantities of interest and
342 generate plotting and visualization formats.

343In this methodology, there is no feedback from the stress distributions
344to the flow problem, and as a result, the production values do not
345reflect potential reduction in production rates due to progressive
346reservoir consolidation (see Boswell et al.-b, this issue). The solution of
347the mechanics is linear and quasistatic in absence of the flow effects,
348and thus each case can be solved in only ten minutes on a desktop
349workstation given the flow fields to provide the estimates presented
350here. The open source tough_convert post-processing utility (Queiruga,
3512018) is used in a standalone script for the Millstone simulator in this
352system.

353 A saturation dependent poroelastic constitutive response is used. The
354 stress update is linear elastic with respect to the displacements, and
355 the bulk and shear modulus depend on the hydrate saturation linearly
356 by the relations $K(S) = K_0 S + K_1(1 - S)$ and $G(S) = G_0 S + G_1(1 - S)$ (Rutqvist
357 and Moridis, 2009). The values K_0 and G_0 correspond to the hydrate-
358 free moduli of the sediments, and K_1 and G_1 are calculated based on
359 the *in situ* saturation and field-determined elastic moduli. Plastic
360 yielding is not included in the stress integration, but the value of the
361 Drucker-Prager yield criteria is calculated as an estimate of possible
362 geochemical failure.

363 3.2. Domain dimensions and discretization

364 Very fine grids were used in the simulation of production from the
365 vertical well in all cases of this study. The 2D cylindrical (axisymmetric)
366 domains of the single vertical well problems in the four cases were
367 discretized as follows:

- 368 ● Case R (Reference, $r = 2000$ m): 452×525 in $(r, z) = 2.37 \times 10^5$
369 gridblocks
- 370 ● Case C1 ($r = 500$ m): 351×525 in $(r, z) = 1.84 \times 10^5$ gridblocks
- 371 ● Case C2 ($r = 100$ m): 239×525 in $(r, z) = 1.25 \times 10^5$ gridblocks
- 372 ● Case C3 ($r = 75$ m): 219×525 in $(r, z) = 1.15 \times 10^5$ gridblocks

373The meshes are aligned with the r - z axes. Drawing on past experience,
374the discretization along the z -axis within the 53.6 m of the HBS
375sequence had a maximum subdivision size $\Delta z = 0.1$ m, and ensured
376that each layer was subdivided in at least 3 segments regardless of the
377layer thickness (thus providing sufficient description of thermal
378gradients, and of heat and fluid flows). The same fine discretization
379along the z -axis was maintained in the first few subdivisions of the
380overburden and the underburden in contact with the HBS sequence
381(necessary to describe fluid and heat exchanges between the hydrate-
382bearing system and its boundaries during the endothermic dissociation
383process that feeds gas production). The discretization was non-uniform
384(with Δz increasing) in the mud of the overburden and underburden
385away from the top and bottom hydrate interfaces, i.e., near the top
386and bottom of the domain.

387Particular emphasis was given to fine discretization in the first 50 m
388along the r -axis, with 0.1 m radial subdivisions to 5 m, then linearly
389increasing Δr to 0.5 m at 50 m. Discretization past that point in the x -
390and y -directions was non-uniform, increasing logarithmically using a
391starting value of $\Delta r = 0.5$ m to 2,000 m (452 elements total). Past
392experience has indicated that such fine discretizations are necessary
393when steep thermal and pressure gradients are involved (Moridis et al.,
3942007). This high degree of refinement provided the level of detail
395needed to capture important processes near the wellbore and in the

entire hydrate-bearing zone, and especially in the thin interlayers that characterize the NGHP-02-09 systems.

Treating hydrate dissociation as an equilibrium reaction (Kowalsky and Moridis, 2007) and accounting for the effect of the salinity on hydrate dissociation, resulted in a system of about 9.48×10^5 , 7.36×10^5 , 5.0×10^5 and 4.6×10^5 equations for Cases R, C1, C2, and C3, respectively. The size of the problem precluded the use of desktop computational platforms (except for scoping calculations) and necessitated the use of the parallel version of T+H (pT+H) and high-performance computing resources. The full two-way coupling between flow and geomechanics was intractable as the coupled simulation requires a smaller timestep size and more iterations per timestep. The complexity of the geology of the system and of the coupled processes involved were so extreme that the flow simulations alone required between 900,000 to 2,000,000 timesteps (total) to cover the study periods of the various cases, and required hundreds of thousands of CPU-hours. The resources of LBNL Lawrence Livermore cluster farm were used to perform the pT+H simulations in this paper using 256 to 1,024 cores per submission.

The dual-mesh algorithm enables a coarser mesh to be used for the geomechanical response, where Millstone automatically handles the interpolation between the structured finite difference grid and unstructured finite element mesh. The final geomechanical results

418 were solved on an unstructured quadrilateral mesh with 48,954 nodes
419 and 48,777 elements, resulting in a system of 97,908 equations for
420 displacement updates and 195,108 additional stress degrees of
421 freedom. The mesh was structured near the well in the hydrate bearing
422 layer with square elements of side length of approximately 0.25 m to
423 capture the fine scale deformation. The post-processing-based one-
424 way coupling algorithm allowed the geomechanical results to be
425 calculated in approximately ten minutes for each case, for which only
426 considering the one-way effects allowed us to only use 20 intermediate
427 snapshots to compute the quasi-static deformation path.

428

429 **3.3. Baseline system properties and well description**

430 Key baseline hydraulic and thermal properties of the various geological
431 media in the various layers of the geologic model in Figure 5 were
432 provided from studies conducted by other members of the NGHP-02
433 expedition and are listed in Table 1. The corresponding geomechanical
434 properties are listed in Table 2. These values were used in the
435 simulation of all four cases. In the absence of relevant information, the
436 relative permeability and capillary pressure relationships and
437 corresponding parameters were approximations based on similarly
438 textured media or calculated from estimated effective permeabilities.
439 Note the relatively low thermal conductivity values measured from

440samples from Site NGHP-02-09. A possible explanation for the low
441values was the “watery” texture of the samples, as indicated by their
442very high porosity. Reasonable specific heat values were used for all
443the geologic media because data from direct measurements were
444unavailable.

445The same layer geometry is applied to the finite element mesh for the
446geomechanical properties. In this study, material is modeled using a
447rate-based formulation that does not consider plastic behavior. We
448considered two material groups: a sandy (hydrate-bearing or hydrate-
449free) medium, and a clay (mud) medium of the overburden,
450underburden and of the interlayers between the sandy HBS. The
451relevant geomechanical properties (Young’s modulus, Poisson’s ratio,
452and skeletal grain density for each medium) are listed in Table 2. We
453used values of the Young’s modulus that are linear functions
454(interpolations) of S_H in the hydrate-bearing media. Based on Rutqvist
455and Moridis (2009) and Rutqvist et al. (2009), a constant Poisson’s
456ratio was used, and the Biot coefficient was $b = 0.99$.

457Based on earlier studies that confirmed the validity of the approach
458(Moridis and Reagan, 2007a,b; Liu et al., 2017), we approximated
459wellbore flow by Darcian flow through a pseudo-porous medium
460describing the interior of the well. This pseudo-medium had $\phi = 1$, a
461very high $k = 5 \times 10^{-9} \text{ m}^2$ (= 5,000 Darcies), a capillary pressure $P_c = 0$,

462a relative permeability that was a linear function of the phase
463 saturations in the wellbore, and a low (but nonzero) irreducible gas
464 saturation $S_{irG} = 0.005$ to allow for the emergence of a free gas phase
465 in the well. While discretely treating the wellbore is required to solve
466 the flow, the structure is neglected in the mechanical analysis and the
467 coarser size of the mesh elements extends to the center axis of the
468 domain, using only the mechanical properties of the sediments.

469 **3.4. Initial and boundary conditions**

470 We determined the initial conditions in the reservoir by following the
471 initialization process described by Moridis and Reagan (2007a,b).
472 Based on initial measurements at the site, the geothermal gradient at
473 the site was $dT/dz = 5.82$ °C/100 meter with a seafloor temperature of
474 $T = 3.46$ °C (later updated—see *Waite et al. this issue*). The uppermost
475 and lowermost gridblock layers (i.e., at the top of the overburden at
476 the ocean floor, and at the bottom of the simulated domain) were
477 treated as constant-condition boundaries (maintaining constant P and
478 T). Knowing that a) the pressure $P = 25.45$ MPa at the ocean floor and
479 b) the pressure distribution with depth was hydrostatic (as is almost
480 universally the case in hydrate accumulations), we determined the
481 pressure P_T using the P , T - and salinity-adjusted water density. Then,
482 using P_T and the boundary temperatures T_T and T_B , the hydrostatic
483 gradient and representative thermal conductivity values, we

484determined the vertical P - and T -profiles in the domains by means of a
4851-D column simulation.

486The numerical representation of a constant bottomhole pressure P_w
487involves imposing a constant P_w at the topmost element of the well in
488the manner used to impose other constant-condition boundaries. In our
489study, the system behavior and performance was evaluated at a single
490value of P_w ($= 3.0$ MPa). Based on the results of the Moridis et al.
491(2014) study, this bottomhole pressure was the most desirable
492(although not necessarily practical or attainable under the conditions
493of the Site NGHP-02-09 deposit), and useful in providing the upper
494estimate of production. This P_w value is larger than the CH_4 -hydrate
495quadruple point pressure $P_Q = 2.56$ MPa, eliminating the possibility of
496ice formation and the corresponding adverse effect on k_{eff} , flow and
497production.

498The boundary conditions of the geomechanical system include an
499assumption of no-horizontal displacement at both sides along the r -
500axis, and a no-vertical displacement boundary at the bottom. The
501overburden pressure (at the top of the first HBL) is set at 27.70 MPa.
502The initial stress state of the geomechanical system is determined by
503solving for a set of discarded displacements that solve the static
504equilibrium of the domain given the mechanical loading conditions, the

505spatially-variably material properties, and the initial fluid pressures and
506saturation used for the flow simulation.

507

508**4. Results and Discussion**

509**4.1. Production performance in the reference Case R**

510Figure 6 shows the expected evolution of the hydrate dissociation
511(overall rate of gas release into the reservoir from hydrate dissociation)
512rate Q_D and of the gas production rate at the well, Q_P , as a result of the
513depressurization caused by the operation of a single vertical well at the
514center of the cylindrical infinite-acting domain. Although Q_P rises very
515fast to a high level (exceeding 5 MMSCFD in less than a month), even a
516cursory inspection of Figure 6 reveals a problem: Q_D is substantially
517smaller than Q_P , throughout the period of the test, indicating that
518hydrate dissociation is not the dominant source of the produced gas in
519this timeframe. Hydrate deposits that are promising targets for
520production are characterized by Q_D exceeding Q_P early in the
521production period, and their desirability increases with an increasing
522gap between the two. In the absence of free gas zones in the system,
523the only possible alternative source of gas is exsolution of CH_4
524dissolved in the aqueous phase of the deposit. Given the very small
525solubility of CH_4 in H_2O , this indicates that very large amounts of H_2O

526 need to be produced to provide the significant level of Q_P estimated by
527 the simulation, raising significant questions about the viability of such
528 an endeavor. The semi-log plot in Figure 7 shows the same Q_D and Q_P
529 results, but focused on the early-time behavior. It shows net hydrate
530 formation (denoted by the negative Q_D values) in the reservoir for the
531 first 20 days of production. This means that CH_4 dissolved in the
532 aqueous phase forms hydrate on the way to the well at a rate that
533 exceeds the hydrate dissociation at elsewhere in the reservoir. An
534 even more worrisome feature in Figures 6 and 7 is the declining trend
535 in Q_D as time advances: this is the opposite of what would be expected
536 in a desirable production target and is an indication of ineffective
537 depressurization.

538 Review of the composition of the produced fluids in Figure 8 provides
539 further evidence of the problem with this production test: gas dissolved
540 in the produced water amounts to almost 50% of the total methane
541 produced at the well. This means a very large water production rate is
542 needed to achieve the rate of methane production predicted by the
543 simulation. The cumulative volumes of methane produced and
544 hydrate-originating methane in the reservoir (V_D and V_P , respectively)
545 in Figure 9 depict clearly the increasing discrepancy between hydrate
546 dissociation and gas production at the well (with $V_D \ll V_P$). Further
547 evidence of the challenges facing a long-term production test at Site
548 NGHP-02-09 is provided by the free gas volume V_F in Figure 10, which

549reaches a plateau within 50 days from the onset of production, and
550actually appears to decline slowly after this time (hinting at the
551possibility of secondary hydrate formation capturing free gas within
552the reservoir). Hydrate deposits that are desirable production targets
553are characterized by an increasing V_F over time (at least until a large
554part of the resource is exhausted) that acts as the primary source of
555gas for production. The inability of V_F to increase with time (in addition
556to the low Q_D) is further evidence of ineffective depressurization.

557The water production results (Q_W and M_W) in Figure 11 confirm these
558problems and indicate the significant technical and economic
559challenge of moving the very large and increasing volumes of H_2O that
560are necessary to maintain the depressurization needed to support the
561production rate Q_P , mainly through transport of aqueous CH_4 in the
562produced water. The high level of Q_W and its non-declining (actually
563increasing) value with time even after $t > 180$ days is an indication of
564continuous inflow of H_2O from the boundaries. The water-to-gas ratio
565(WGR), $R_{WG} = M_W/V_P$, and the salt mass fraction X_S in the produced
566water (Figure 12) confirm the earlier observations, deductions and
567conclusions. WGR appears practically constant over time at a very high
568level (about 170 kg of H_2O per standard m^3 of CH_4) that is economically
569unsustainable and technically challenging (although perhaps feasible).
570The high and persistent WGR level during the duration of the test
571period is an additional indication of continuous inflow of H_2O from the

572 boundaries. The evolution of X_s over time provides further support to
573 the initial Q_D behavior—its value exceeding the natural salinity of
574 ocean water (0.035) is a clear evidence and confirmation of the net
575 hydrate formation identified in Figure 7, as hydrate formation in saline
576 water results in localized salinity increases as the hydrate crystal does
577 not admit salt. The fact that X_s remains above the 0.035 level indicates
578 a combination of limited hydrate dissociation, hydrate formation at
579 other locations, and inflow of ocean water from the boundaries, all of
580 which point toward ineffective depressurization.

581

582 **4.2. Spatial distributions of important parameters in the** 583 **reference Case R**

584 The pressure distributions in Figure 13 provide direct evidence of the
585 indications of ineffective depressurization surmised from the analysis
586 of the figures in Section 4.1. Thus, there appears to be practically no
587 change in the P -distribution past $t \geq 56$ days. Note the relatively thin
588 depressurization zone, indicative of a higher effective permeability
589 compared to its adjacent units. The depressurization band, however,
590 does not expand beyond the range seen at $t = 17$ days, thus further
591 supporting the conclusion of ineffective depressurization. As expected,
592 the largest pressure drop in the domain (depicted by the yellow-blue

range of color) occurs close to the vertical well at $r = 0$ and corresponds to hydrate dissociation there.

The T -distributions in Figure 14 are different in pattern than the P -distributions in Figure 13, but it is these differences that confirm the observations and conclusions drawn from the P -profile analysis and from the earlier results. At $t = 17$ days, there is a narrow band of lower temperature in the upper part of the HBS sequence (within layers 1 through 28 as shown on Figure 5), which indicates cooling caused by active hydrate dissociation. However, this temperature disturbance is attenuated at $t = 56$ days, and practically disappears after that time. This is an indication of water inflows from the infinite-acting radial boundaries, which counters the initial cooling and at the same time provides the pressure support observed in Figure 13. The limited dissociation discussed in Case R is further indicated by the absence of any noticeable change in the T -distributions for $t > 56$ days.

The evolution of the S_H and S_G distributions are shown in Figures 15 and 16, respectively. The hydrate saturation appears practically unchanged after $t \geq 56$ days, as does the distribution of gas, S_G . The limited occurrence of free gas (derived from dissociation) is consistent with the V_F results of Figure 10 and confirms both the observations of limited dissociation and its stagnation as time advances. In addition to poor dissociation performance, some localized formation of hydrate

615 occurs in the uppermost layers, resulting in hydrate saturations that
616 exceed the initial saturation (indicated by arrows in Figure 15). Further
617 proof is provided by the X_s distribution in the aqueous phase that is
618 shown in Figure 17: the absence of significant freshening of the water
619 and the limited footprint of the areas where X_s is different from the
620 background level are consistent with limited (or non-occurring)
621 dissociation, and is in agreement with all previous observations.

622 Figure 18 describes the pressure profile inside the well (i.e., along z at
623 $r = 0$) and provides clear evidence of the culprit for the ineffectiveness
624 of depressurization and the consequent limited hydrate dissociation.
625 Although there is no resistance to flow within the well casing (being in
626 essence an “infinite permeability” system, leading to an expectation of
627 a near-linear pressure decline in the well), there is no significant
628 pressure drop at any time below about $z = -241$ m. The obvious
629 inference is that there is a source of water at and above this level that
630 can easily replenish the water produced by the well, thus preventing
631 any pressure drop below this point. This source of water is the hydrate-
632 free sandy layers Aquo01 through Aquo10 (see Figure 5), which have
633 very high permeability (on the order of $k_r = 10^{-11} \text{ m}^2 = 10 \text{ D}$, Yoneda et
634 al. (this issue-b)), thus having enough capacity to resupply all the
635 water withdrawn by the well and preventing a pressure drop below the
636 $z = -241$ m (with Aquo10, at $z = -248$ m and with a thickness of nearly 7
637 m, capable of contributing significant flows) . In addition, the low-

638 permeability layers Mud01 through Mud05 ($-230 \text{ m} < z < -226 \text{ m}$)
639 separate the upper hydrate and aquifer layers and are reflected by the
640 near step-change in pressure within the reservoir below -226 m seen in
641 Figure 13. Consequently, effective depressurization is not possible
642 below this level.

643 **4.3. Conclusions drawn from the production performance in** 644 **Case R**

645 The results of the study indicate that gas production from Site NGHP-
646 02-09 under the conditions of a long-term field test involving a single
647 vertical well is technically feasible and can yield high gas production
648 rates. However, the high gas production is based mainly on exsolution
649 of dissolved gas rather than hydrate dissociation and thus necessitates
650 excessively large water production, the management of which appears
651 to be a technical challenge.

652 The conclusion from this analysis is that Site NGHP-02-09 is not a
653 promising location for a field test of gas production from the hydrate
654 deposits of the KG Basin. Despite encouraging conditions (high
655 permeability and hydrate saturation) and ample hydrate resources at
656 the site (with a combined thickness of HBLs in excess of 36 m and an
657 excellent permeability regime of these units), the presence and
658 attributes of the hydrate-free and extremely permeable aquifer layers
659 are sufficient to singlehandedly short-circuit the depressurization

process and preclude the consideration of Site NGHP-02-09 as a possible test location. In essence, such a test would be a demonstration of production more of exsolution of dissolved gas rather than of dissociation of hydrates. Note that attempts to isolate the Aqu10 layer by modifying the location of the perforated interval of the well (e.g., confining it to intervals above and below this layer) in several scoping simulations had no practical effect, with production behavior very similar to that of the fully perforated HBS sequence as there are still many sources of water inflow.

4.4. Production performance in Cases C1, C2 and C3

The importance of the assumed no-flow radial boundaries in Cases C1, C2 and C3 is amply demonstrated by the evolution of the corresponding gas release rates Q_D in Figure 19, which also includes the Q_D for Case R for comparison. The differences in both pattern and performance are notable. In all three cases, we observe an early surge of gas release at rates that are between 3 and 3.3 m³/s (9 and 10 MMSCFD) and are caused by the large initial driving force of depressurization, i.e., the difference ΔP between the bottomhole and the reservoir pressure in the vicinity of the well that is at its maximum at the beginning of production. Because the Aqu10 unit is now unable to function as a practically infinite source of water, depressurization is effective and leads to the large initial Q_D that occurs almost

682 immediately after the onset of production in the limited volumes of the
683 domains in Cases C2 and C3. In this first gas release, Q_D is higher for
684 the cases with reduced domain volumes because of stronger response
685 to depressurization, although the lack of enhancement from Case C2 to
686 C3 suggests there is a practical limit to tighter well spacing. The
687 response in the larger-volume domain of Case C1 is slower because of
688 the correspondingly larger mass of water in the Aqu10 unit. This is the
689 reason why the Q_D for Cases R and C1 initially coincide, with the point
690 of deviation at about $t = 20$ days marking the first effect of the closed
691 boundaries.

692 The initial spike in Q_D is followed by longer periods of large Q_D that
693 peak at similar levels of about 3 MMSCFD for Cases C2 and C3, but are
694 larger (peaking at about $4 \text{ m}^3/\text{s}$ or 12 MMSCFD by $t = 300 \text{ d}$) in the
695 larger system of Case C1. In this second gas release, Q_D increases with
696 an increasing domain volume because of an increasing mass of
697 dissociating hydrate. Although the driving force difference ΔP is
698 smaller, the effect of dewatering of the system leads to an effective
699 depressurization of the hydrate over a large volume of the reservoir,
700 significant dissociation and gas release. The peak in this second phase
701 of hydrate dissociation is followed by a continuous decline in Q_D that is
702 attributed to the reduction in the reservoir temperature (caused by the
703 endothermic nature of dissociation, which inhibits dissociation) and in
704 the driving force of dissociation, i.e., the difference between wellbore

705and reservoir P). The same behavior is more evident in Cases C2 and
706C3.

707The evolution of the gas production rate Q_p in cases C1, C2, and C3
708(Figure 20) follows a similar pattern as Q_D , and differs substantially
709from that in Case R in terms of pattern, magnitude and relationship to
710 Q_D . Q_p also exhibits the two-lobe pattern of Q_D in the C1, C2, and C3
711cases (Figure 20), with similar relationships of the relative magnitudes
712between the cases. Thus, the first surge of production peaks at about
713 $Q_p = 4.5, 6,$ and 6.5 MMSCFD in Cases C1, C2, and C3, respectively.
714The second (long term) surge of production peaks at about $Q_p = 8, 3.5,$
715and 3 MMSCFD in Cases C1, C2, and C3, respectively. The effective
716hydrate dissociation in these closed systems is demonstrated in the
717analysis of the origin of gas in Cases C1 and C3 (Figure 21), which now
718shows a far smaller contribution to Q_p from methane dissolved in the
719produced water than in Case R. Both the Q_p and Q_D results are positive
720indicators of the potential of the site as a target for multi-well
721production rather than as a test site. Note that these enhancements
722assume a degree of uniformity across the larger multi-well reservoir
723system and that these results reflect the performance of *inner wells*
724shielded from water inflow by outer wells in the pattern. Interference
725between wells due to unknown pathways or heterogeneities in hydrate
726dissociation could reduce the effectiveness of a multi-well pattern.

727The cumulative volumes of produced gas V_P in Figure 22 indicate (a)
728similar initial production in all closed-system cases, with deviations
729marking the beginning of exhaustion of the different hydrate masses
730(or severe reduction in dissociation) in the 3 systems, and (b) V_P that
731are consistently lower than that for Case R during the initial 200 days
732of the simulation. The evolution of free gas volume V_F in the three
733domains (Figure 23) also shows a striking difference from that in Case
734R and explains some of the V_P observations: V_F are now much larger by
735orders of magnitude, as released gas is stored in the reservoir, and is
736used as a source of gas for production. The severe reduction in hydrate
737dissociation (attributed to the causes discussed earlier) is evident in
738Cases 2 and 3, but has not yet begun during the production period in
739the larger system of Case 1. As expected, both V_P and V_F increase with
740an increased volume of the closed domain of the cases.

741The evolution of water production (rates Q_W and cumulative mass M_W in
742Figures 24 and 25, respectively) shows the clear production superiority
743of closed systems compared to Case R. Following an initial surge of
744very short duration, Q_W decreases continuously in all three cases (in
745contrast to the increasing Q_W in Case R), leading to M_W that are much
746smaller than those in Case R and posing a much easier water
747management problem that becomes easier as the reservoir volume
748corresponding to each well in the closed systems decreases. Thus, the
749attractiveness of the larger V_P in Case R is negated by the much larger

750 M_w , but Cases C1, C2, and C3 emerge as possible production options.
751This is further confirmed by the WGR in Figure 26, which indicates a
752generally improving gas vs. water regime in all three closed-system
753cases, and is consistent with promising production targets. Note the
754slight increase in the WGR for Cases 2 and 3 at late times, which is
755attributed to water inflows from the top (overburden and ocean floor)
756and bottom (deep subsurface) boundaries that are enhanced by the
757depressurized interior of the reservoir. This is confirmed by the pattern
758of X_s evolution in Figure 27, which exhibits the effect of active hydrate
759dissociation in the initial X_s decline (water *freshening*) that is caused by
760the release of salt free water from the hydrate dissociation. The X_s
761decline is faster where hydrate dissociation is at its most intense, i.e.,
762it is enhanced in decreasing system volumes. However, in the smaller
763volumes of Cases 2 and 3, there is a pattern reversal and an increase
764in X_s for $t > 300$ days (when hydrate dissociation is at its minimum and
765the system pressure is at its lowest), which is an indication of saline
766water inflows, as well as of hydrate regeneration in the reservoir.

767**4.5. Spatial distributions of important parameters in the Cases** 768**C1, C2, and C3**

769In Case C1, the pressure distributions in Figure 28 clearly indicate a
770more effective depressurization than in Case R. The thin band
771identified in Figure 13 is clearly discernible initially, but the lack of

inflows from the radial boundaries results in pressure drops over the entire reservoir depth interval that, as expected, continuously expand radially with time and are a positive indicator of production potential. The effective depressurization and its positive impact on hydrate dissociation in Case C1 is further demonstrated in the evolution of the T -distribution of Figure 29, which shows a continuous cooling of the system beyond the immediate wellbore and is another indicator of occurrence of the endothermic process of hydrate dissociation. Further confirmation of the enhanced hydrate dissociation in Case C1 (compared to that in Case R) is provided by the evolution of the S_H , S_G and X_S spatial distributions in Figures 30, 31 and 32, respectively. The footprint/occurrence of S_H indicates a continuously shrinking hydrate mass, which is by no means near exhaustion at the end of the 360-day production period. However, some localized hydrate reformation (indicated by arrows) still occurs, with local $S_H > S_{H,initial}$. This is accompanied by ever-expanding footprints of increasing S_G and decreasing X_S in the reservoir, as well as by increasing S_G and decreasing X_S levels, providing direct evidence of enhanced dissociation.

In Case C2, the system behavior is similar to that in Case C1, but far more intense. Thus, the pressure distributions in Figure 33 indicate a continuous and an even more effective depressurization, as depicted by larger pressure drops over a larger system volume. Similarly, the

795 evolution of the T -distribution in Figure 34 shows a continuous and
796 faster (than in case C1) cooling of the system that affects a larger
797 portion of the system volume, and is an indicator of intense hydrate
798 dissociation. Further confirmation of intense hydrate dissociation in
799 Case C2 (compared to that in Cases R and C1) is provided by the
800 evolution of the S_H , S_G , and X_S spatial distributions in Figures 35, 36 and
801 37, respectively. The footprint/occurrence of S_H indicates a
802 continuously shrinking hydrate mass. However, given the production
803 behavior discussed in the previous section, there is no indication of
804 hydrate exhaustion (only of mass reduction) at the end of the 540-day
805 production period. This explains the production behavior and
806 eliminates the possibility of exhaustion of hydrate as a possible reason
807 for the near-cessation of dissociation and the consequent severe
808 reduction in production at later times.

809 This explanation can be further strengthened by an inspection of the
810 spatial distributions in Figures 33 to 37, in addition to a re-evaluation
811 of the production results. Once again, closer inspection of the S_H
812 distribution at $t = 540$ days indicates localized increases in S_H (arrows).
813 The S_G distribution indicates gas exhaustion, as indicated by the
814 reduction in the S_G levels at $t = 540$ days, and is consistent with the V_F
815 results in Figure 23. At the same time, the footprints of X_S in the
816 reservoir, as well as the increasing X_S levels, providing direct evidence
817 of continuing (albeit localized) dissociation. All these results taken

818together indicate that there is no hydrate exhaustion in Case C2, and
819the reason for the significant reduction in gas release and production is
820that (a) the driving force of dissociation, i.e., the ΔP between well and
821reservoir, is now at a minimum and (b) the system temperature has
822fallen so much that further hydrate dissociation is not only severely
823reduced, but can also lead to localized hydrate reformation. This can
824also partly explain the increase in the salinity of the produced water
825observed in Figure 27.

826The evolutions over time in the spatial distributions of the same key
827parameters in Case C3 are very similar to those in Case C2, and will
828not be discussed in detail.

829

830**4.6. Conclusions drawn from the production performance in** 831**Cases C1, C2, and C3**

832The conclusion from the analysis of the closed systems in Cases C1 to
833C3 is that Site NGHP-02-09 may be a promising production target for
834full production operations despite its unsuitability as a location for a
835single vertical well test. However, this requires controlling the water
836inflows from the radial boundaries to increase the productivity of
837interior wells. For those interior wells of the multi-well pattern,
838depressurization can induce significant hydrate dissociation and gas

839production while water production can be manageable. The hydrate
840accumulations at this site seem to meet both an absolute criterion of
841high gas production and a relative criterion of manageable/low water
842production. Confounding costs and challenges include the need for
843installing lower-performing wells at the boundaries of the pattern that
844serve to control water influx at a single interior well. Larger arrays,
845though more expensive to construct, would offer more interior wells
846per exterior well.

847

848**5. Geomechanical system behavior**

849The geomechanical response was calculated for each of the cases
850discussed in the previous section using the one-way coupling process.
851The maximum strains found in the simulation domain for each of the
852cases is plotted in Figure 38. The evolution of the vertical
853displacements u_z along the z-axis (indicating uplift or subsidence) at
854the seafloor, top of the reservoir, and bottom of the reservoir are
855plotted in Figures 39. Snapshots of the displacement fields for each of
856the cases at three times are presented in Figures 40 to 42. The
857snapshots are zoomed in at the production zone clearly indicate
858increasing magnitudes as time advances, as well as a progressive
859contraction (“squeezing”) of the reservoir as the top subsides and the
860bottom is uplifted in response to depressurization. This is clearly

demonstrated in Figure 39, which shows the evolution of the maximum and minimum u_z displacements in the vicinity of the vertical wells in cases R, C1 and C2. The displacements in Case R are minimal: practically zero at the ocean floor, a slight uplift at the base of the accumulation because of the effect of the Aqu10 layer that prevents depressurization, and a slight subsidence at the top of the accumulation in response to the proximity of the location of the maximum pressure drop near the top of the well operating at a constant P_w . This minimal impact allows for the de-coupling of the geomechanical and production flow simulations that allow for tractable production simulations to be accomplished given the requirement for exceedingly fine reservoir discretizations. We recognize that in many systems with other characteristics, most notably more aggressive hydrate dissociation, full two-way coupling will be required to achieve more reliable production simulations.

The displacements in the closed systems in cases C1 and C2 are far more substantial, and increase with a decreasing radius (and volume of the reservoir portion served by the individual wells). The depressurization of the system is primarily isolated to the reservoir layers, and consequently the reservoir sediments exhibit the most pronounced deformation. Because the overburden does not deform significantly, the subsidence at the ocean floor in these cases for the interior wells closely follows that at the top of the accumulation, and

884reaches about 4 m and almost 9 m at the end of their production
885periods in Cases C1 and C2, respectively, at which levels they appear
886to stabilize. The underburden is pulled up towards the well from the
887fixed based, so that the uplift at the base of the Case C1 reservoir is
888about 0.55 m, which, when combined with the subsidence at the top,
889indicated clear contraction “squeezing” of the reservoir at the well.
890These results indicate that production simulations for these alternative
891cases will be optimistic in comparison to fully-coupled simulations of
892these multi-well cases, should such simulations become practically
893possible in the future.

894The u_z displacements at the base of the accumulation in Case 2 follow
895a different pattern. There is an initial uplift that reaches a maximum of
896about 0.55 m, but the severe and progressing depressurization in the
897case leads to a pattern reversal after about $t = 30$ days and a
898continuous decline in the uplift, ending in subsidence that begins at
899about $t = 270$ days and reaches very modest levels (0.2 m) at the end
900of the 540-production period. The displacement behavior in Cases C1
901and C2 may have important implications for the construction,
902completion and stability of the well, and may impose specific material
903requirements in order to meet the mechanical challenges posed by
904such behavior. Obviously, the situation can change significantly if
905production from Cases C1 and C2 ceases earlier than the production
906period of this study, and this is entirely possible because of the low

907 (and declining, and eventually uneconomical) Q_p level after a certain
908 point (see Figure 20).

909 Plasticity was not incorporated in the one-way calculations of the
910 geomechanical response, but the important stress factors were post-
911 processed to estimate regions of possible failure. In Figures 43 to 45,
912 the value of the Drucker-Prager yield criterion, a smooth version of the
913 Mohr-Coulomb yield criterion, is plotted in the reservoir case for each
914 region. Yield would be indicated by a criterion that is less than zero,
915 where zero is the yield surface itself. We do not use a hydrate-
916 dependent yield criterion and use only the cohesion of the hydrate-less
917 sediment everywhere to serve as a lower bound for the estimates.
918 Because of ineffective depressurization in Case R, the stresses are
919 limited. This not the case in cases C1 and C2, which show increasing
920 stress as depressurization becomes more effective with a decreasing
921 volume of the domain under investigation. In case C2 with the most
922 extreme depressurization, the hydrate-less sediments deform
923 significantly, with one region indicated yielding in the second layer
924 from the top, marked by a red circle in Figure 45. This is clearly
925 demonstrated in Figure 38, which shows the evolution of the maximum
926 and minimum ϵ_{zz} and ϵ_{rr} strains (over the reservoir volumes) over time.
927 The strains are minimal in Case R, but can be significant (and possibly
928 severe) in Case C2 where maximum depressurization and hydrate
929 dissociation occurs.

930The conclusion drawn from these results is that full-field production
931from the hydrate accumulations at Site NGHP-02-09 site needs to
932carefully consider geomechanical issues that can be challenging. The
933authors of this study are unable to authoritatively proffer an opinion on
934whether the geomechanical criterion of the reservoir desirability as a
935production target can be met because of lack of the required well
936construction expertise to address the issue, and because other issues
937(e.g., when production should cease, decision that can be driven by
938both Q_p and economic considerations) can affect the maximum
939displacements experienced during production. As noted, to render
940these simulations tractable, progressive compaction in the reservoir,
941and the implied decrease in permeability, were not incorporated into
942the estimates of gas and water flow rates. Thus, the overall production
943values estimated in this study should be a first order review of a highly
944complex system.

945

946**6. Overall conclusions**

947The following conclusions can be drawn from this study:

- 948 ● Gas production from Site NGHP-02-09 under the conditions of a
949 long-term field test involving a single vertical well is *technically*
950 *feasible* and can yield high gas production rates. However, the

951 high gas production is based mainly on exsolution of dissolved
952 gas rather than hydrate dissociation and is thus burdened by an
953 excessively large water production.

954 ● Given the properties and the geological model used in this study,
955 Site NGHP-02-09 does not appear to be a promising location for a
956 field test of gas production from the hydrate deposits of the KG
957 Basin because of the presence and attributes of the hydrate-free
958 and extremely permeable Aqu10 layer short-circuit the
959 depressurization process.

960 ● Site NGHP-02-09 may be a more promising production target for
961 a multi-well operation despite its unsuitability as a single-well
962 test location because the control of the water inflows by the
963 multi-well system promotes more effective depressurization
964 while keeping the water production within manageable limits.
965 These results suggest merit in further evaluation of economics of
966 full-field production of this reservoir. Such evaluation will need
967 also to incorporate the potentially significant geomechanical
968 effects on production for the system.

969 ● The geomechanical issues associated with production from the
970 hydrate accumulations at Site NGHP-02-09 need to be carefully
971 considered as significant displacements are possible, which can
972 be challenging to well construction and stability. Note that other
973 considerations (such as the point at which cessation of

974 production should occur, as dictated by economic and/or
975 technical reasons) can change significantly the severity of the
976 geomechanical challenges.

977

978

979**Acknowledgment**

980The authors are thankful to the Ministry of Petroleum & Natural Gas
981within the Government of India, Oil and Natural Gas Corporation
982Limited (ONGC), Directorate General of Hydrocarbons (DGH), Oil India
983Ltd, GAIL (India) Ltd, Indian Oil Corporation Ltd and all other NGHP
984partner organizations for providing the opportunity to contribute to the
985NGHP-02 Expedition and this special issue of the Journal of Marine and
986Petroleum Geology. The technical and science support from Japan
987Agency for Marine-Earth Science and Technology (JAMSTEC), United
988States Geological Survey (USGS), U.S. Department of Energy (US-DOE),
989Japan's National Institute of Advanced Industrial Science and
990Technology (AIST), Geotek Coring, and Schlumberger is gratefully
991acknowledged. This work was supported by the Assistant Secretary for
992Fossil Energy, Office of Natural Gas and Petroleum Technology,
993through the National Energy Technology Laboratory, under the U.S.
994Department of Energy, Contract No. DE-AC02-05CH11231.

995

996**References**

997Boswell, R., Yoneda, J., Waite, W., this issue-a: India National Gas

998 Hydrate Program Expedition 02 summary of scientific results:

999 Evaluation of natural gas hydrate-bearing pressure cores.

1000Boswell, R., Myshakin, E., Moridis, G., Konno, Y., Collett, T., Reagan, M.,

1001 Ajayi, T., Seol, Y., this issue-b: India National Gas Hydrate Program

1002 Expedition 02 summary of scientific results: Numerical simulation of

1003 reservoir response to depressurization.

1004Collett, T., et al., this issue, India National Gas Hydrate Program

1005 Expedition 02 – scientific results.

1006Kowalsky, M. B., and G.J. Moridis, 2007. Comparison of kinetic and

1007 equilibrium reactions in simulating the behavior of gas hydrates,

1008 *Energy Conversion and Management*, **48**, 1850,

1009 doi:10.1016/j.enconman.2007.01.017.

1010Kumar, P., et al., this issue, India National Gas Hydrate Program

1011 Expedition 02 – operational and technical summary.

1012Li, G., G.J. Moridis, K. Zhang and X.-S. Li, Evaluation of Gas Production

1013 Potential from Marine Gas Hydrate Deposits in Shenhu Area of the

1014 South China Sea, *Energy & Fuels*, **24**, 6018-6033, 2010 (doi:
 1015 10.1021/ef100930m).

1016Liu, N., Pan, L., Cheng, J., 2017. Numerical Modeling of CO₂ and Brine
 1017 Leakage through Open Fracture in a Fault Zone: Open Channel Flow
 1018 or Darcy Flow, *Geofluids*, 2017,
 1019 <https://doi.org/10.1155/2017/9035032>.

1020Marin-Moreno, H., T. A. Minshull, G. K. Westbrook, and B. Sinha 2015,
 1021 Estimates of future warming-induced methane emissions from
 1022 hydrate offshore west svalbard for a range of climate models,
 1023 *Geochemistry, Geophysics, Geosystems*, 16(5), 1307-1323.

1024Moridis, G.J. and E.D. Sloan, 2007. Gas Production Potential of Disperse
 1025 Low-Saturation Hydrate Accumulations in Oceanic Sediments, *J. of*
 1026 *Energy Conversion and Management*, **48**(6), 1834-1849, doi:
 1027 10.1016/j.enconman.2007.01.23.

1028Moridis, G.J., Kowalsky, M.B., Pruess, K., 2007. Depressurization-
 1029 induced gas production from Class 1 hydrate deposits. *SPE Res.*
 1030 *Eval. Eng.* **10** (5): 458-481.

1031Moridis, G.J., and Reagan, M.T., 2007a. Strategies for Gas Production
 1032 From Oceanic Class 3 Hydrate Accumulations, *OTC-18865*, 2007
 1033 Offshore Technology Conference, Houston, Texas, 30 April – 3 May
 1034 2007.

1035 Moridis, G.J., and Reagan, M.T., 2007b. Gas Production From Oceanic
 1036 Class 2 Hydrate Accumulations, *OTC 18866*, 2007 Offshore
 1037 Technology Conference, Houston, Texas, U.S.A., 30 April–3 May
 1038 2007.

1039 Moridis, G.J., Kowalsky, M.B., and Pruess, K., 2008. TOUGH+HYDRATE
 1040 v1.0 User's Manual: A Code for the Simulation of System Behavior in
 1041 Hydrate-Bearing Geologic Media, Report LBNL-00149E, Lawrence
 1042 Berkeley National Laboratory, Berkeley, CA.

1043 Moridis, G.J., M.T. Reagan, S.-J. Kim, Y. Seol and K. Zhang, 2009a.
 1044 Evaluation of the Gas Production Potential of Marine Hydrate
 1045 Deposits in the Ulleung Basin of the Korean East Sea, *SPE Journal*,
 1046 **14**(4): 759-781, doi: 10.2118/110859-PA.

1047 Moridis, G.J., T.S. Collett, R. Boswell, M. Kurihara, M.T. Reagan, E.D.
 1048 Sloan and C. Koh. Toward production from gas hydrates:
 1049 assessment of resources and technology and the role of numerical
 1050 simulation, *SPE Reservoir Evaluation & Engineering*, **12**(5): 745-771,
 1051 2009b (doi: 10.2118/114163-PA).

1052 Moridis, G.J., and M.T. Reagan, 2011a. Estimating the Upper Limit of
 1053 Gas Production From Class 2 Hydrate Accumulations in the
 1054 Permafrost, 1: Concepts, System Description and the Production

1055 Base Case, *J. Petr. Sci. Eng.*, 76, 194-201, (doi:10.1016/
 1056 j.petro.2010.11.023).

1057 Moridis, G.J., and M.T. Reagan, 2011b. Estimating the Upper Limit of
 1058 Gas Production From Class 2 Hydrate Accumulations in the
 1059 Permafrost, 2: Alternative Well Designs and Sensitivity Analysis, *J.*
 1060 *Petr. Sci. Eng.*, 76, 124-137, 2011b (doi: 10.1016/j.petro.
 1061 2010.12.001).

1062 Moridis, G.J., Silpngarm, S., Reagan, M.T., Collett, T., Zhang, K.,
 1063 2011c. Gas production from a cold, stratigraphically bounded
 1064 hydrate deposit at the Mount Elbert site, North Slope, Alaska. *J.*
 1065 *Marine Petr. Geol.*, **28**, 517-534 (doi:
 1066 10.1016/j.marpetgeo.2010.01.005)

1067 Moridis, G.J., M.T. Reagan, K.L. Boyle, and K. Zhang, 2011d. Evaluation
 1068 of the Gas Production Potential of Challenging Hydrate Deposits,
 1069 *Transport in Porous Media*, **90**, 269-299 (doi: 10.1007/s11242-011-
 1070 9762-5).

1071 Moridis, G.J. and Pruess, K. 2014. User's manual of the TOUGH+ Core
 1072 code v1.5: A general-purpose simulator of non-isothermal flow and
 1073 transport through porous and fractured media, LBNL Report 6871E,
 1074 <https://pubarchive.lbl.gov/islandora/object/ir%3A1005566>.

1075 Moridis, G.J. 2014. User's manual for the HYDRATE v1.5 option of
 1076 TOUGH+ v1.5: A code for the simulation of system behavior in
 1077 hydrate-bearing geologic media, LBNL Report 6869E,
 1078 <https://pubarchive.lbl.gov/islandora/object/ir%3A1005569>.

1079 Moridis, G.J., A.F. Queiruga and M.T. Reagan, The T+H+M Code for the
 1080 Analysis of Coupled Flow, Thermal, Chemical and Geomechanical
 1081 Processes in Hydrate-Bearing Geologic Media, Paper 1195,
 1082 Proceedings of the 9th International Conference on Gas Hydrates,
 1083 Denver, Colorado, 25-30 June 2017.

1084 Pruess, K., Oldenburg, C.M., Moridis, G.J., 1999. TOUGH2 Users Guide,
 1085 Version 2.0, LBNL Report 43134,
 1086 http://tough.lbl.gov/assets/docs/TOUGH2_V2_Users_Guide.pdf.

1087 Pruess, K., 2003. The TOUGH Codes – A Family of Simulation Tools for
 1088 Multiphase Flow and Transport Processes in Permeable Media, LBNL
 1089 Report 53630, [https://pubarchive.lbl.gov/islandora/object/ir](https://pubarchive.lbl.gov/islandora/object/ir%3A121930)
 1090 [%3A121930](https://pubarchive.lbl.gov/islandora/object/ir%3A121930).

1091 Queiruga, A.F. and M.T. Reagan. (2018, February 2). tough_convert:
 1092 Version 1.0. Zenodo. <http://doi.org/10.5281/zenodo.1164418>

1093 Rutqvist J. and G.J. Moridis, 2009. Numerical studies on the
 1094 geomechanical stability of hydrate-bearing sediments, *Soc. Pet.*
 1095 *Eng. J.*, **14**(2), 267–282 (doi: 10.2118/126129-PA).

1096Rutqvist J., Moridis G.J. and T. Grover, 2009. Geomechanical response
1097 of permafrost-associated hydrate deposits to depressurization-
1098 induced gas production, *J. Pet. Sci. Eng.*, **67**, 1-12.

1099Shukla, K.M., et al., this issue, Gas hydrate reservoir identification,
1100 characterization and delineation in Krishna-Godavari Basin using
1101 surface and subsurface data from Expedition NGHP-02, offshore
1102 India.

1103Stranne, C., O'Regan, M., Jakobsson M., 2016, Overestimating climate
1104 warming-induced methane gas escape from the seafloor by
1105 neglecting multiphase flow dynamics, *Geophys. Res. Lett.*, 43,
1106 doi:10.1002/ 2016GL070049.

1107Thatcher, K.E., Westbrook, G.K., Sarkar, S., Minshull, T.A., 2013,
1108 Methane release from warming-induced hydrate dissociation in the
1109 West Svalbard continental margin: Timing, rates, and geological
1110 controls, *J. Geophys. Res. Solid Earth*, 118(1), 22-38.

1111Waite, W., Jang, J., Collett, T., Kumar, P., this issue, Downhole physical
1112 property-based description of gas hydrate petroleum system in
1113 NGHP-02 Area C: a channel, levee, fan complex in the Krishna-
1114 Godavari basin offshore eastern India.

1115Yoneda, J., Oshima, M., Kida, M., Kato, A., Konno, Y., Jin, Y., Jang, J.,
1116 Waite, W., Kumar, P., Tenma, N., this issue-a, Pressure-core based

1117 onshore laboratory analysis on mechanical properties of hydrate-
 1118 bearing sediments recovered during India's National Gas Hydrate
 1119 Program Expedition (NGHP) 02.

1120 Yoneda, J., Oshima, M., Kida, M., Kato, A., Konno, Y., Jin, Y., Kumar, P.,
 1121 Tenma, N., this issue-b, Permeability variation and anisotropy of gas
 1122 hydrate-bearing pressure-core sediments recovered from the
 1123 Krishna-Godavari basin, offshore India.

1124 Zhang, K., and Moridis, G.J., 2008. A Domain Decomposition Approach
 1125 for Large-Scale Simulations of Coupled Processes in Hydrate-
 1126 Bearing Geologic Media, paper presented at the 6th International
 1127 Conference on Gas Hydrates, Vancouver, British Columbia, Canada,
 1128 July 6-10, 2008.

1129

1130
 1131
 1132
 1133
 1134
 1135
 1136
 1137
 1138
 1139

Table 1. Reservoir Conditions and Porous Media Properties in the Site NGHP-02-9 Study	
Hydrate dissociation model	Equilibrium
Overburden thickness	214.9 m

Underburden thickness	331.5 m
Initial pressure at top of domain/seafloor (P_T)	25.45 MPa
Pressure distribution with depth	Hydrostatic
Initial temperature at top of domain/seafloor (T_T)	3.46 °C
Initial temperature at base of domain (T_B)	38.4 °C
Temperature distribution with depth	Geothermal gradient (as affected by $k_{\theta C}$)
Gas composition	100% CH ₄
Water salinity	3.5%
Hydrate saturation in hydrate-bearing sands (HBS) S_H	0.75
Porosity (all formations) ϕ	0.45
Intrinsic permeability of the HBS layers k_r	10^{-11} m ² (= 10.0 D)
Initial effective permeability of the HBS layers $k_{r,eff}$	10^{-15} m ² (= 1 mD)
Intrinsic permeability of the other sand layers k_r	10^{-11} m ² (= 10.0 D)
Intrinsic permeability of the mud layers k_r	10^{-17} m ² (= 0.01 mD)
Intrinsic permeability of overburden/underburden k_r	10^{-17} m ² (= 0.01 mD)
k_r/k_v	1 (all media)
Pore compressibility of sand layers	1.3×10^{-8} Pa ⁻¹
Pore compressibility of mud layers	8.3×10^{-8} Pa ⁻¹
Grain density ρ_R	2750 kg/m ³ (overburden) 2700 kg/m ³ (all other formations)
Media specific heat (C_R)	1000 J/kg/K (all formations)
Wet thermal conductivity ($k_{\theta RW}$)	1.76 W/m/K (all formations)
Dry thermal conductivity ($k_{\theta RD}$)	0.3 W/m/K (all formations)
Composite (water, hydrate, ice, rock) thermal conductivity model (Moridis et al., 2014)	$k_{\theta C} = k_{\theta RD} + (S_A^{1/2} + S_H^{1/2}) (k_{\theta RW} - k_{\theta RD}) + \phi S_I$
Capillary pressure model (van Genuchten, 1980)	$P_{cap} = -P_0 \left[(S^*)^{-1/\lambda} - 1 \right]^{-\lambda}$ $S^* = \frac{(S_A - S_{irA})}{(S_{mxA} - S_{irA})}$
λ	0.45 (sand); 0.25 (clay/mud)
P_0	10^4 Pa (sand); 10^6 Pa (clay/mud)
Relative permeability model (Moridis et al., 2014)	$k_{rA} = (S_A^*)^n$ $k_{rG} = (S_G^*)^m$ $S_A^* = (S_A - S_{irA}) / (1 - S_{irA})$ $S_G^* = (S_G - S_{irG}) / (1 - S_{irA})$
$n; m$	3.855; 2.5 (sand) 3.5; 2.5 (clay/mud)
Irreducible gas saturation S_{irG}	0.01 (sand); 0.03 (clay/mud)
Irreducible water saturation S_{irA}	0.10 (sand); 0.90 (clay/mud)
Constant bottomhole pressure BHP (P_w)	3.0 MPa

1140

1141

1142

1143

1144

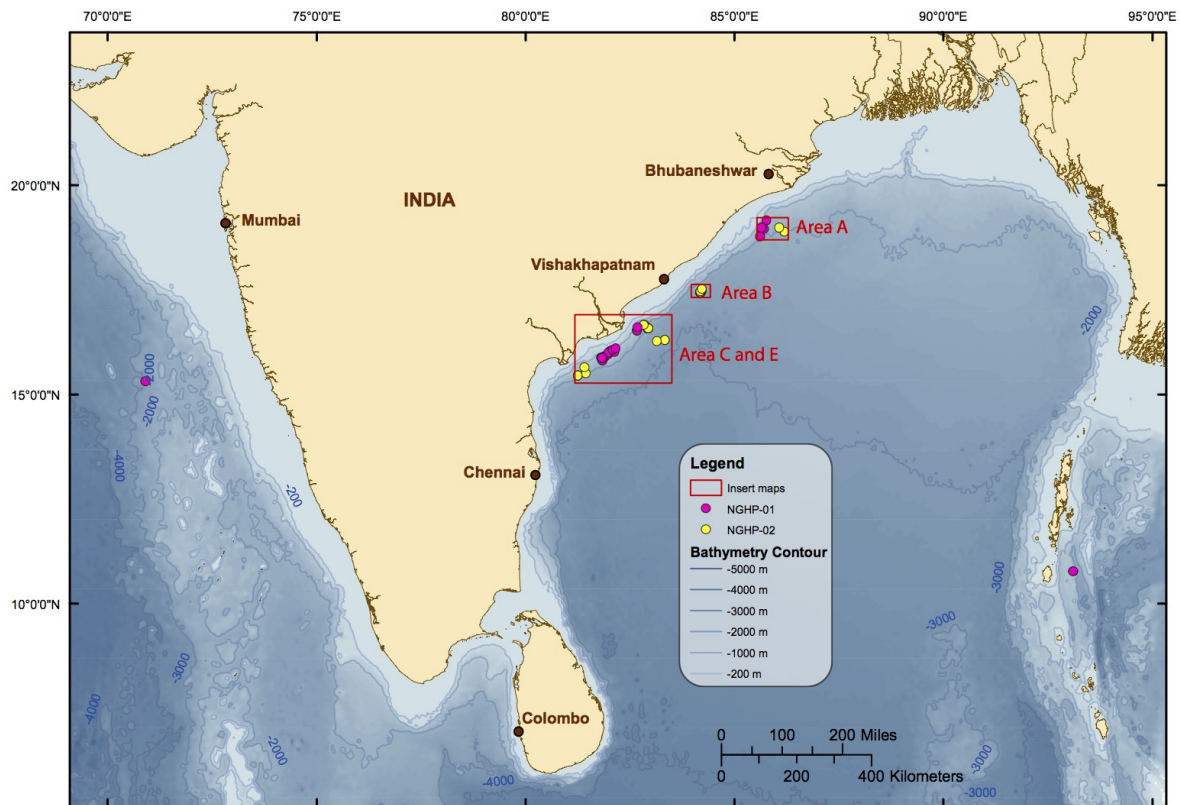
Table 2. Material Geomechanical Properties in the Site NGHP-02-9 Study						
Layers	Young's modulus	Skeletal density	Poisson ratio	Shear modulus	Cohesion	Friction Angle
Mud zones: Overburden	E=109 MPa	2750 kg/m ³	0.30	6 MPa	0.5 MPa	30°
Sand zones	E=50 MPa (at S _H =0) E=199 MPa (at S _H =1)	2700 kg/m ³	0.40	16 MPa	0.5 MPa	30°
Underburden	E=109 MPa	2700 kg/m ³	0.30	8 MPa	0.5 MPa	30°
Interlayer mud zones	E=109 MPa	2700 kg/m ³	0.30	7 MPa	0.5 MPa	30°

1145

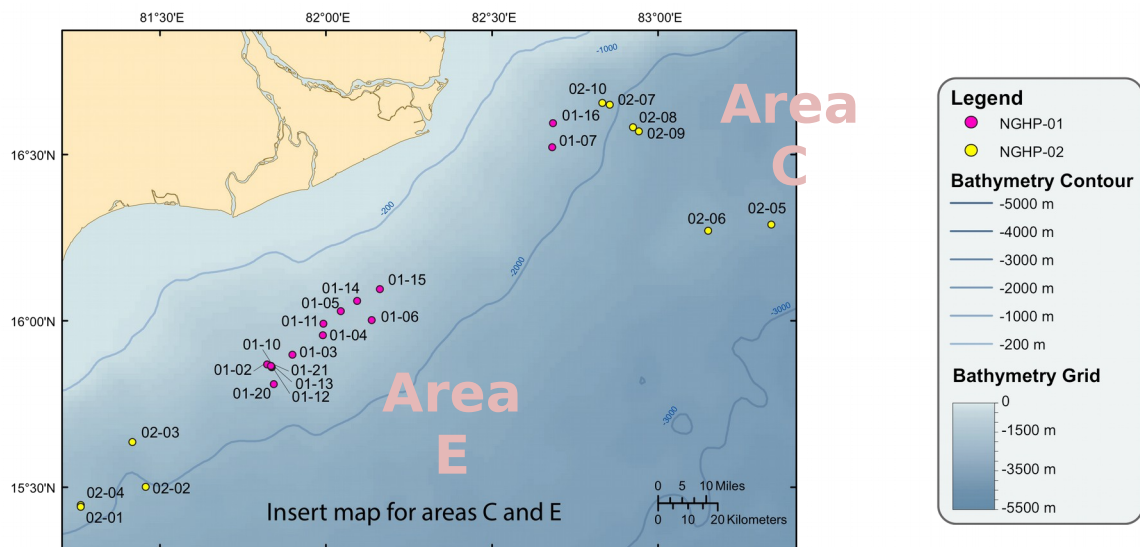
1146

1147

1148



1149

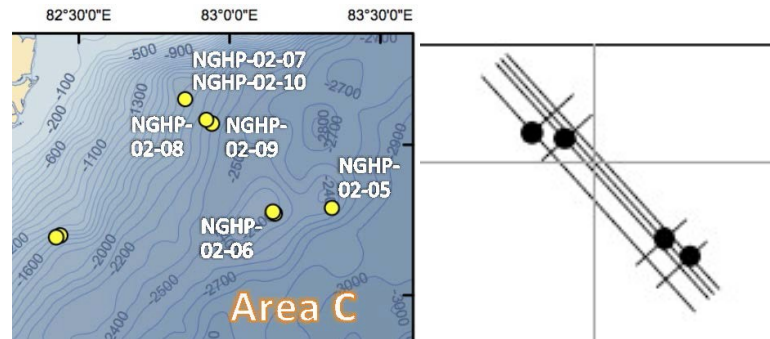


1150
1151

Figure 1. Physiographic map of the Krishna-Godavari (KG) Basin, areas of investigation during the NGHP-02 scientific cruise, and location of Site NGHP-02-09 (NGHP-02 Expedition Scientific Party).

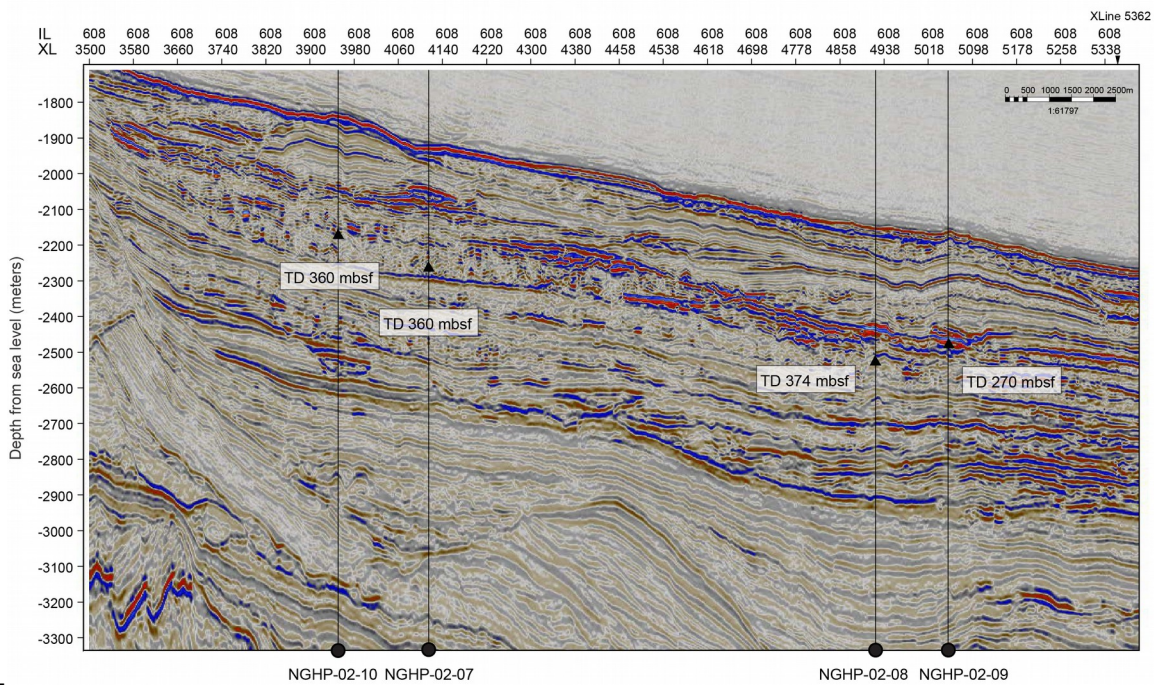
1155

1156
1157
1158



1159
1160

Seismic profile showing slope sediment with channel-levee system in Area C, NGHP Expedition 02.



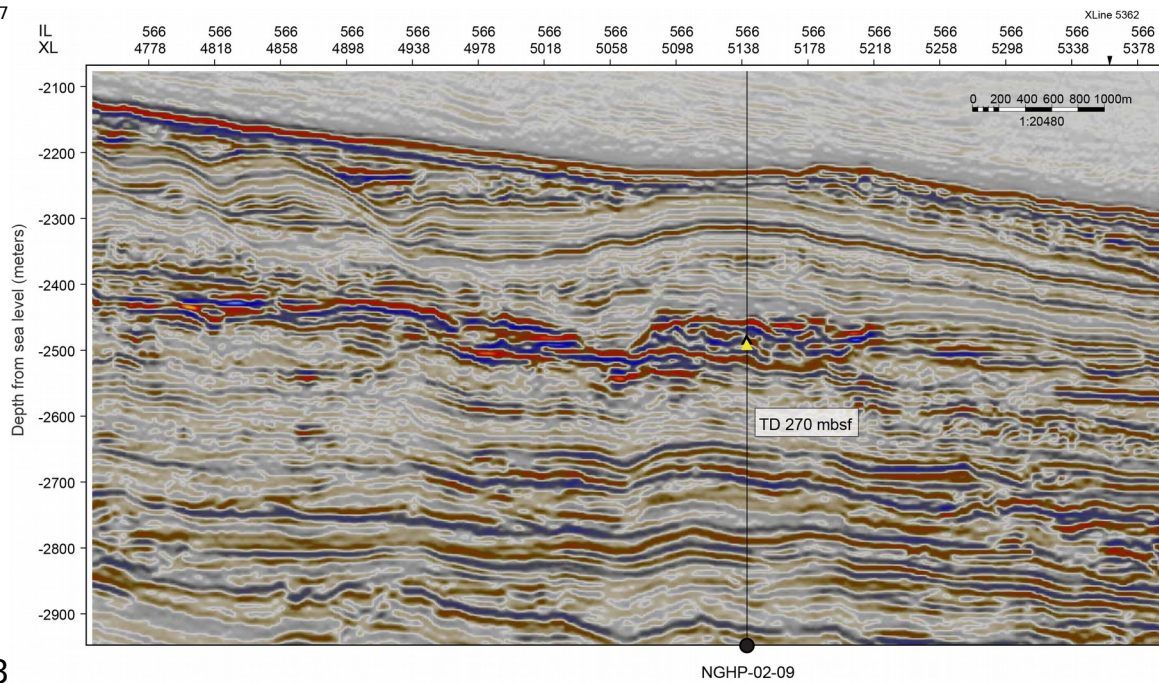
1161

Figure 2 - The gas hydrate petroleum system in the KG Basin, seismic profile showing the slope-rise channel-levee system in Area C. Sites NGHP-02-08 and -09 penetrate levee deposits on either side of the channel near the toe of the continental slope (Collett et al., this issue).

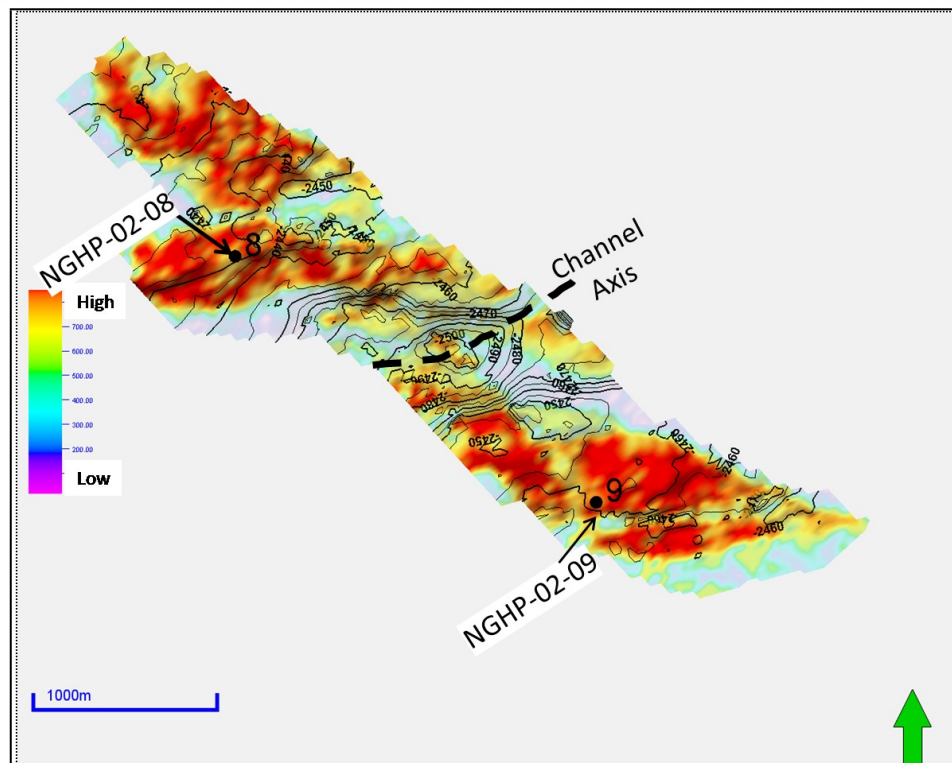
1165

1166

1167



1168



1169

Figure 3. (a) Seismic profile through Site NGHP-02-09 (Collett et al., this issue), showing an image of the slope-rise channel-levee system in Area C. (b) Seismic amplitude distribution at 40 ms (TWT) close to the top of the gas hydrate reservoir at Sites NGHP-02-08 and NGHP-02-09 in Area C (Shukla et al., this issue).

1174

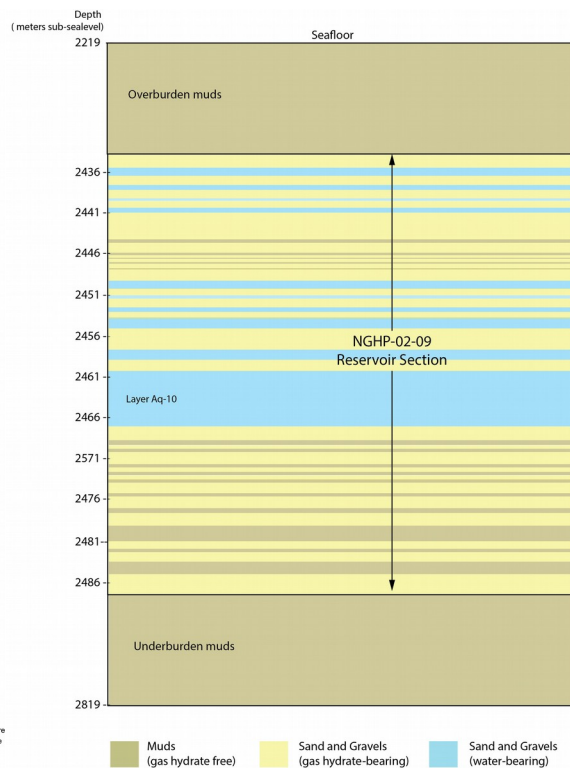
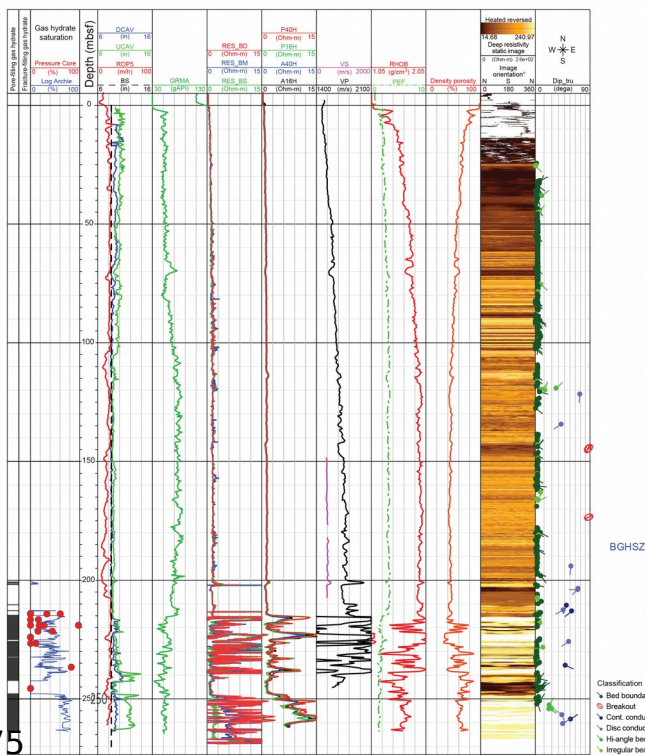
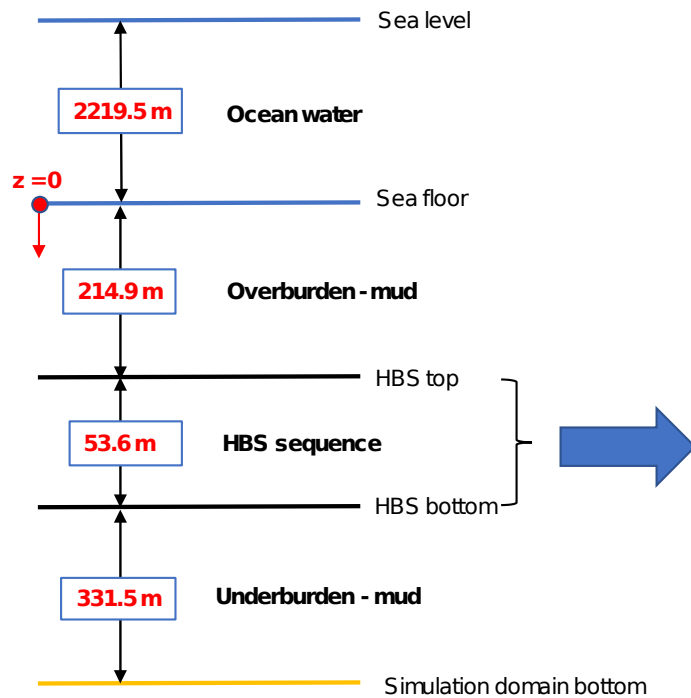


Figure 4. (a) Composite LWD log data display for Hole NGHP-02-09-A. BS =bit size, ROP5
 =rate of penetration averaged over the last 5 ft, UCAV = ultrasonic caliper, DCAV = density
 caliper, GRMA = natural gamma radiation, RES_BD = deep button resistivity, RES_BS = shallow
 button resistivity, RES_BM = medium button resistivity, P40H/P16H = phase-shift resistivity,
 A40H/A16H = attenuation resistivity, VS = shear velocity, VP = compressional velocity, PEF =
 photoelectric factor, RHOB = bulk density (Collett et al., this issue). (b) Interpreted layered
 reservoir geology at Site NGHP-02-09 (Area C) in the KG Basin (Collett et al., this issue).

1187



Layer #	Layer Name	Δz (m)	Z_0 (m)
1	Hyd01	1.8	-216.7
2	Aqu01	0.8	-217.5
3	Hyd02	1.3	-218.8
4	Aqu02	0.5	-219.3
5	Hyd03	1.1	-220.4
6	Aqu03	0.2	-220.6
7	Hyd04	0.8	-221.4
8	Aqu04	0.6	-222.0
9	Hyd05	3.3	-225.3
10	Mud01	0.5	-225.8
11	Hyd06	1.3	-227.1
12	Mud02	0.4	-227.5
13	Hyd07	0.3	-227.8
14	Mud03	0.2	-228.0
15	Hyd08	0.4	-228.4
16	Mud04	0.2	-228.6
17	Hyd09	0.5	-229.1
18	Mud05	0.2	-229.3
19	Hyd10	1.3	-230.6
20	Aqu05	1.1	-231.7
21	Hyd11	0.8	-232.5
22	Aqu06	0.3	-232.8
23	Hyd12	1.1	-233.9
24	Aqu07	0.4	-234.3
25	Hyd13	0.7	-235.0
26	Aqu08	1.3	-236.3
27	Hyd14	2.6	-238.9
28	Aqu09	1.2	-240.1
28	Hyd15	1.3	-241.4
30	Aqu10	6.9	-248.3
31	Hyd16	1.7	-250.0
32	Mud06	0.6	-250.6
33	Hyd17	2.3	-252.9
34	Mud07	0.4	-253.3
35	Hyd18	0.5	-253.8
36	Mud08	0.4	-254.2
37	Hyd19	0.5	-254.7
38	Mud09	0.4	-255.1
39	Hyd20	1.2	-256.3
40	Mud10	0.4	-256.7
41	Hyd21	1.4	-258.1
42	Mud11	0.6	-258.7
43	Hyd22	1.5	-260.2
44	Mud12	2.0	-262.2
45	Hyd23	0.8	-263.0
46	Mud13	0.4	-263.4
47	Hyd24	1.2	-264.6
48	Mud14	1.4	-266.0
49	Hyd25	2.5	-268.5

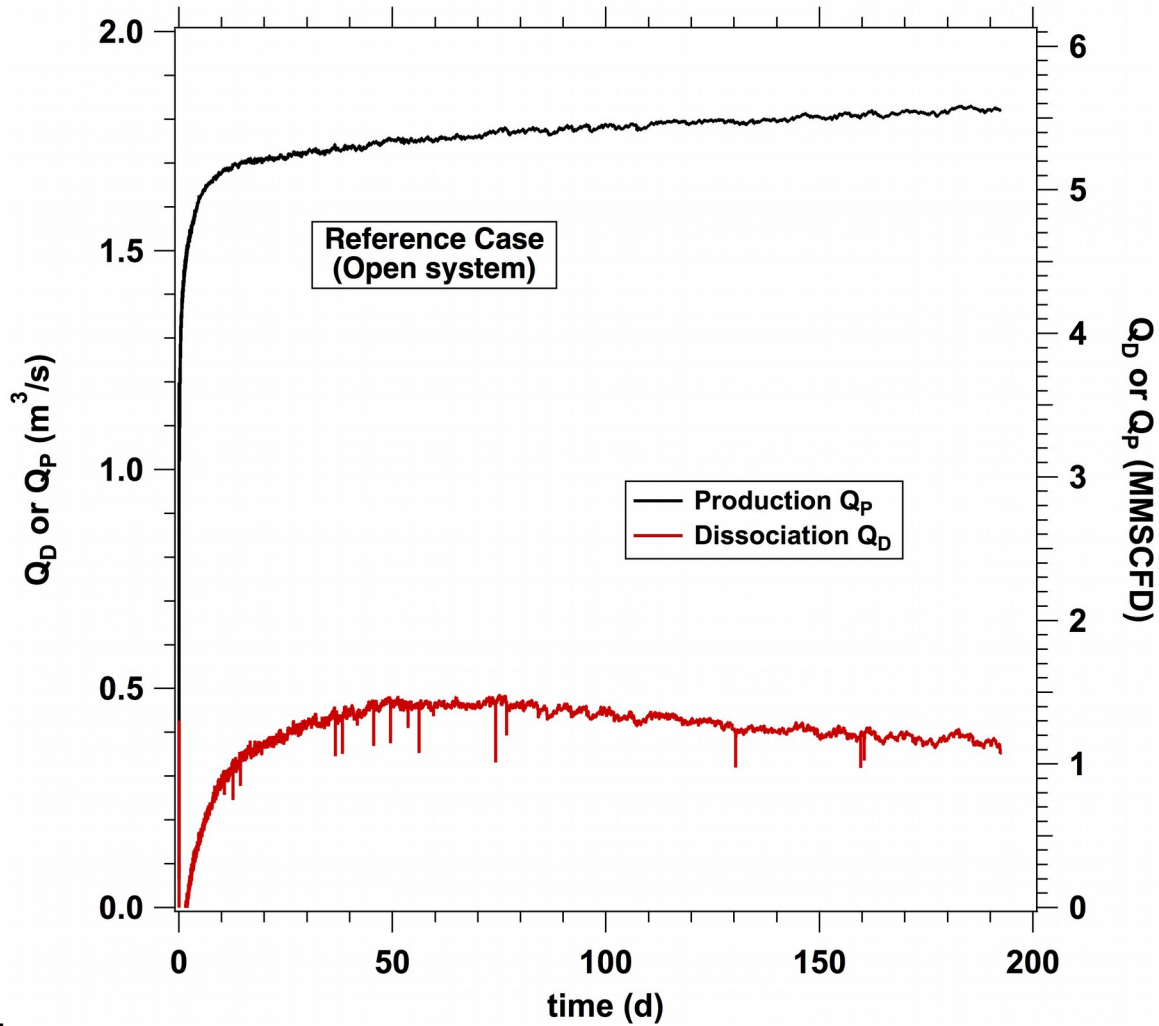
1188

1189
1190**Figure 5.** A simple representation (not to scale) of the geology, stratification, texture and
1191dimensions in the subsurface at at Site NGHP-02-09 of the KG Basin, as used in the description
1192of the simulation domain. The “Hyd”, “Aqu” and “Mud” prefixes in the layer description
1193indicate hydrate-bearing sand, hydrate-free sand and mud, respectively. The origin of the z-
1194axis used in the simulation grid coordinates is also clearly shown.

1195
1196

1197
1198

1199
1200

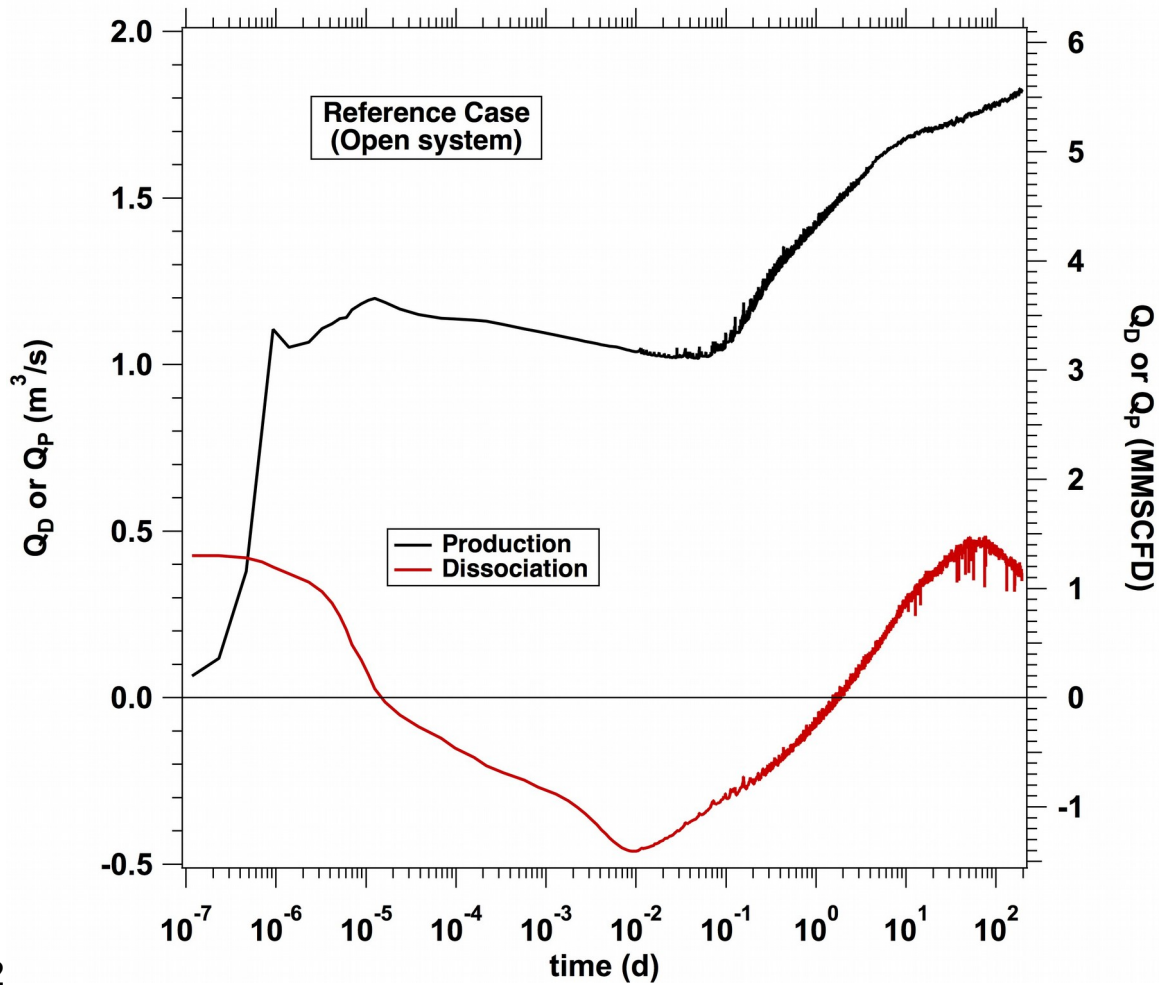


1201
1202

1203 **Figure 6.** Reference Case R (open system, infinite-acting boundaries): expected evolution of
1204 the rate of gas release from dissociation (Q_D) and the rate of gas production (Q_P) over time
1205 during the planned long-term field test at Site NGHP-02-09 of the KG Basin. Note that Q_D is
1206 consistently (and substantially) lower than Q_P .

1207
1208

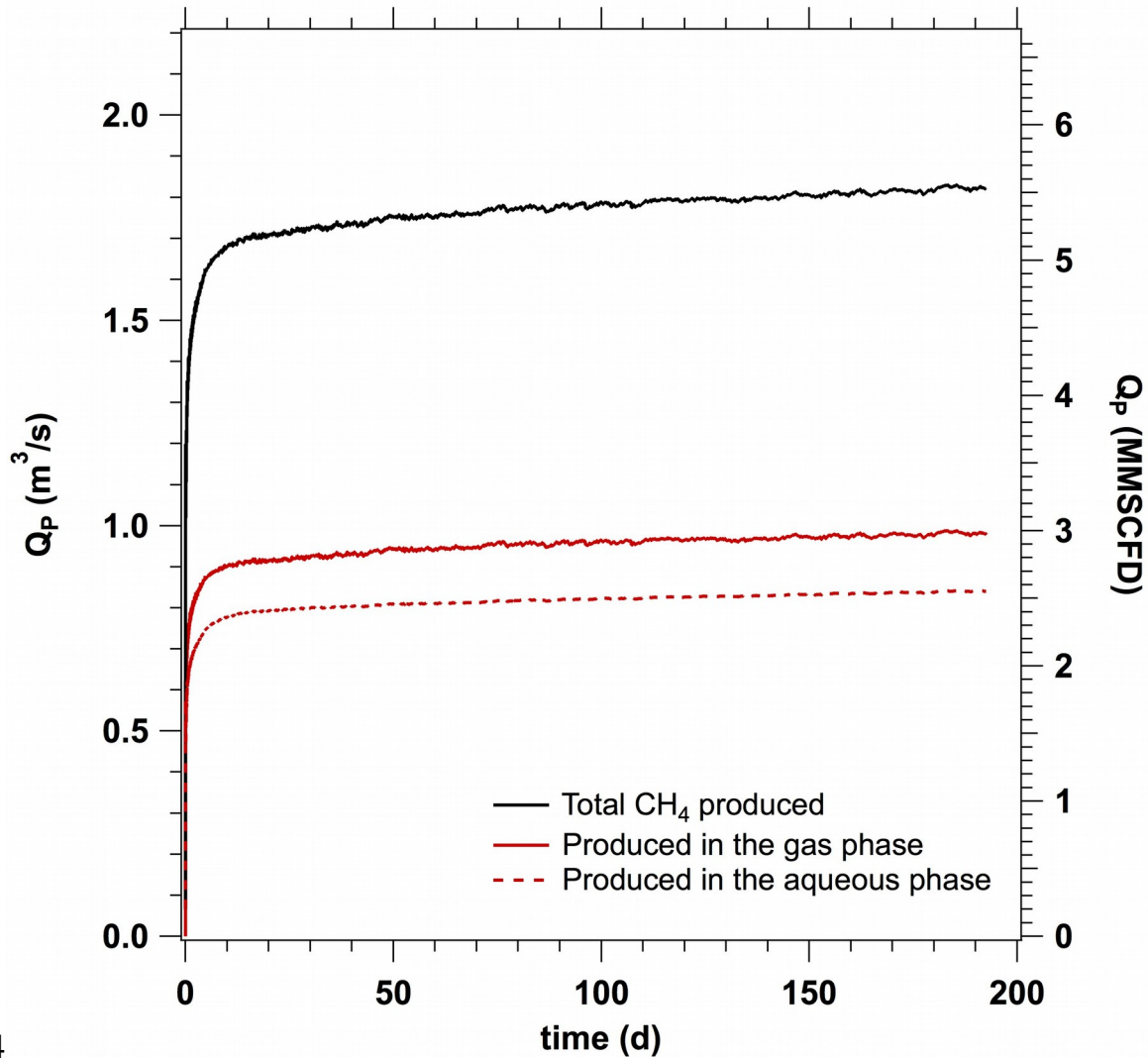
1209
1210
1211



1212
1213
1214
1215
1216
1217
1218
1219
1220

Figure 7. Semi-log plot of the expected evolution of Q_D and Q_P of the reference Case R (shown in Fig. 6) that captures the early time behavior of the system. The negative Q_P immediately after the initiation of production is attributed to secondary hydrate formation involving gas released from exsolution in the water.

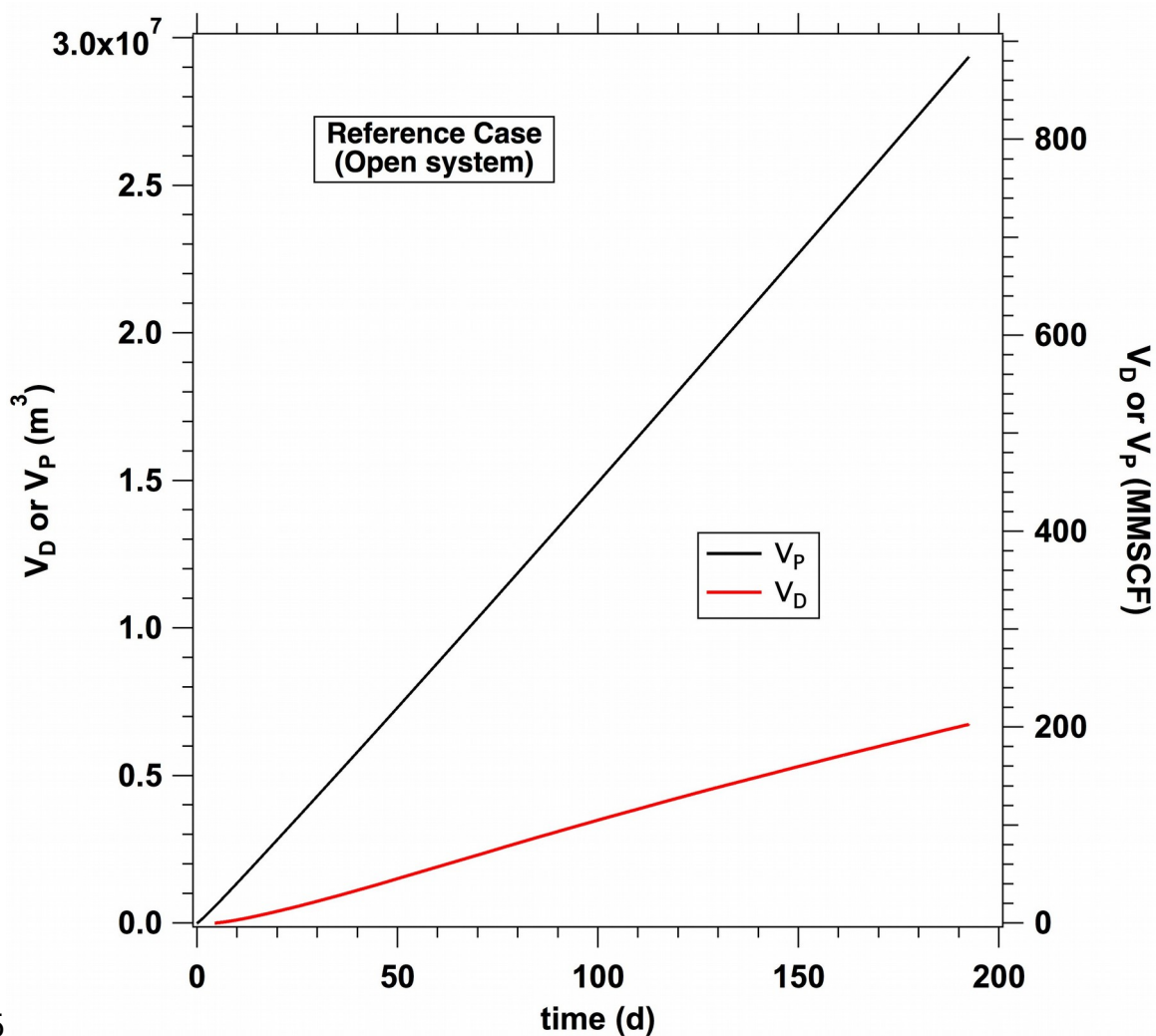
1221
1222
1223



1224
1225
1226
1227
1228
1229
1230
1231

Figure 8. Provenance of gas in the produced fluids for Case R. Exsolution of dissolved gas from the produced water provides almost as much gas as as derived from hydrate dissociation to the total produced methane, Q_P , seen in Figure 6.

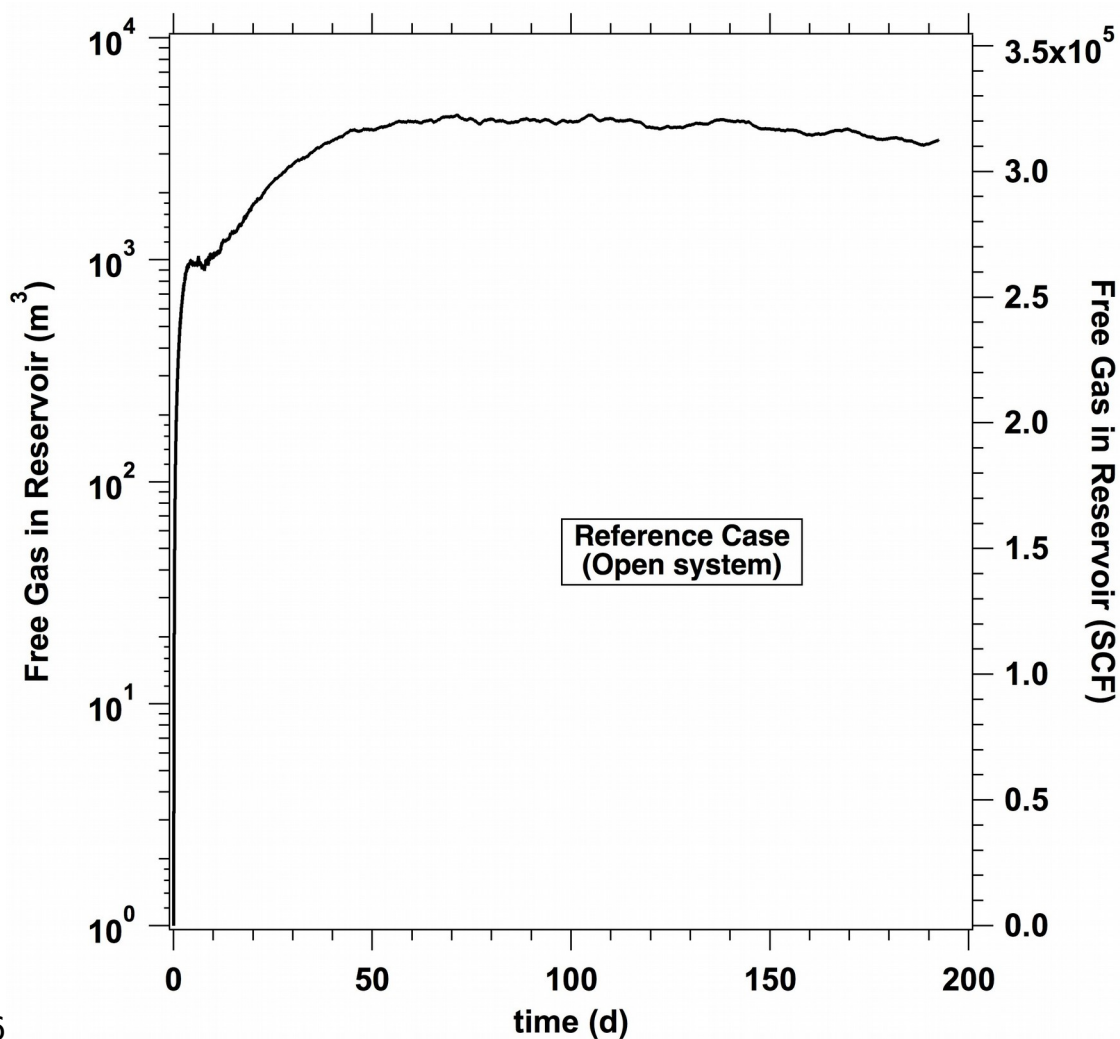
1232
1233
1234



1235
1236
1237
1238
1239
1240
1241
1242

Figure 9. Reference Case R (open system): Cumulative volumes of released and produced gas (V_D and V_P , respectively) over time during the planned long-term test at Site NGHP-02-09 of the KG Basin. Note that $V_D < V_P$ at all times.

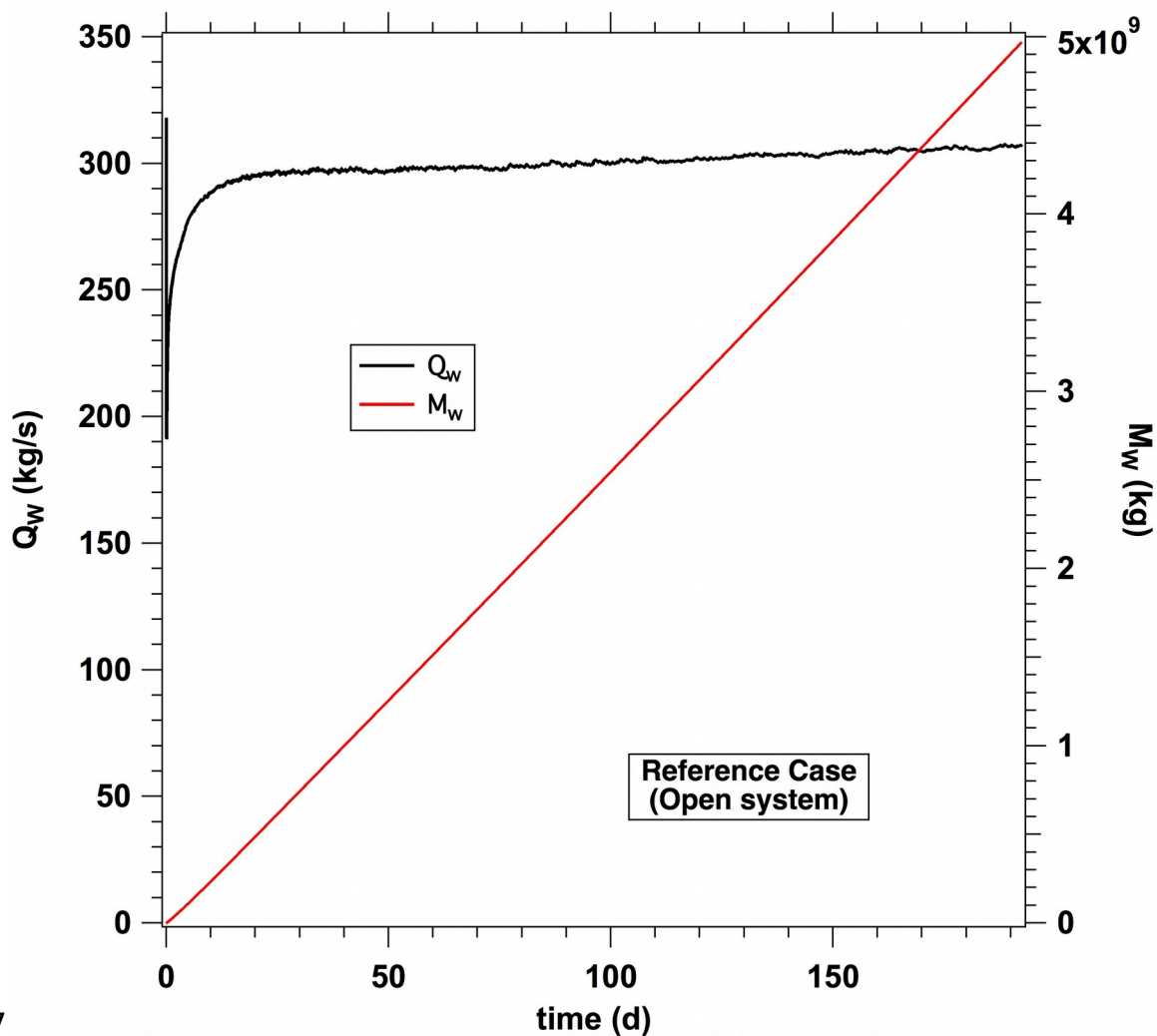
1243
1244
1245



1246
1247
1248
1249
1250
1251
1252
1253

Figure 10. Reference Case R (open system): evolution of the volume of the free gas phase in the reservoir (V_F) over time during the planned long-term test at Site NGHP-02-09 of the KG Basin. Note the modest V_F magnitude and its relative stability for $t > 50$ days.

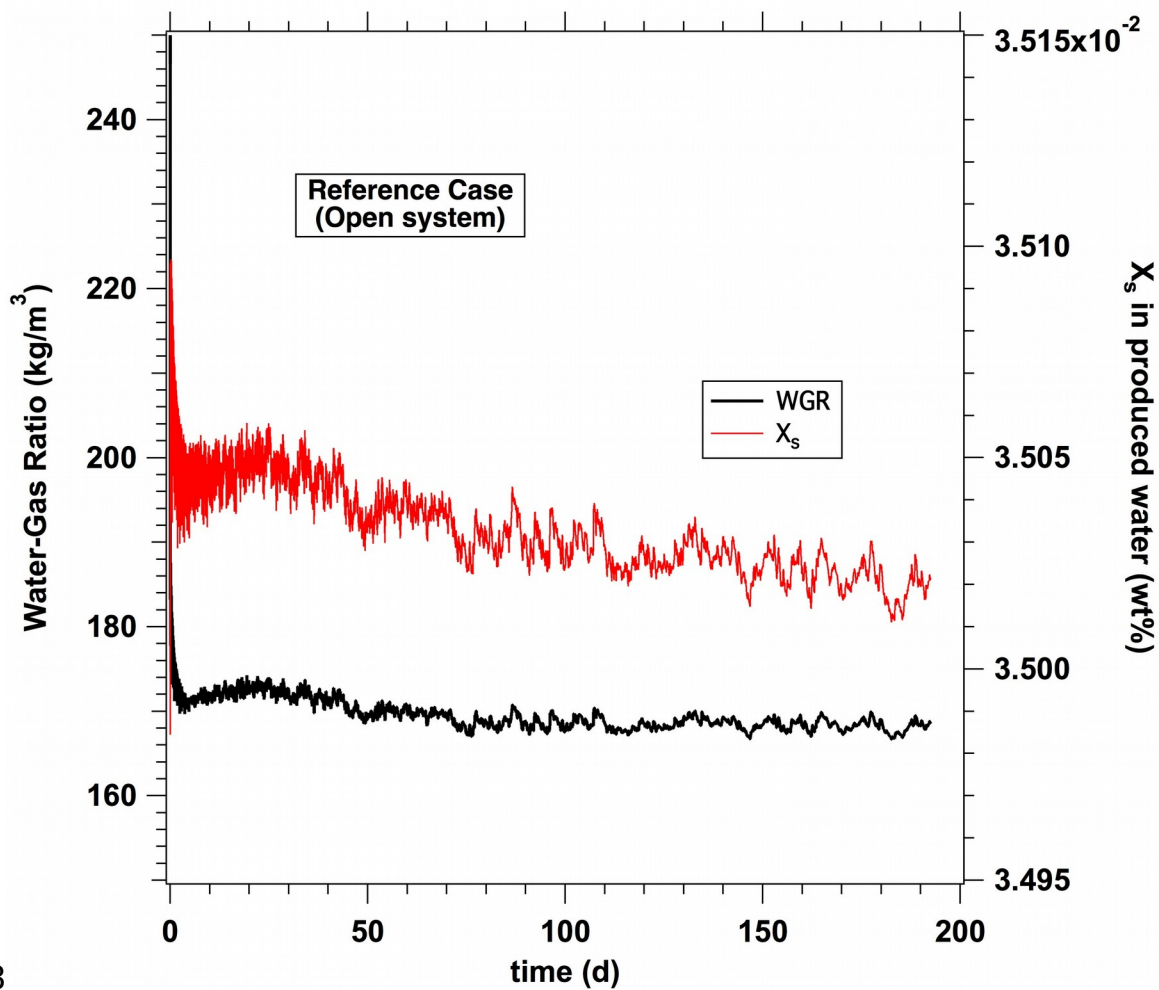
1254
1255
1256



1257
1258
1259
1260
1261
1262
1263
1264

Figure 11. Reference Case R (open system): evolution of (a) the rate of water production (Q_w) and (b) the cumulative mass of water (M_w) over time during the planned long-term test at Site NGHP-02-09 of the KG Basin. Note the non-declining Q_w for practically the entire test period.

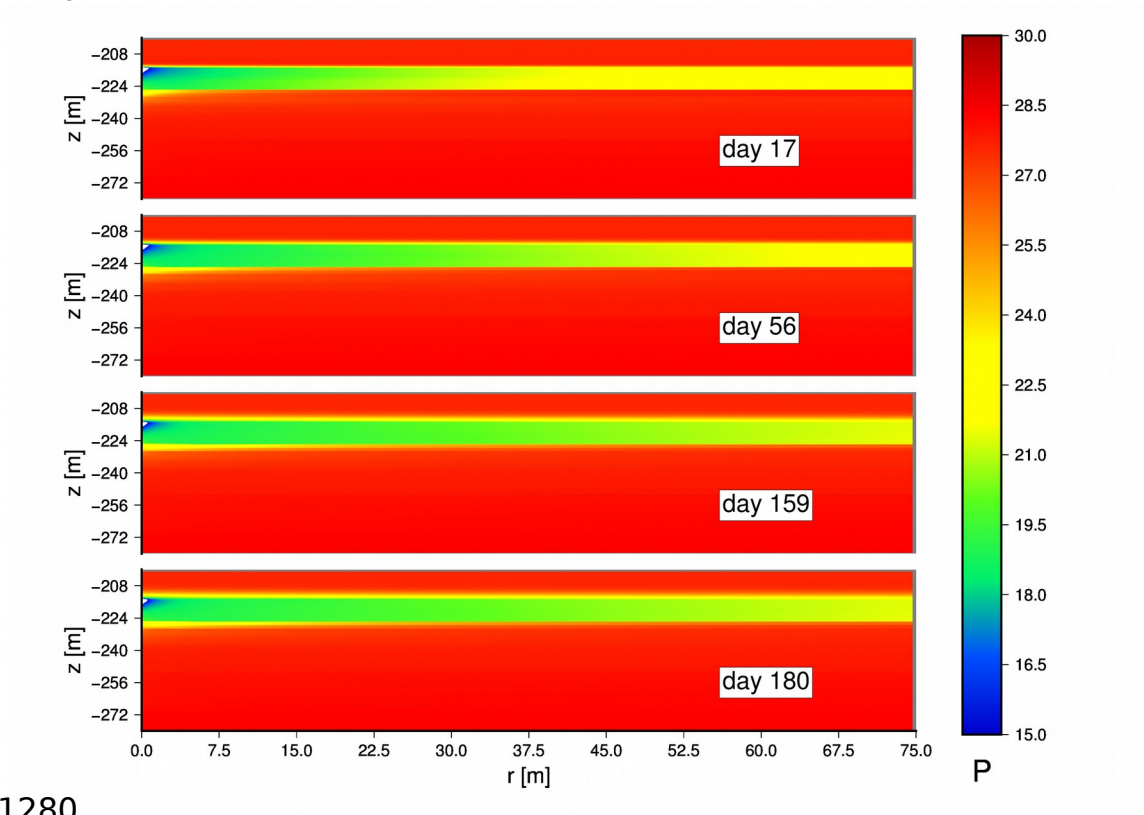
1265
1266
1267



1268
1269
1270
1271
1272
1273
1274
1275
1276

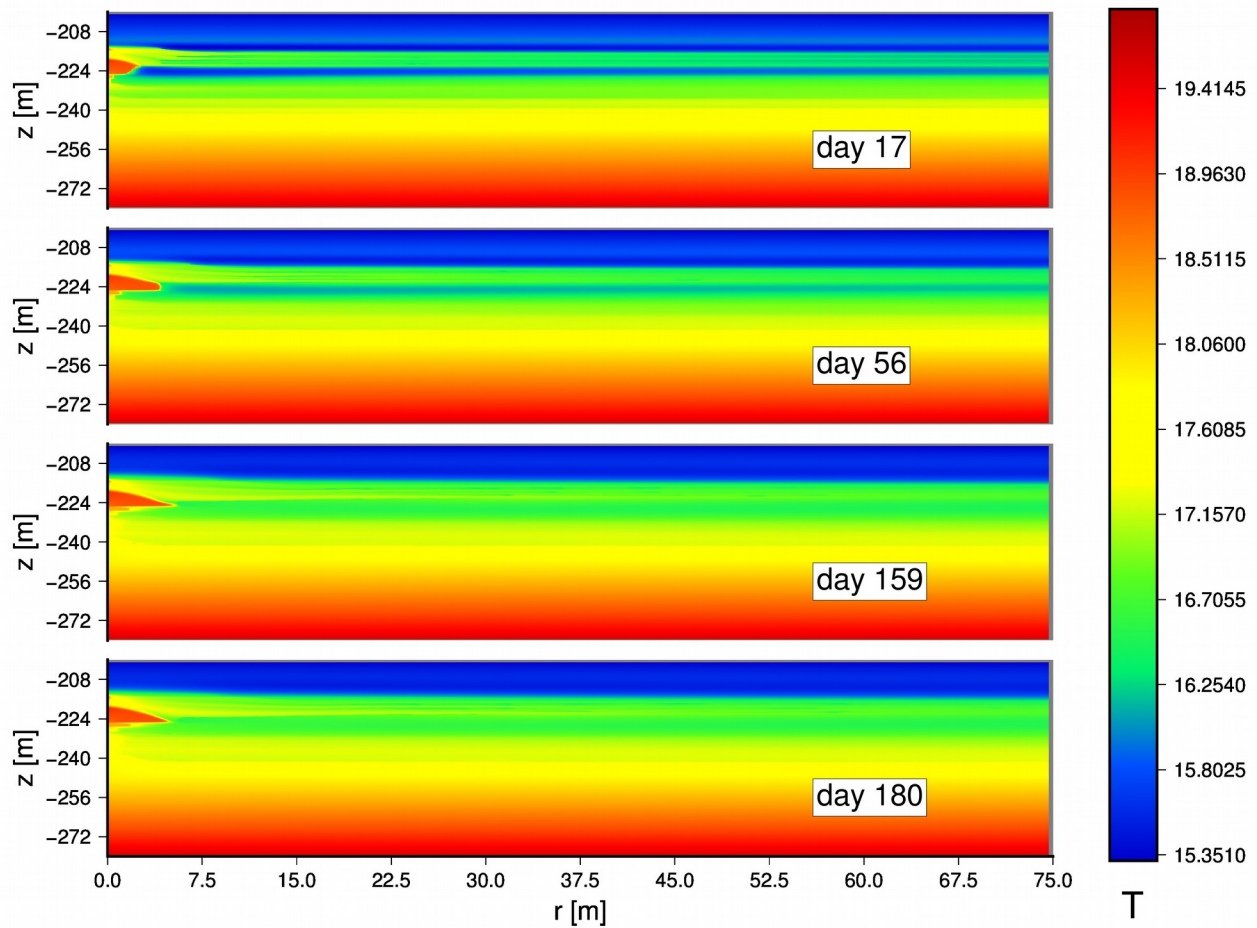
Figure 12. Reference Case R (open system): evolution of (a) the water-to-gas ratio (*WGR*) and (b) the salt mass fraction X_s in the produced water during the planned long-term test at Site NGHP-02-09 of the KG Basin. Note the high-value (and stability) of *WGR* during the test period, and the high level of X_s .

1277
1278
1279



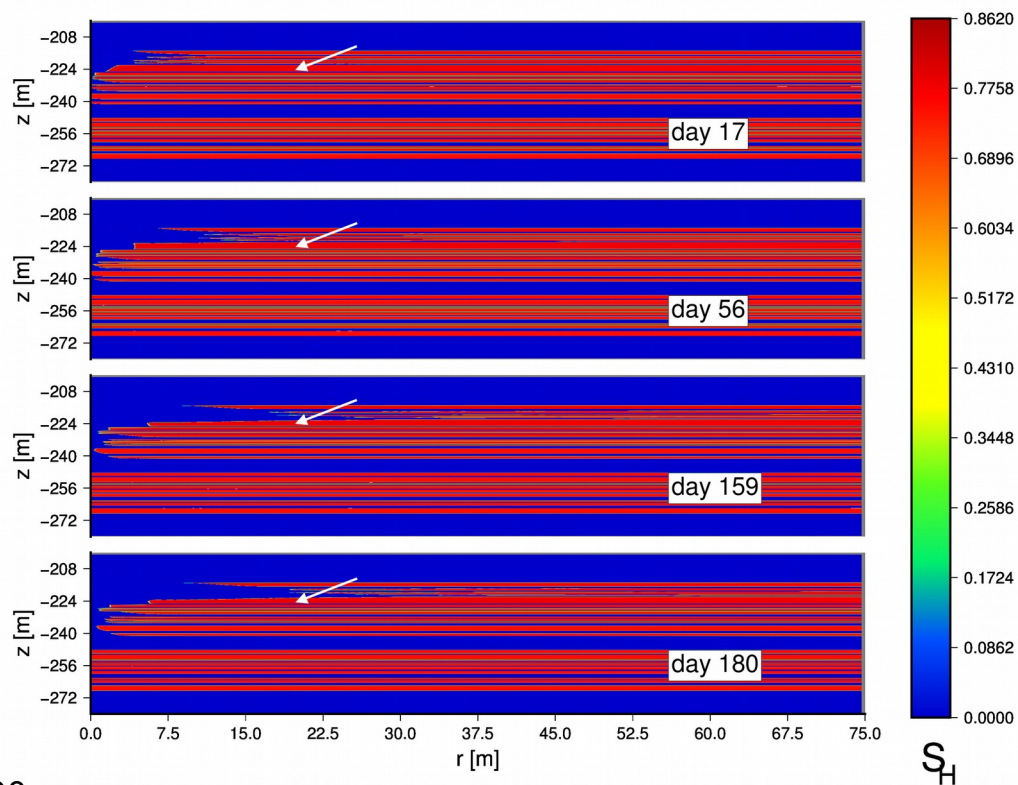
1280
1281
1282 **Figure 13.** Case R: Evolution of pressure (in MPa) distribution in the system during the long-
1283 term production test at Site NGHP-02-09 of the KG Basin ($P_w = 3$ MPa).
1284
1285
1286

1287
1288
1289



1290
1291
1292 **Figure 14.** Case R: Evolution of temperature (in $^{\circ}\text{C}$) distribution in the system during the long-
1293 term production test at Site NGHP-02-09 of the KG Basin ($P_w = 3$ MPa).
1294
1295
1296

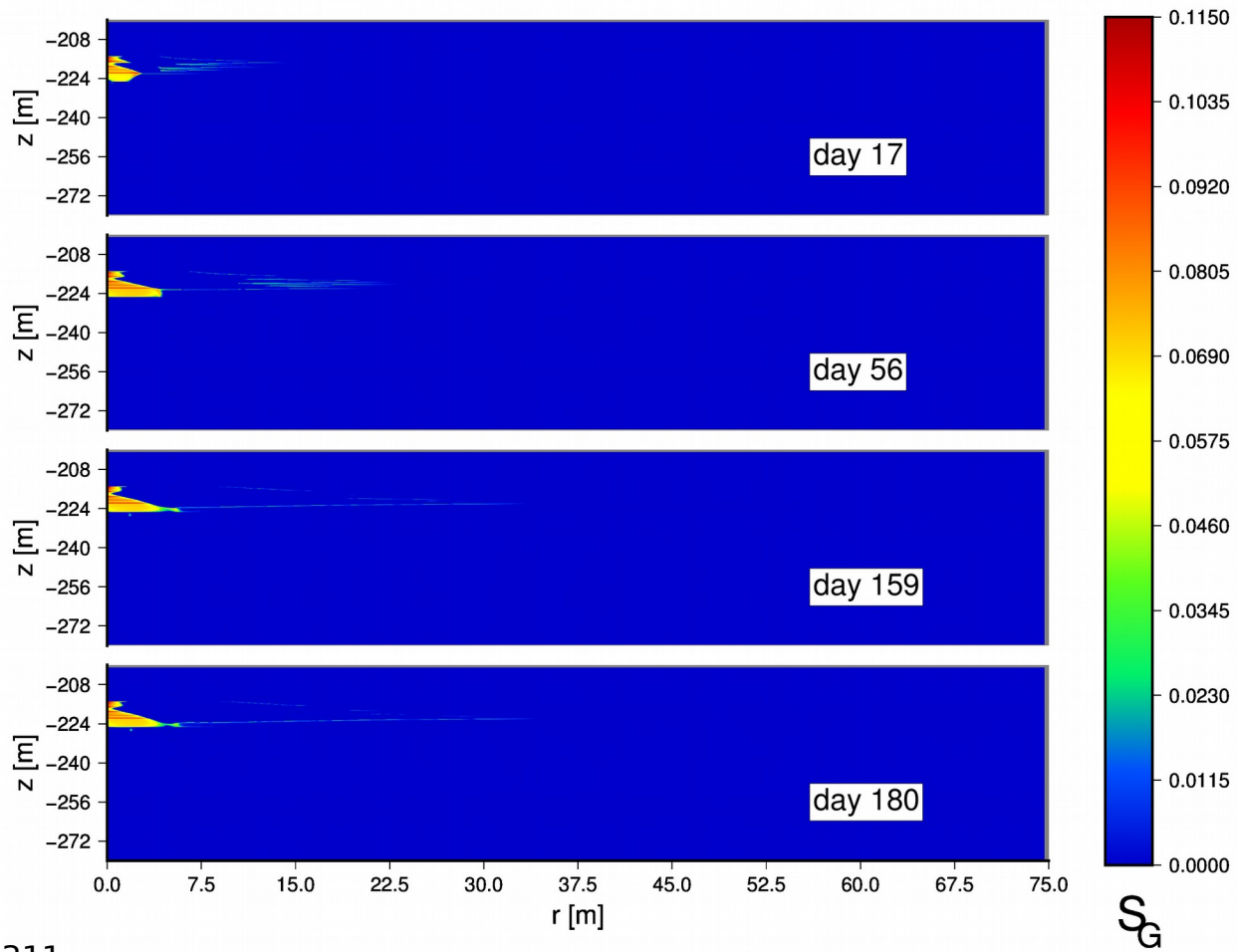
1297
1298
1299



1300
1301
1302
1303
1304
1305
1306
1307

Figure 15. Case R: Evolution of the hydrate saturation S_H distribution in the system during the long-term production test at Site NGHP-02-09 of the KG Basin ($P_w = 3$ MPa). Arrows indicate layers where $S_H > 0.75$.

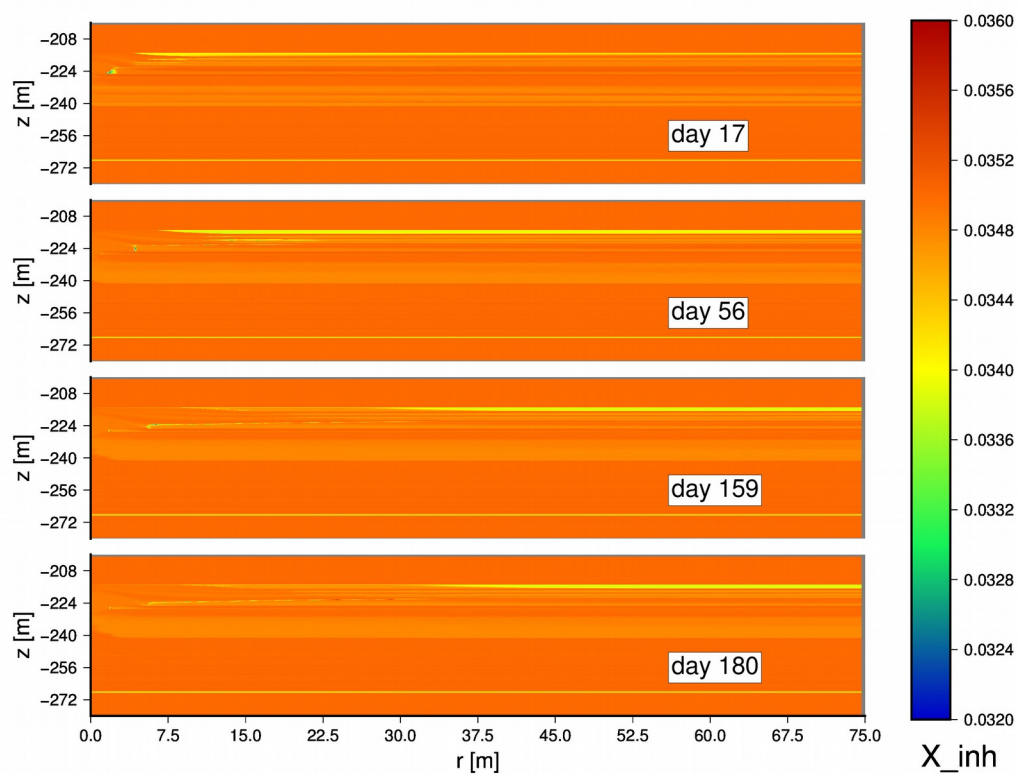
1308
1309
1310



1311
1312
1313
1314
1315
1316
1317

Figure 16. Case R: Evolution of the gas saturation S_G distribution in the system during the long-term production test at Site NGHP-02-09 of the KG Basin ($P_w = 3$ MPa).

1318
1319
1320

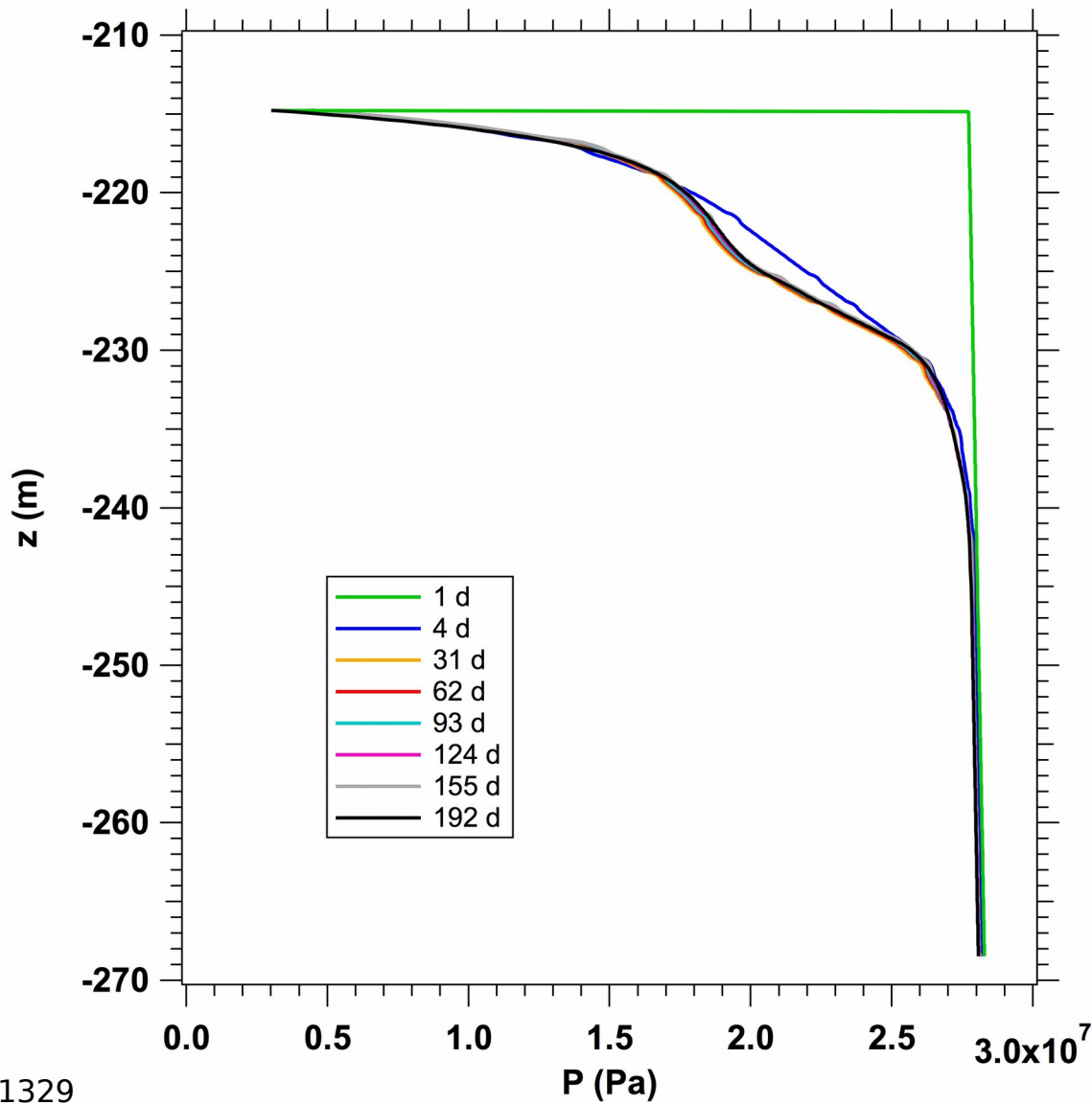


1321
1322

Figure 17. Case R: Evolution of the distribution of the salt mass fraction X_s in the aqueous phase of the system during the long-term production test at Site NGHP-02-09 of the KG Basin.

1325

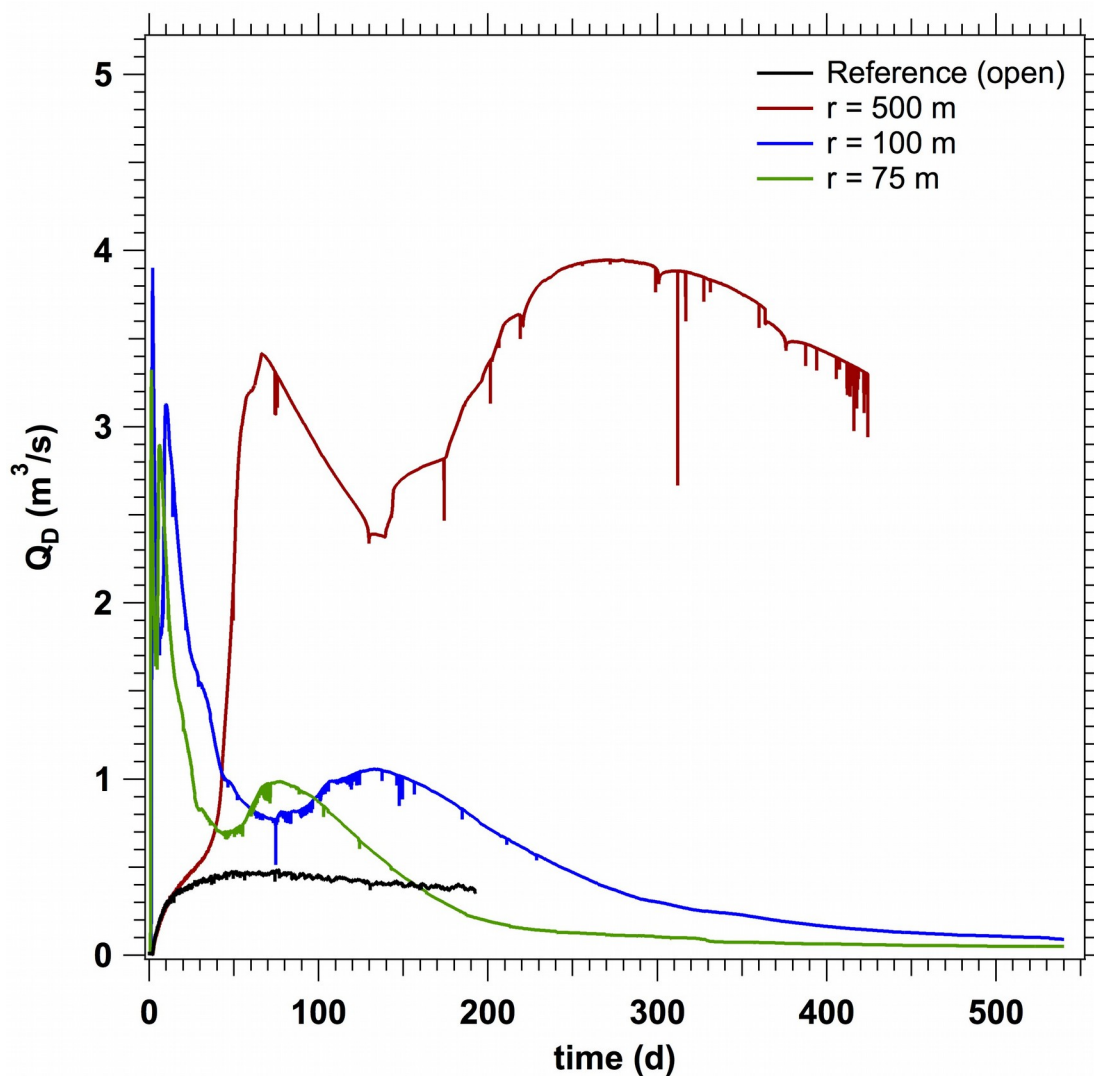
1326
1327
1328



1329
1330
1331
1332
1333
1334
1335
1336
1337
1338

Figure 18. Case R: Evolution of the pressure distribution with depth at the well during the long-term production test at Site NGHP-02-09 of the KG Basin ($P_w = 3$ MPa). Note the lack of pressure response below $z = -240$ m (from the ocean floor), where the thick, highly permeable aquifer horizon “Aqu09” begins.

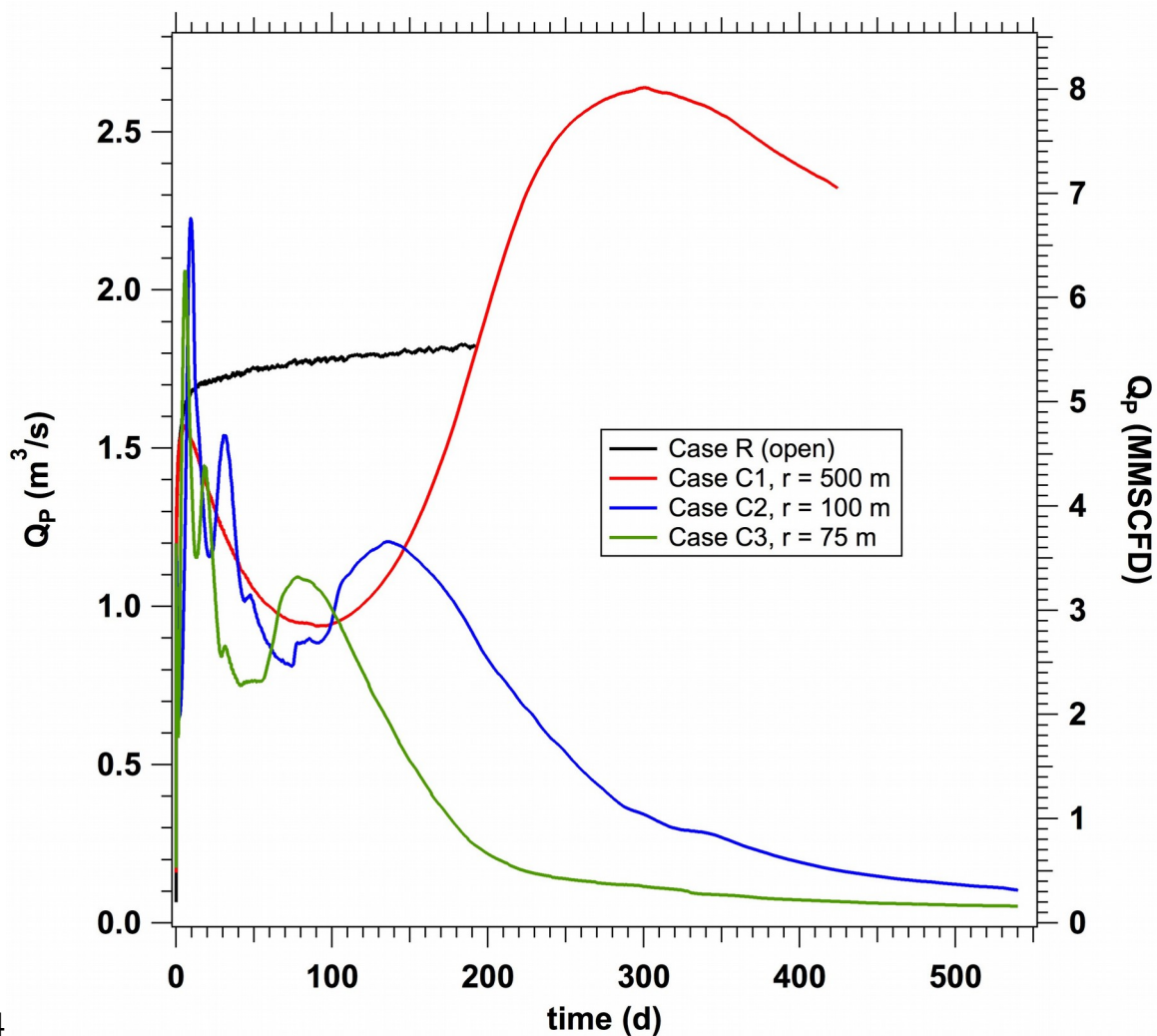
1339
1340



1341
1342
1343
1344
1345
1346
1347
1348
1349
1350

Figure 19. Cases C1, C2, C3 (closed systems): evolution of the rate of gas release from dissociation (Q_D) over time during multi-well operations at Site NGHP-02-09 of the KG Basin. The Q_D for the reference Case R (open system) is included for comparison.

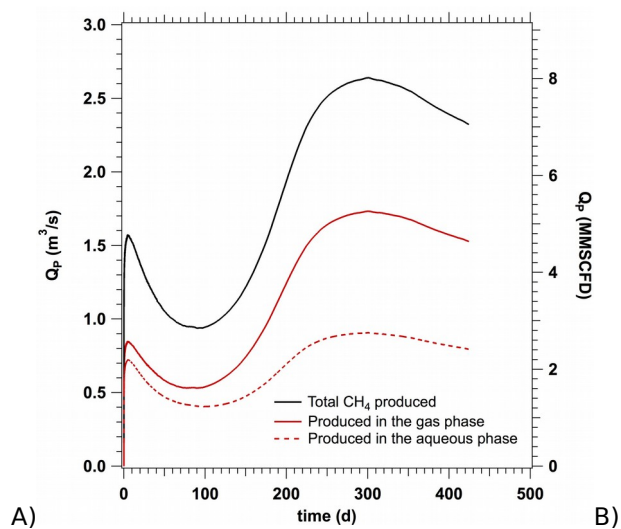
1351
1352
1353



1354
1355
1356
1357
1358
1359
1360
1361
1362

Figure 20. Cases C1, C2, C3 (closed systems): evolution of the rate of gas production (Q_p) over time during long-term multi-well operations at Site NGHP-02-09 of the KG Basin. The Q_p for the reference Case R (open system) is included for comparison.

1363



1364

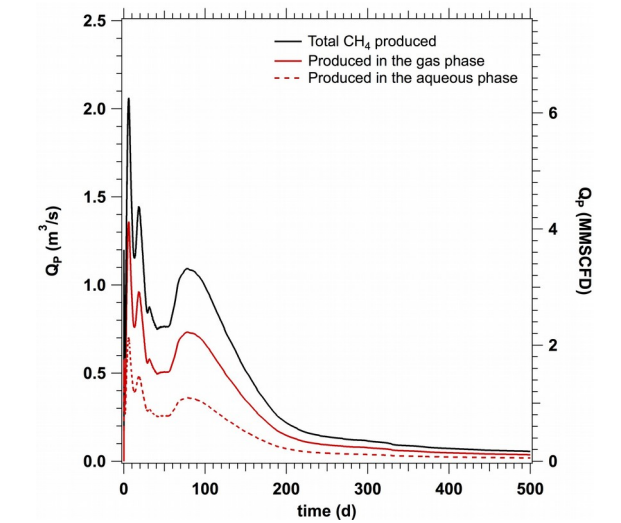
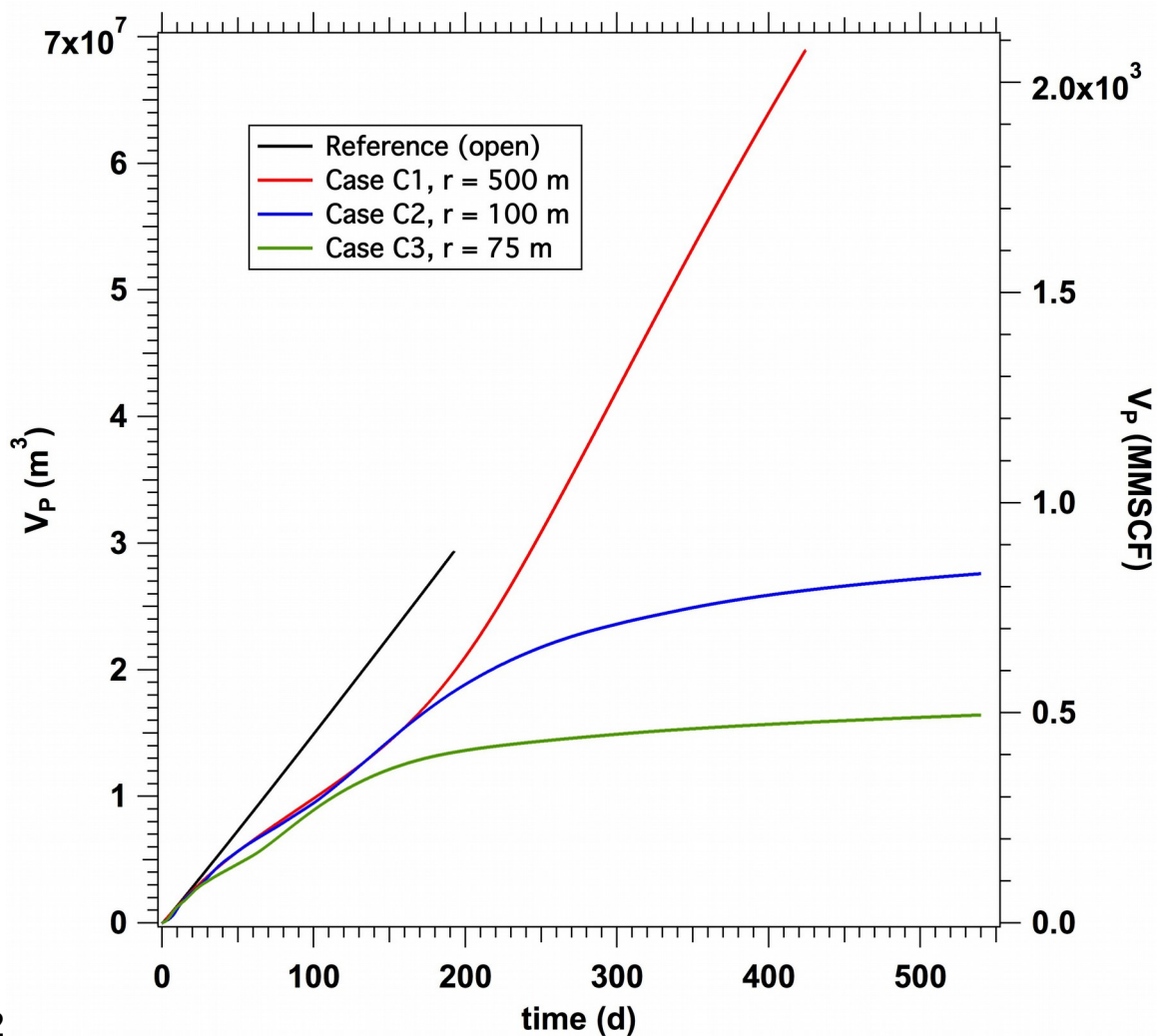


Figure 21. Provenance of gas in the production rate Q_p in Case C1 (A) and Case C3 (B).

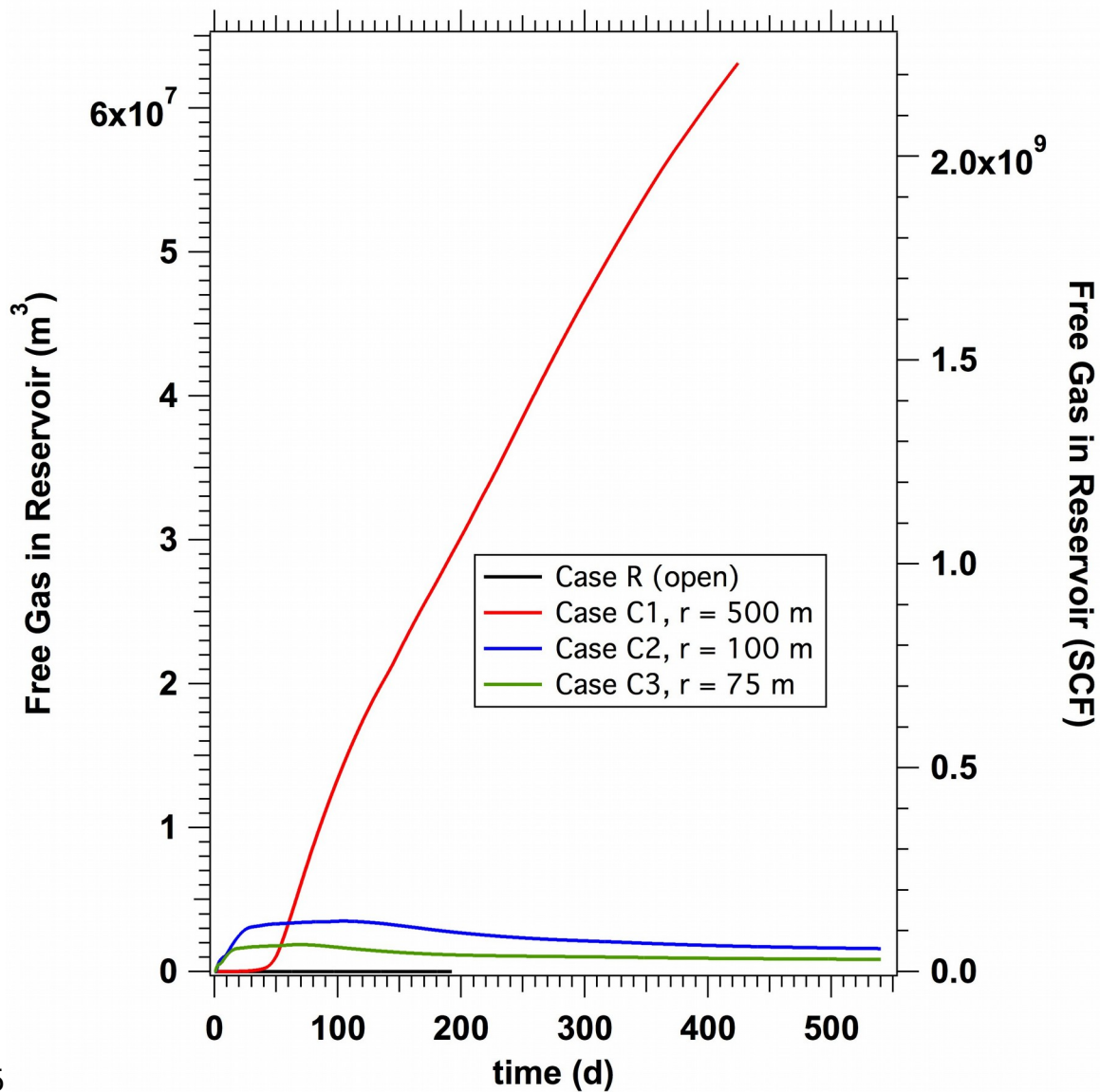
1369
1370
1371



1372
1373
1374
1375
1376
1377
1378
1379
1380

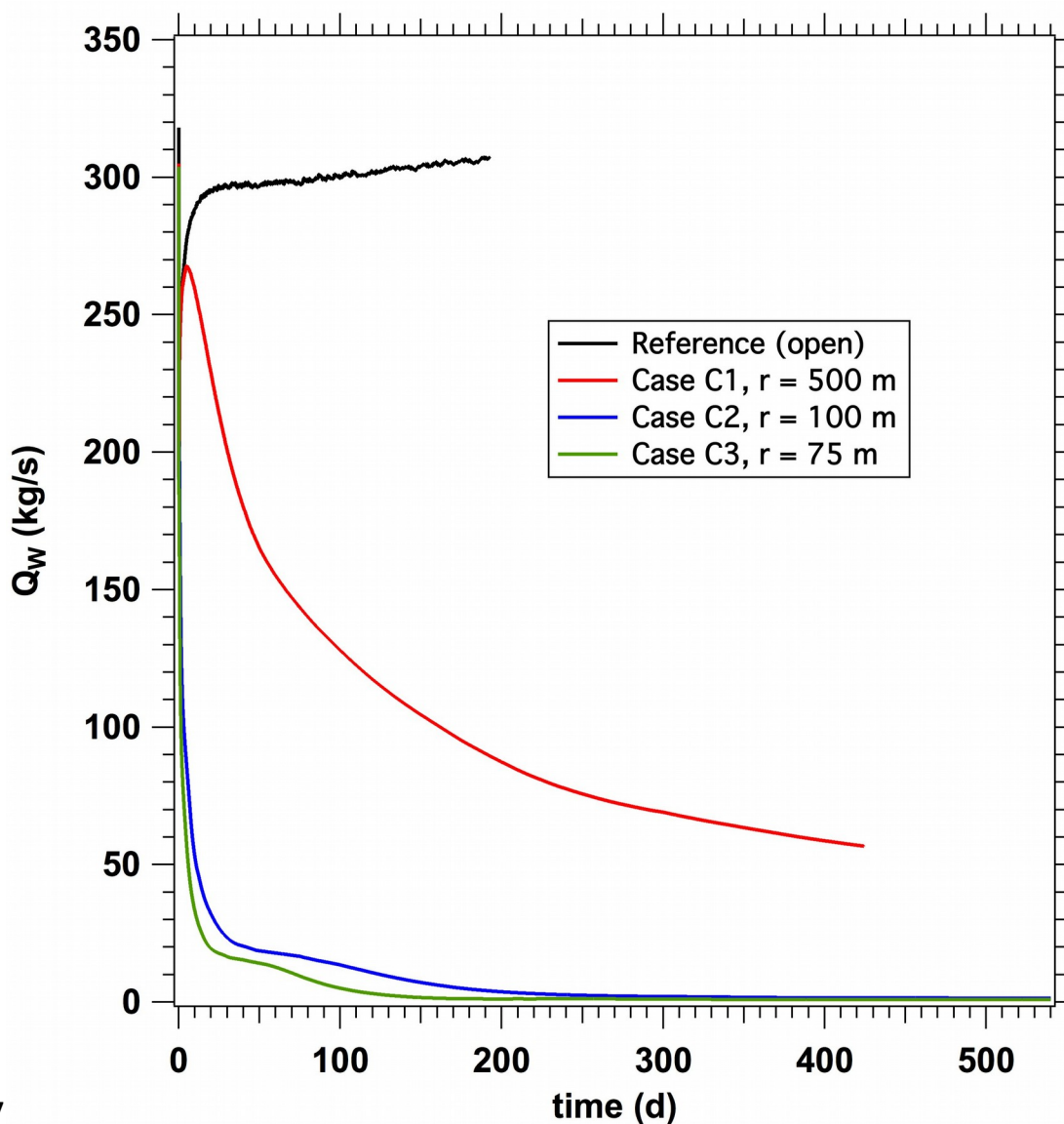
Figure 22. Cases C1, C2, C3 (closed systems): evolution of the volume of produced gas (V_p) over time during multi-well operations at Site NGHP-02-09 of the KG Basin. The V_p for the reference Case R (open system) is included for comparison.

1381
1382
1383
1384



1385
1386
1387 **Figure 23.** Cases C1, C2, C3 (closed systems): evolution of the volume of free gas in the
1388 reservoir (V_F) over time during multi-well operations at Site NGHP-02-09 of the KG Basin. The
1389 V_F for the reference Case R (open system) that is included for comparison is significantly
1390 smaller than for any other case.
1391
1392
1393

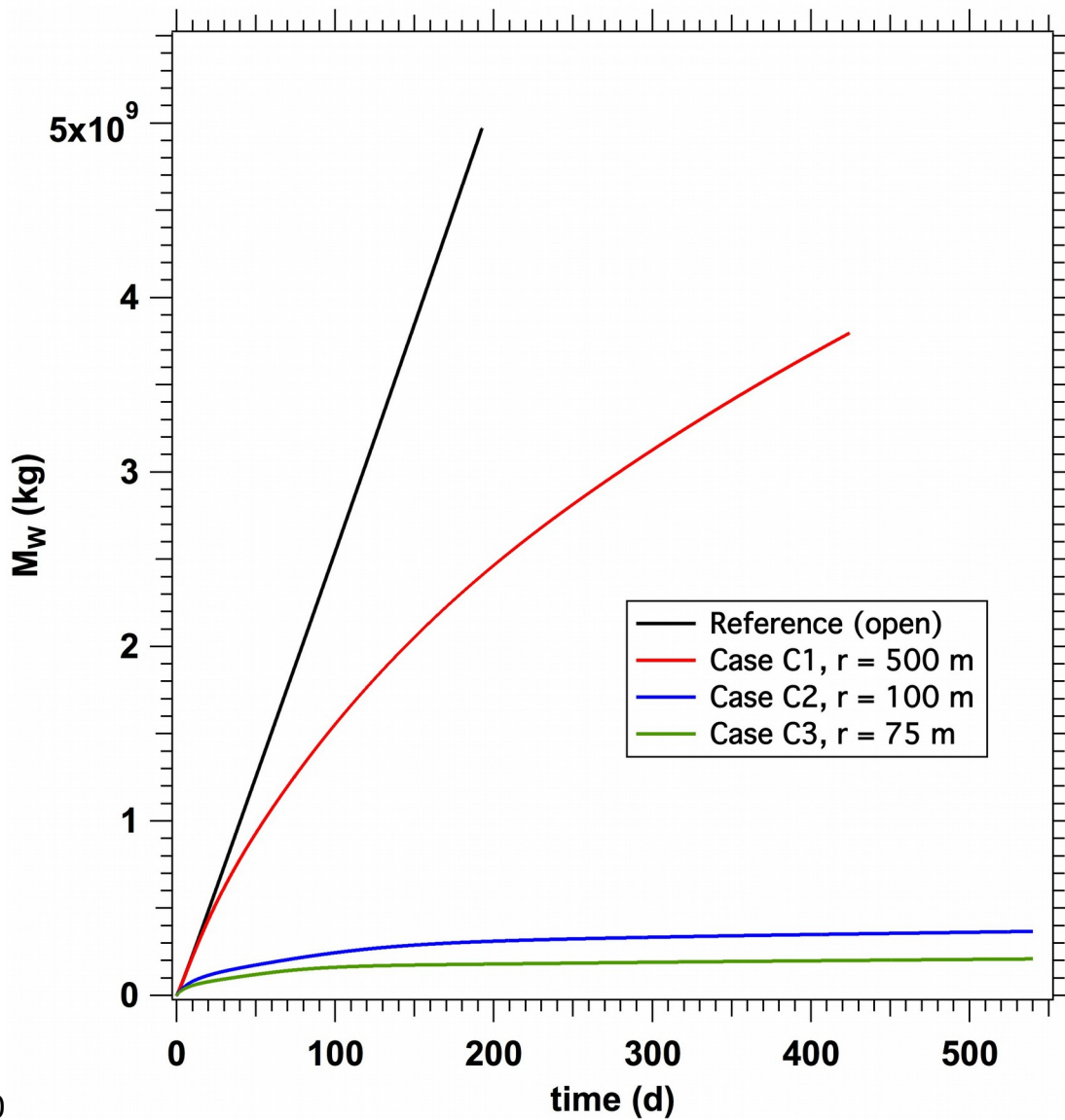
1394
1395
1396



1397
1398
1399
1400
1401
1402
1403
1404
1405
1406

Figure 24. Cases C1, C2, C3 (closed systems): evolution of the mass rate of water production (Q_w) over time during multi-well operations at Site NGHP-02-09 of the KG Basin. The Q_w for the reference Case R (open system) that is included for comparison has a distinctly different behavior.

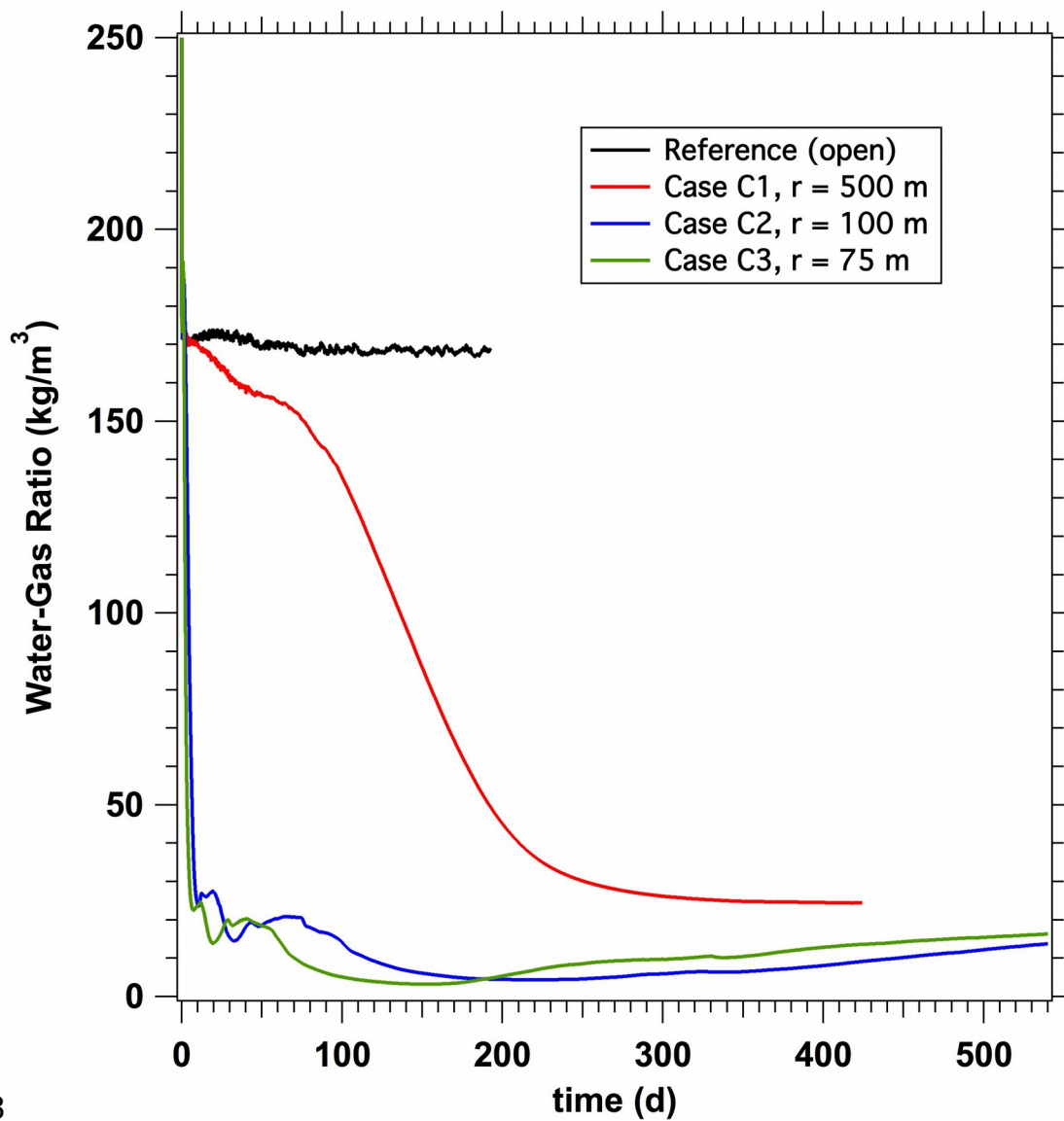
1407
1408
1409



1410
1411
1412
1413
1414
1415
1416
1417
1418
1419

Figure 25. Cases C1, C2, C3 (closed systems): evolution of the cumulative mass of produced water (M_w) over time during multi-well operations at Site NGHP-02-09 of the KG Basin. The M_w for the reference Case R (open system) that is included for comparison is significantly larger than in any other case.

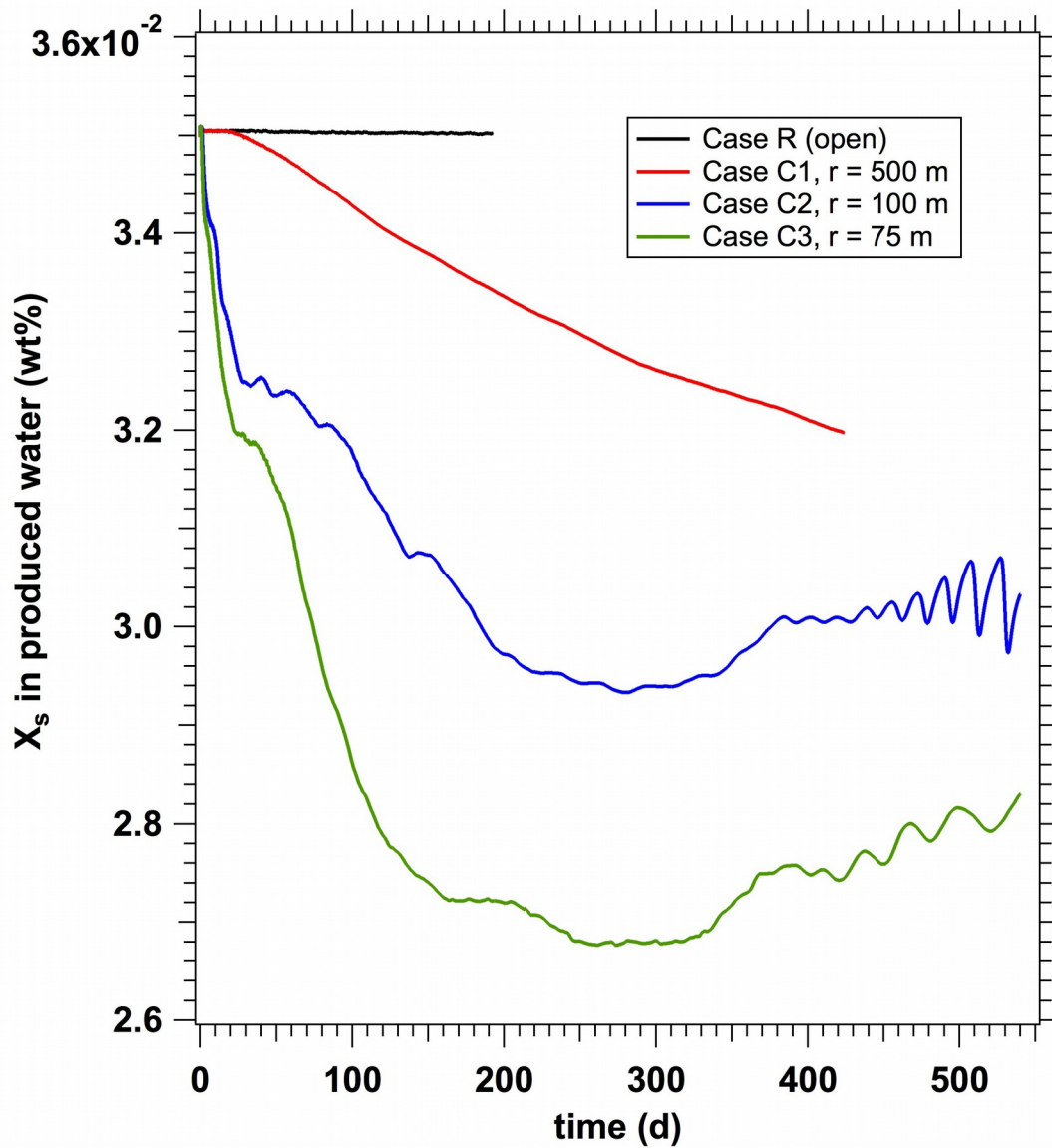
1420
1421
1422



1423
1424
1425
1426
1427
1428
1429
1430
1431

Figure 26. Cases C1, C2, C3 (closed systems): evolution of the water-to-gas ratio (*WGR*) over time during multi-well operations at Site NGHP-02-09 of the KG Basin. Note the different behavior of the *WGR* for the reference Case R (open system) that is included for comparison.

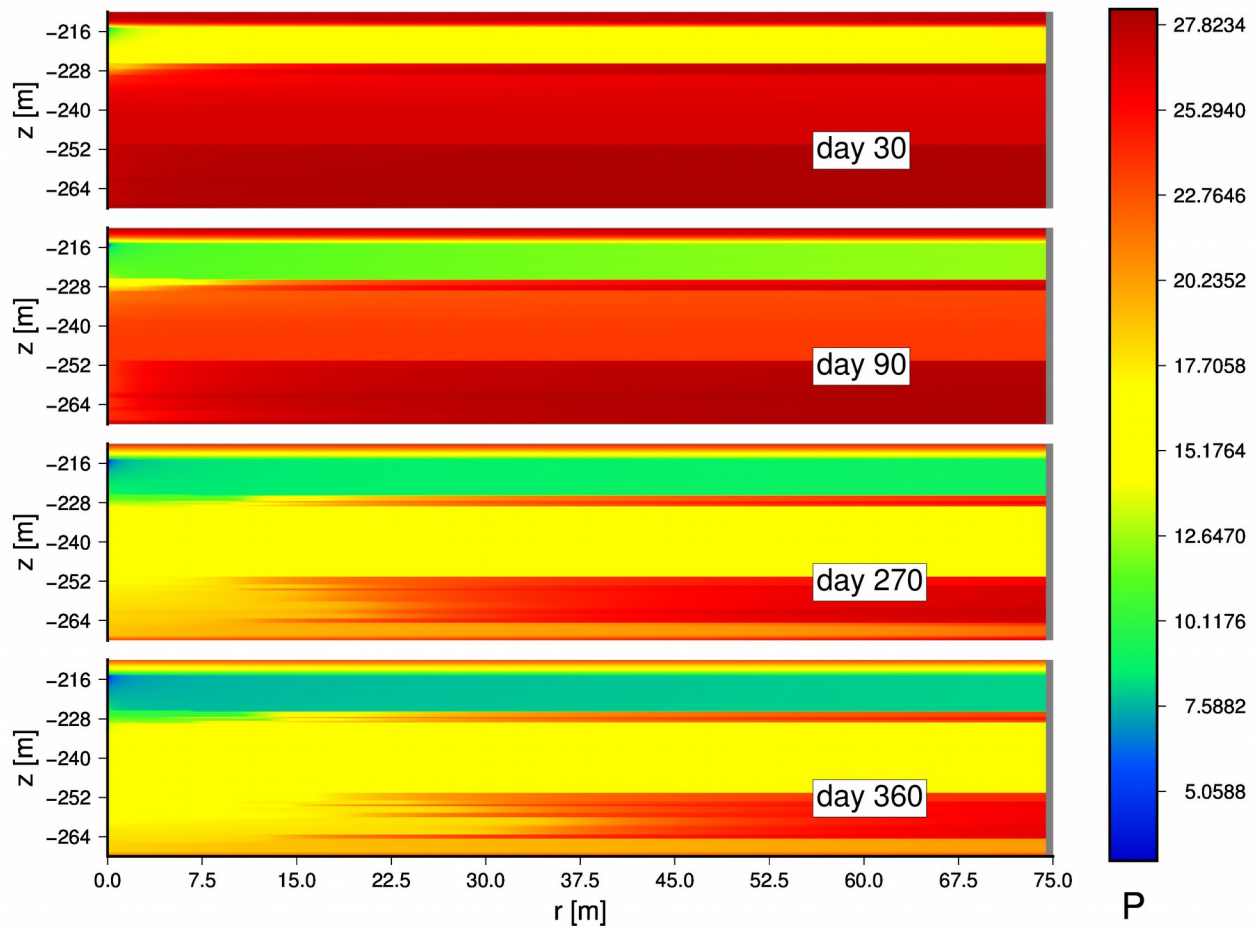
1432
1433
1434



1435
1436
1437
1438
1439
1440
1441
1442
1443
1444

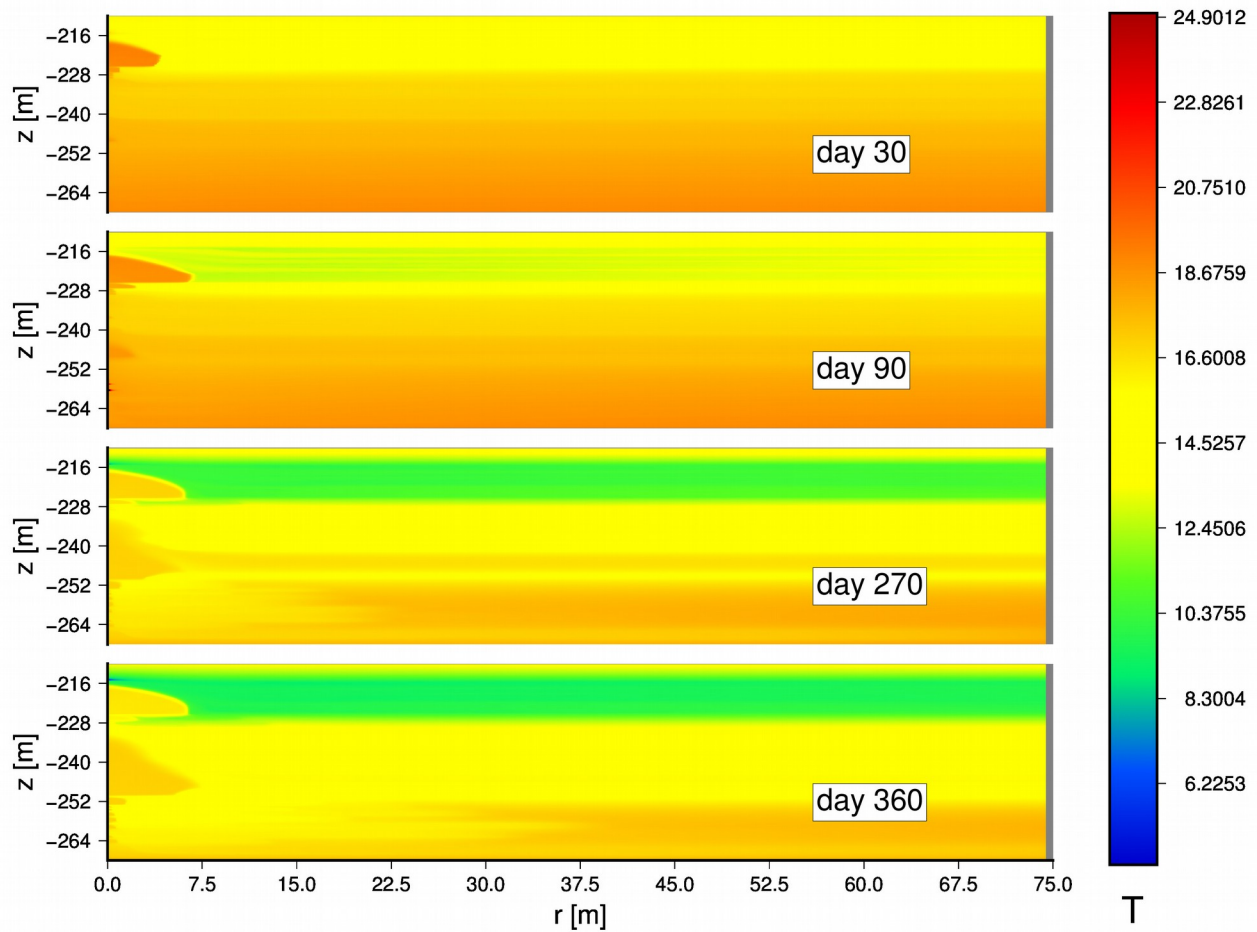
Figure 27. Cases C1, C2, C3 (closed system): evolution of the salt mass fraction in the produced water (X_s) over time during multi-well operations at Site NGHP-02-09 of the KG Basin. Note the different behavior of the X_s in the reference Case R (open system) that is included for comparison.

1445
1446
1447



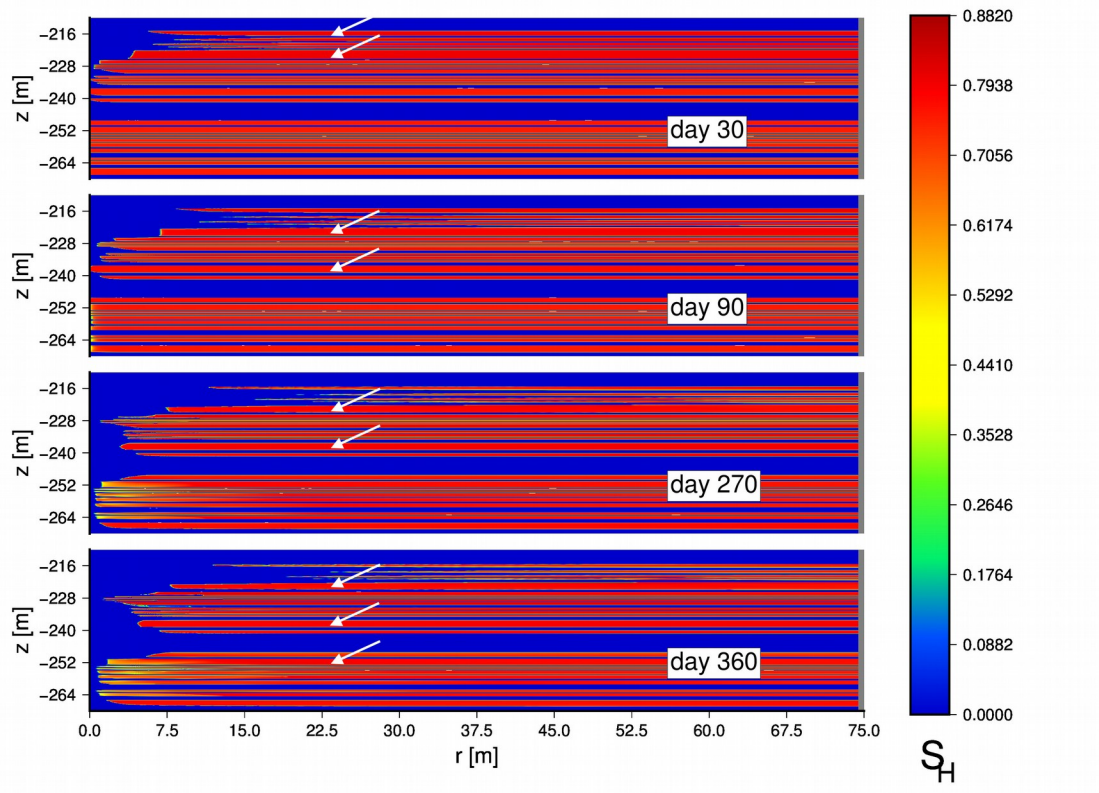
1448
1449
1450
1451 **Figure 28.** Case C1: Evolution of pressure (in MPa) distribution in the system during multi-well
1452 production operations at Site NGHP-02-09 of the KG Basin ($P_w = 3$ MPa).
1453
1454
1455

1456
1457
1458



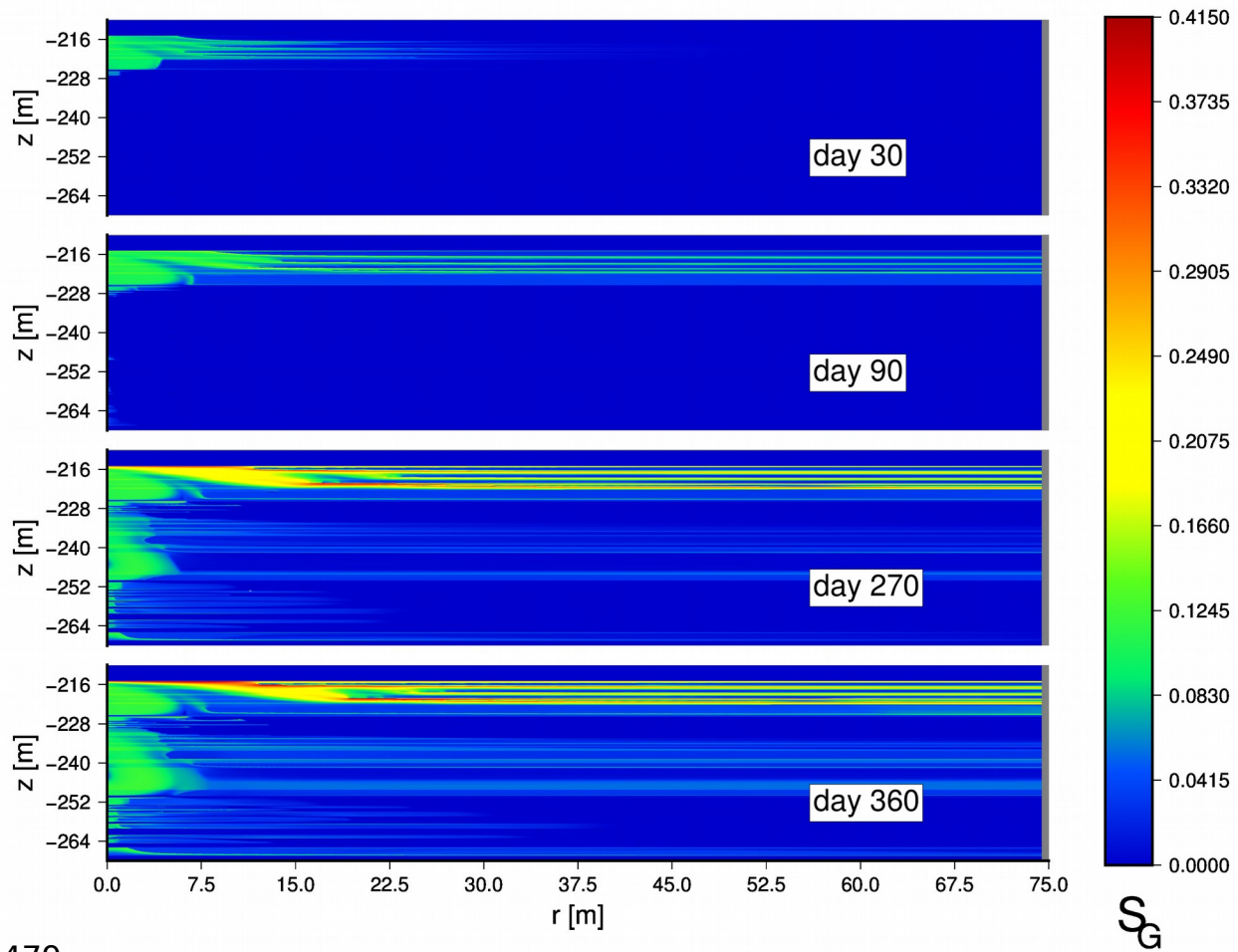
1459
1460
1461 **Figure 29.** Case C1: Evolution of temperature (in °C) distribution in the system during multi-
1462 well production operations at Site NGHP-02-09 of the KG Basin ($P_w = 3$ MPa).
1463
1464

1465
1466



1467
1468
1469
1470 **Figure 30.** Case C1: Evolution of the hydrate saturation S_H distribution in the system during
1471 multi-well production operations at Site NGHP-02-09 of the KG Basin ($P_w = 3$ MPa). Arrows
1472 indicate hydrate layers with $S_H > 0.75$.
1473
1474
1475

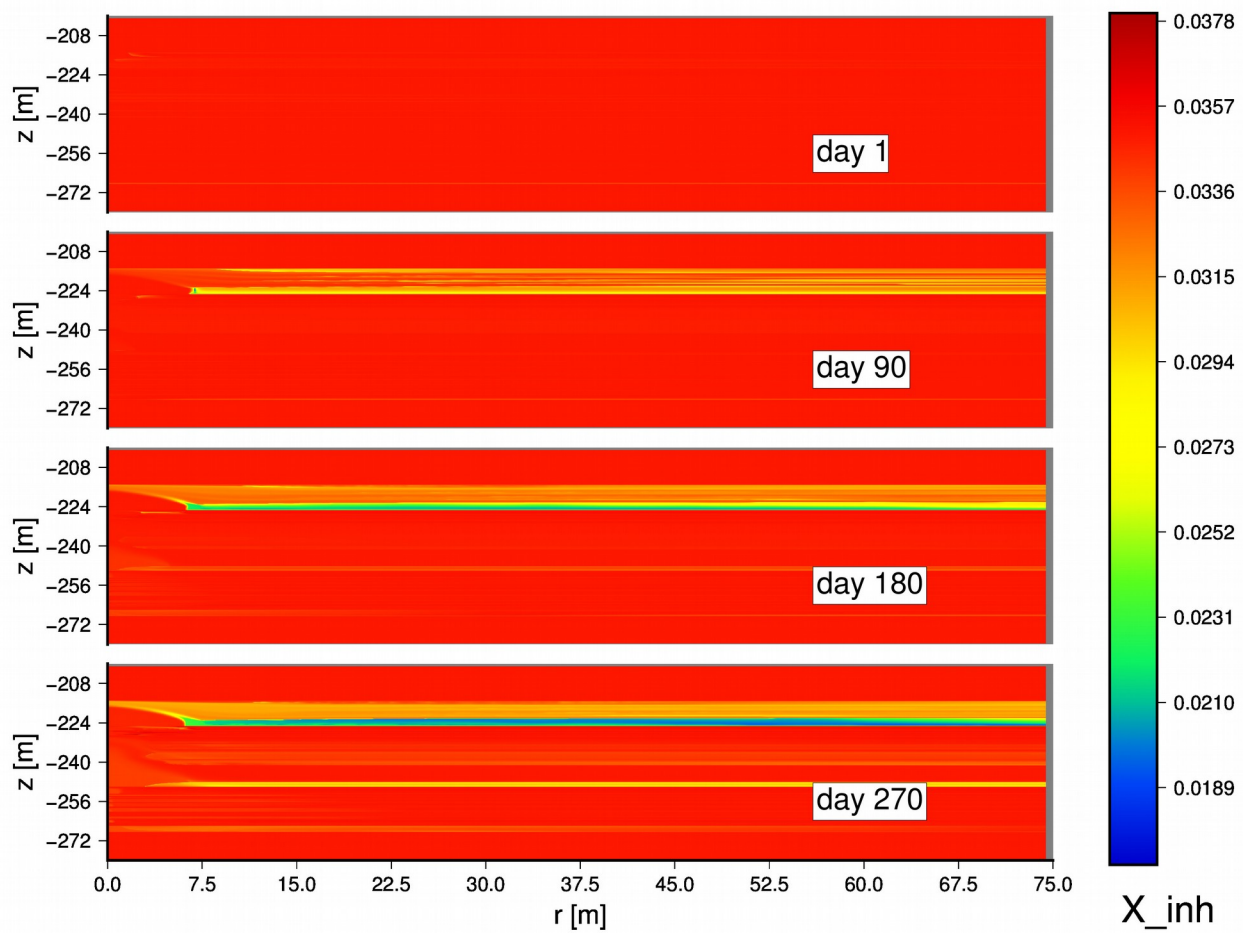
1476
1477
1478



1479
1480
1481
1482
1483
1484
1485

Figure 31. Case C1: Evolution of the gas saturation S_G distribution in the system during multi-well production operations at Site NGHP-02-09 of the KG Basin ($P_w = 3$ MPa).

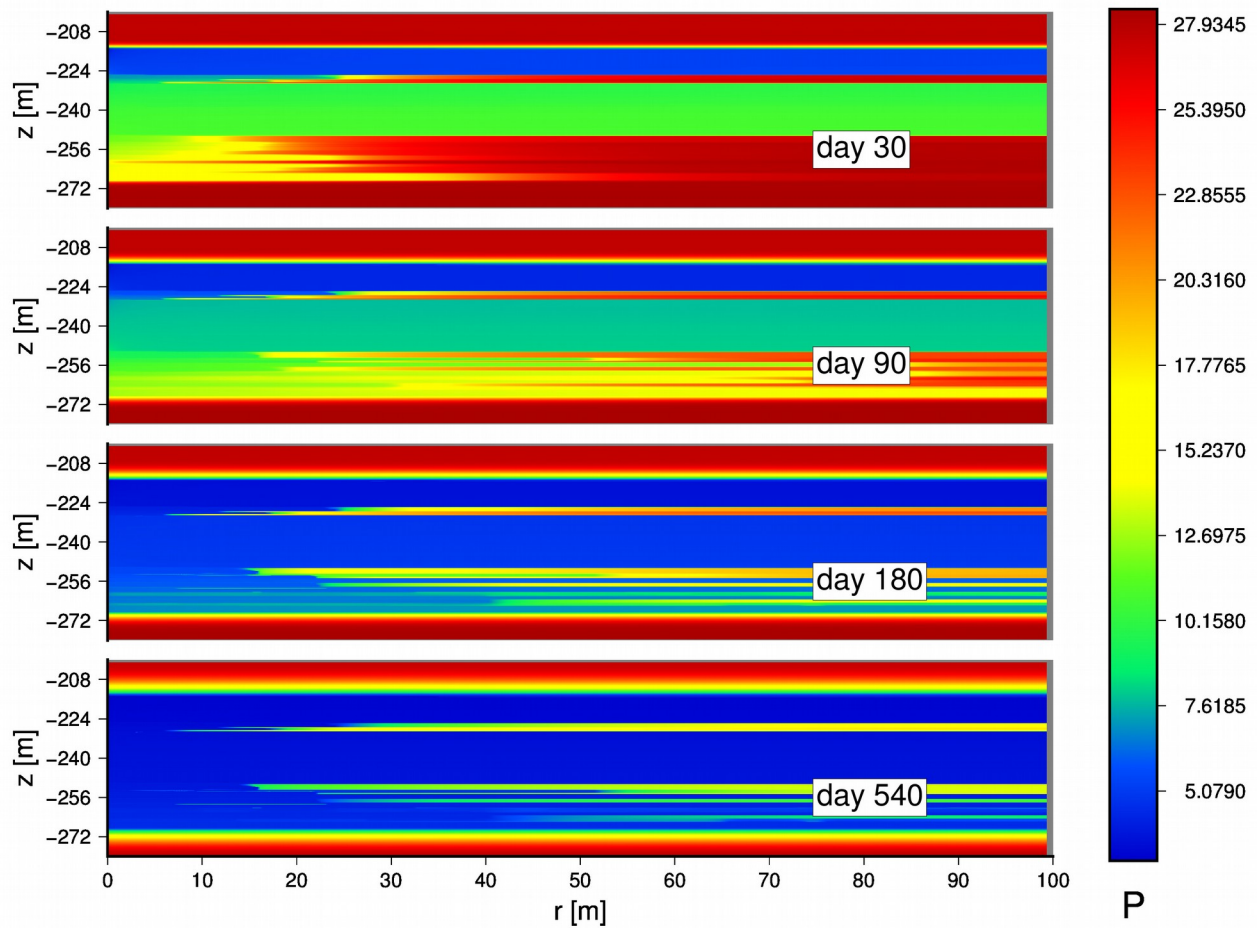
1486
1487
1488



1489
1490
1491
1492
1493
1494

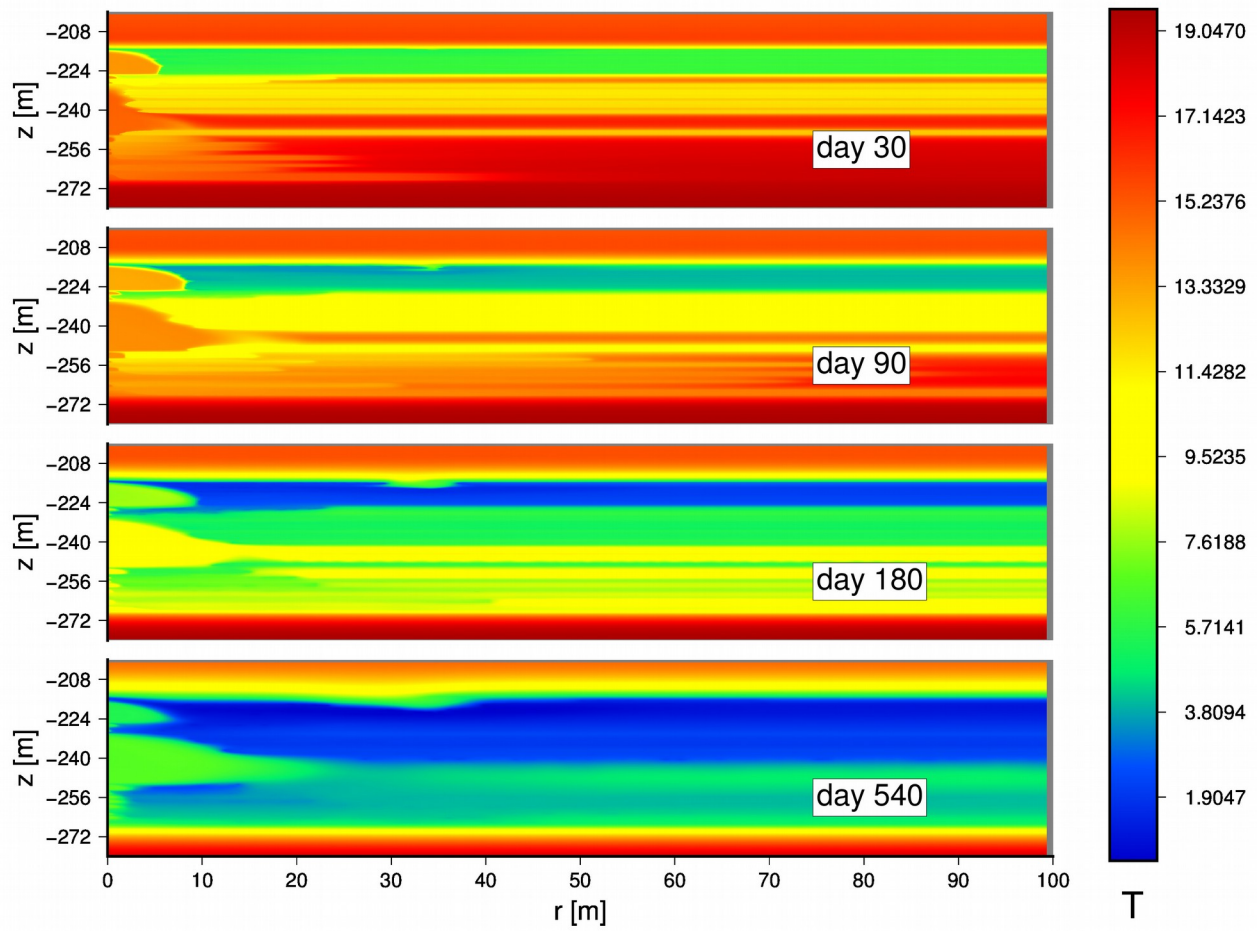
Figure 32. Case C1: Evolution of the distribution of the salt mass fraction X_s in the aqueous phase of the system during multi-well production operations at Site NGHP-02-09 of the KG Basin ($P_w = 3$ MPa).

1495
1496
1497



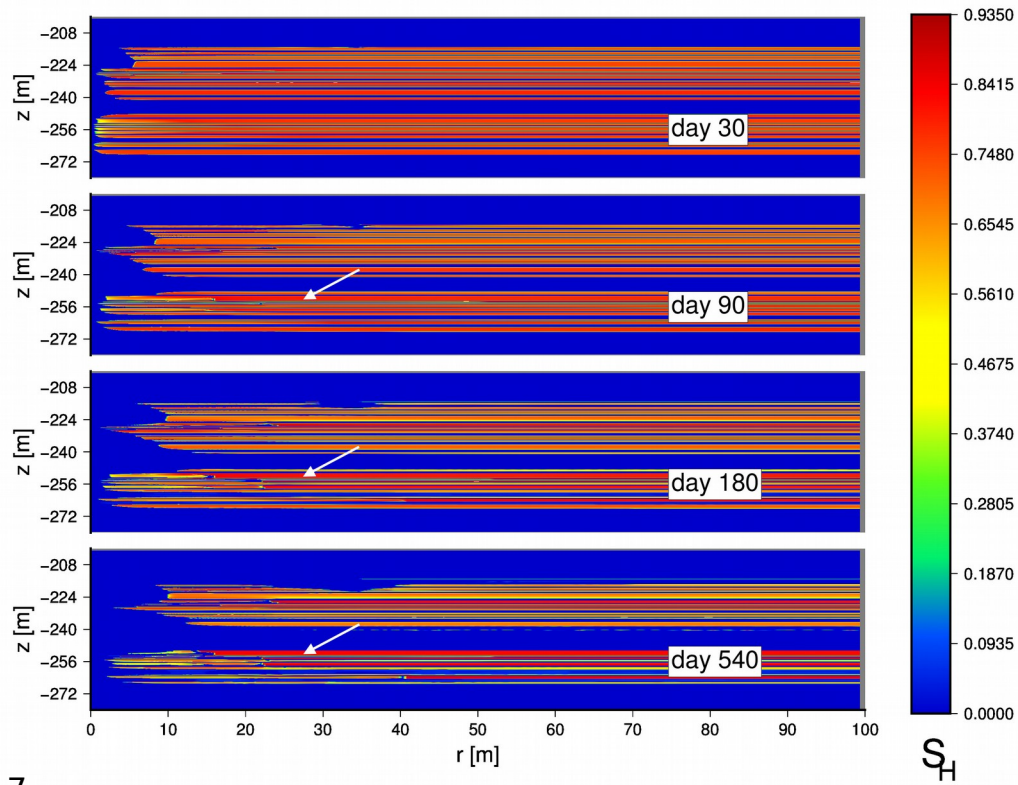
1498
1499
1500 **Figure 33.** Case C2: Evolution of pressure (in MPa) distribution in the system during multi-well
1501 production operations at Site NGHP-02-09 of the KG Basin ($P_w = 3$ MPa).
1502
1503
1504

1505
1506
1507



1508
1509
1510 **Figure 34.** Case C2: Evolution of temperature (in °C) distribution in the system during multi-
1511 well production operations at Site NGHP-02-09 of the KG Basin ($P_w = 3$ MPa).
1512
1513

1514
1515
1516

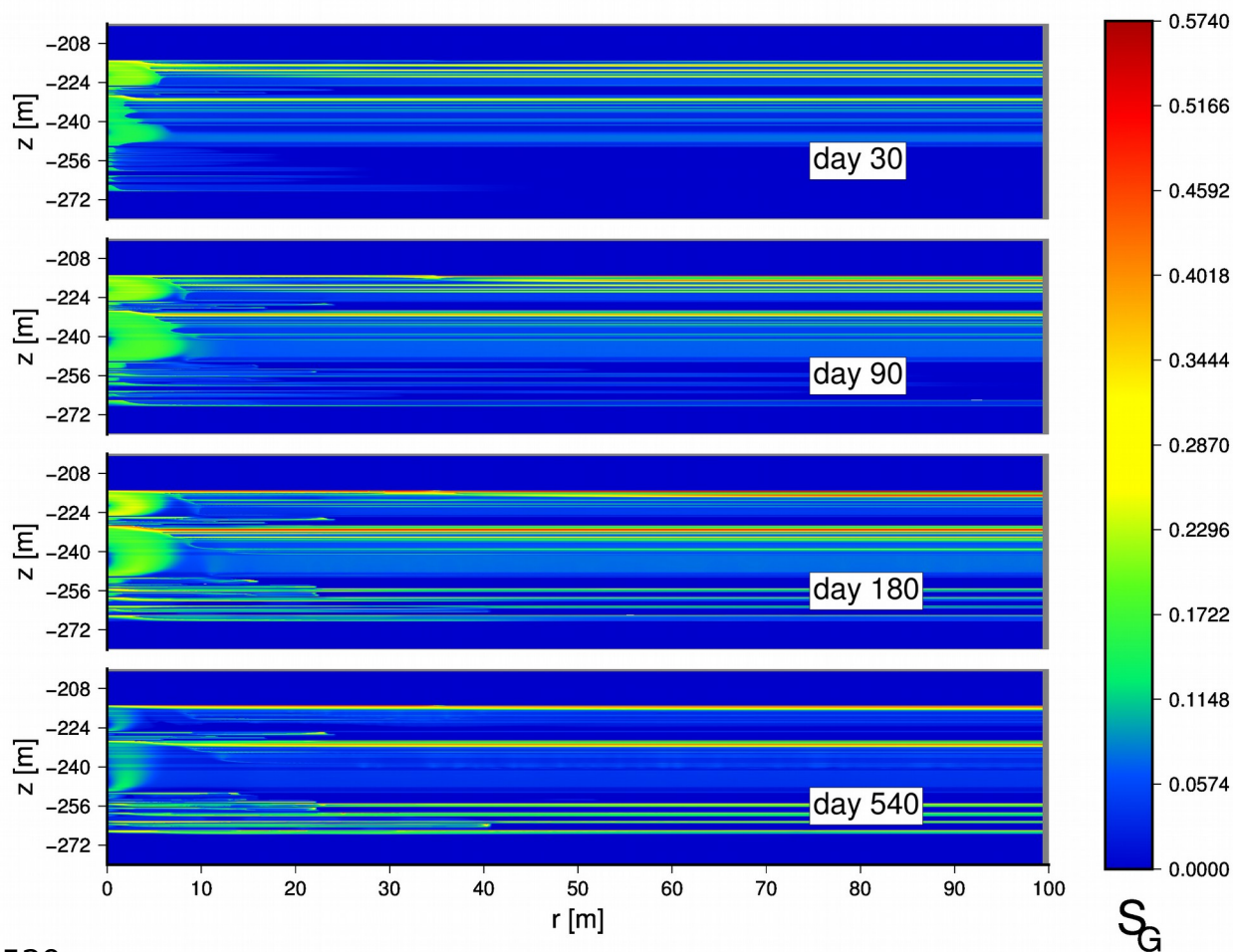


1517
1518

Figure 35. Case C2: Evolution of the hydrate saturation S_H distribution in the system during multi-well production operations at Site NGHP-02-09 of the KG Basin ($P_w = 3$ MPa). Arrows indicate hydrate layers with $S_H > 0.75$.

1522
1523
1524
1525

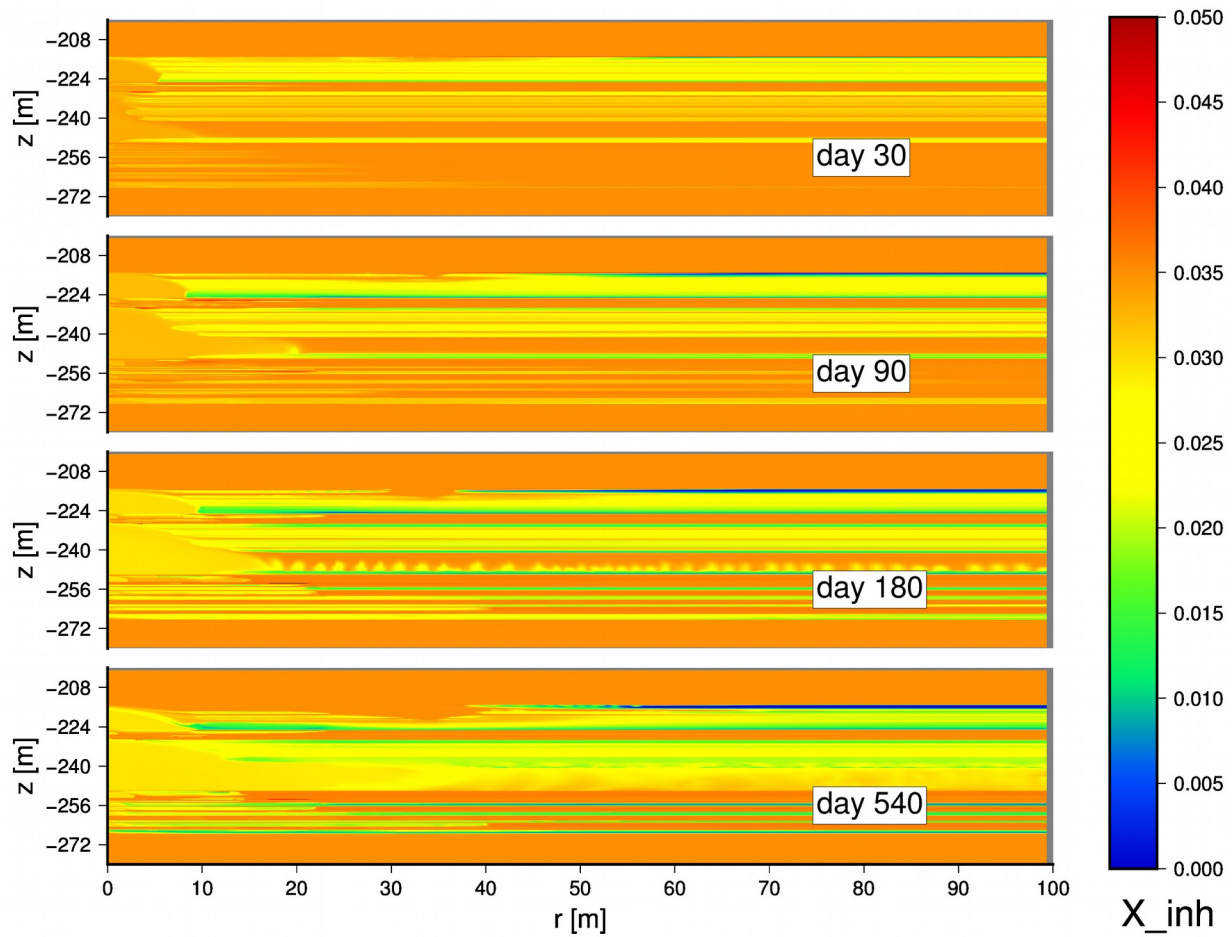
1526
1527
1528



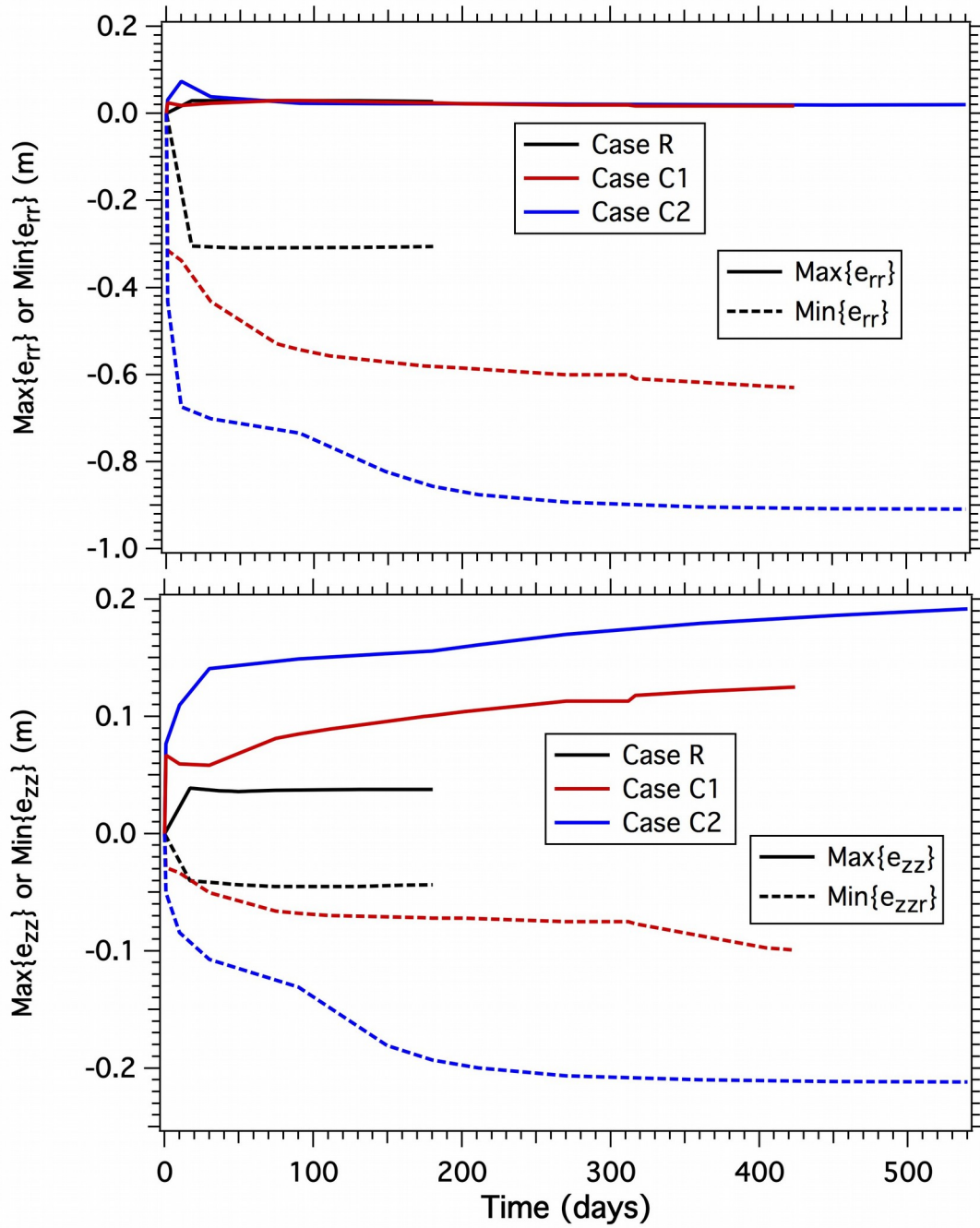
1529
1530
1531
1532
1533
1534
1535

Figure 36. Case C2: Evolution of the gas saturation S_G distribution in the system during multi-well production operations at Site NGHP-02-09 of the KG Basin ($P_w = 3$ MPa).

1536
1537
1538

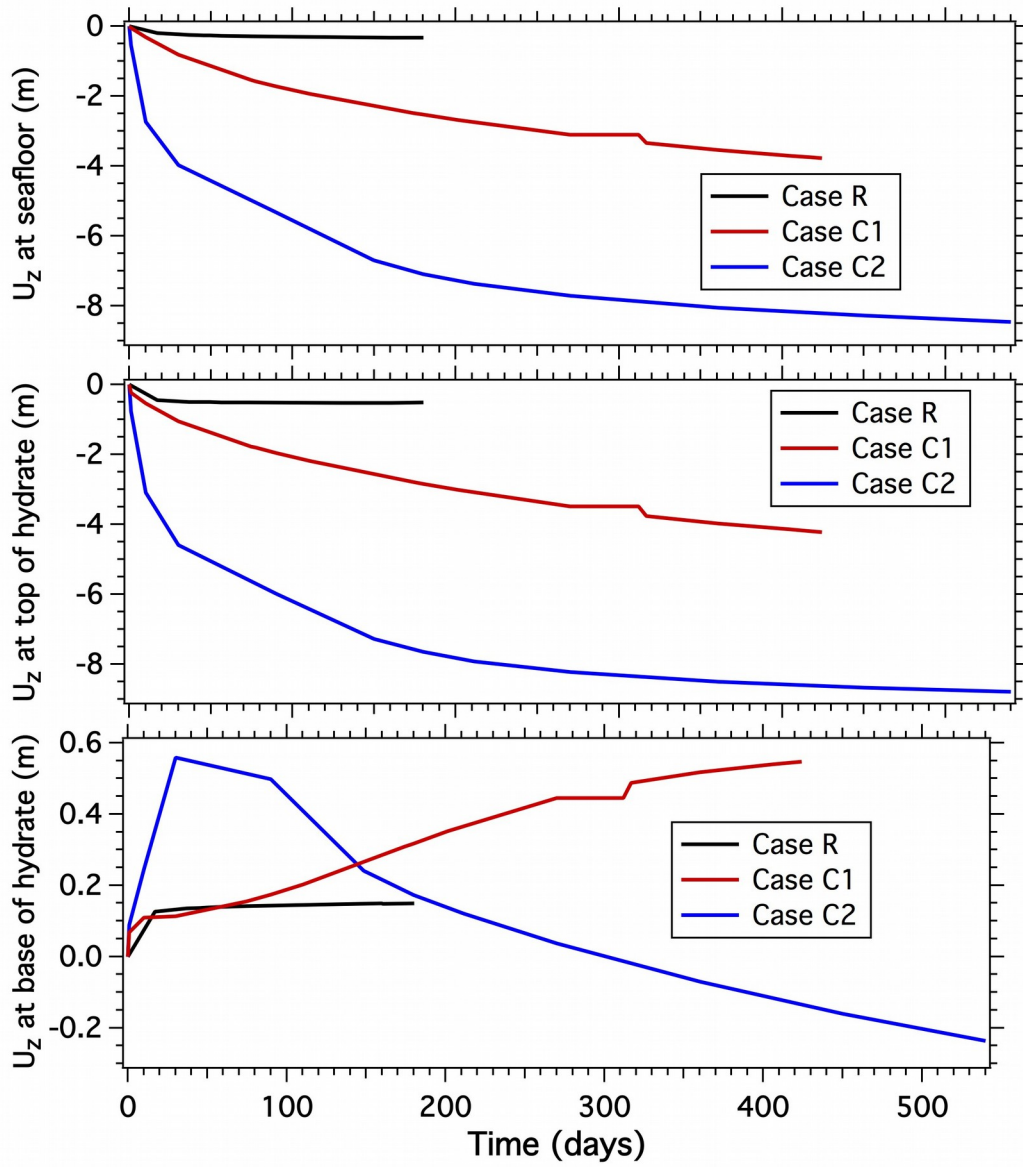


1539
1540
1541 **Figure 37.** Case C2: Evolution of the distribution of the salt mass fraction X_s in the aqueous
1542 phase of the system during multi-well production operations at Site NGHP-02-09 of the KG
1543 Basin ($P_w = 3$ MPa).
1544
1545
1546
1547



1548
 1549 **Figure 38.** Evolution of maximum and minimum strains ϵ_{zz} and ϵ_{rr} in the domain in Cases R,
 1550 C1 and C2.
 1551
 1552

1553
1554
1555
1556



1557
1558 **Figure 39.** Evolution of displacements u_z in the vicinity of the well in the domain in Cases R,
1559 C1 and C2.

1560
1561
1562

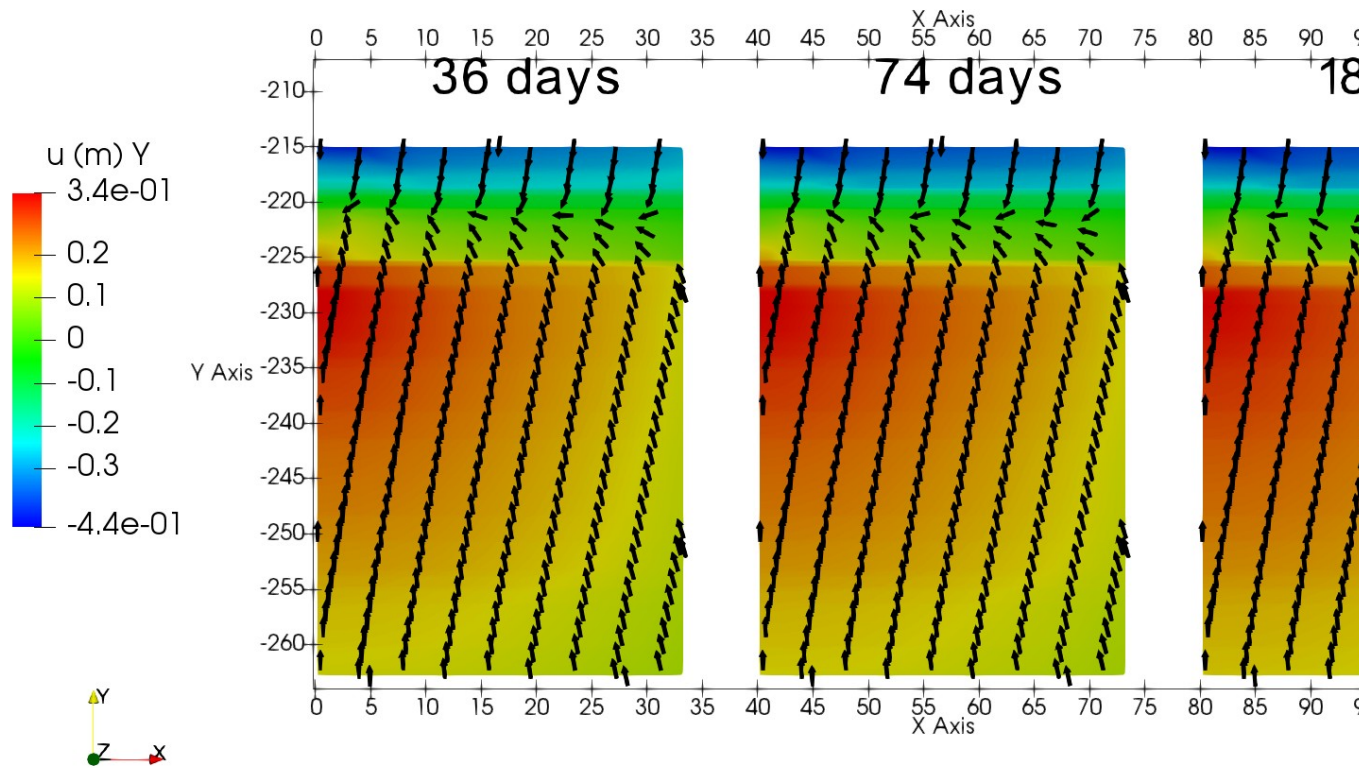


Figure 40: Evolution of the z-displacements (u_z) in Case R (open system). The arrows show the direction of the displacement. The z-coordinate (Y in the labels due to the rendering software) represents elevation in meters measured from the ocean floor and the x-coordinate represents the distance from the well. The two right images are offset by 40m and 80 m, respectively.

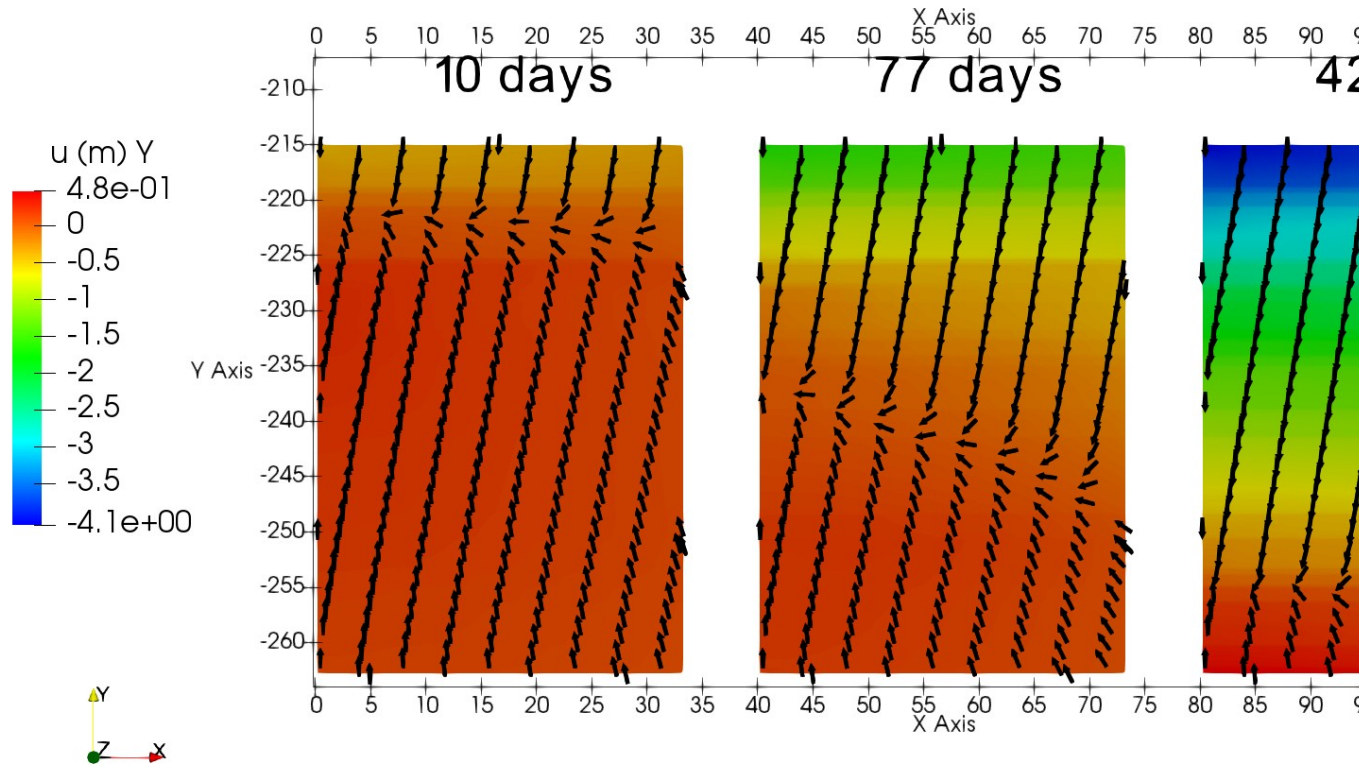


Figure 41: Evolution of the z-displacements (u_z) in Case C1 (closed system, $r = 500\text{m}$). The arrows show the direction of the displacement. The z-coordinate (Y in the labels due to the rendering software) represents elevation in meters measured from the ocean floor and the x-coordinate represents the distance from the well. The two right images are offset by 40m and 80 m, respectively.

1576
1577
1578

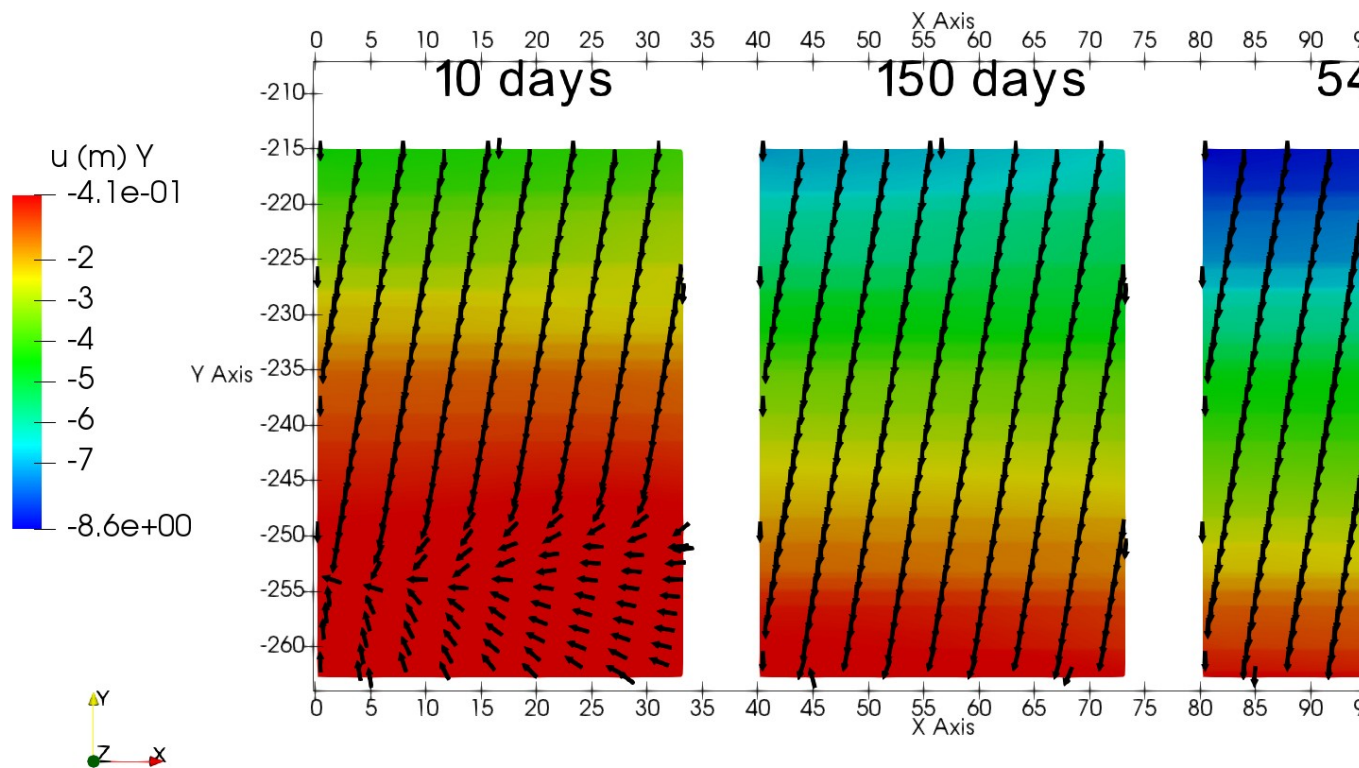
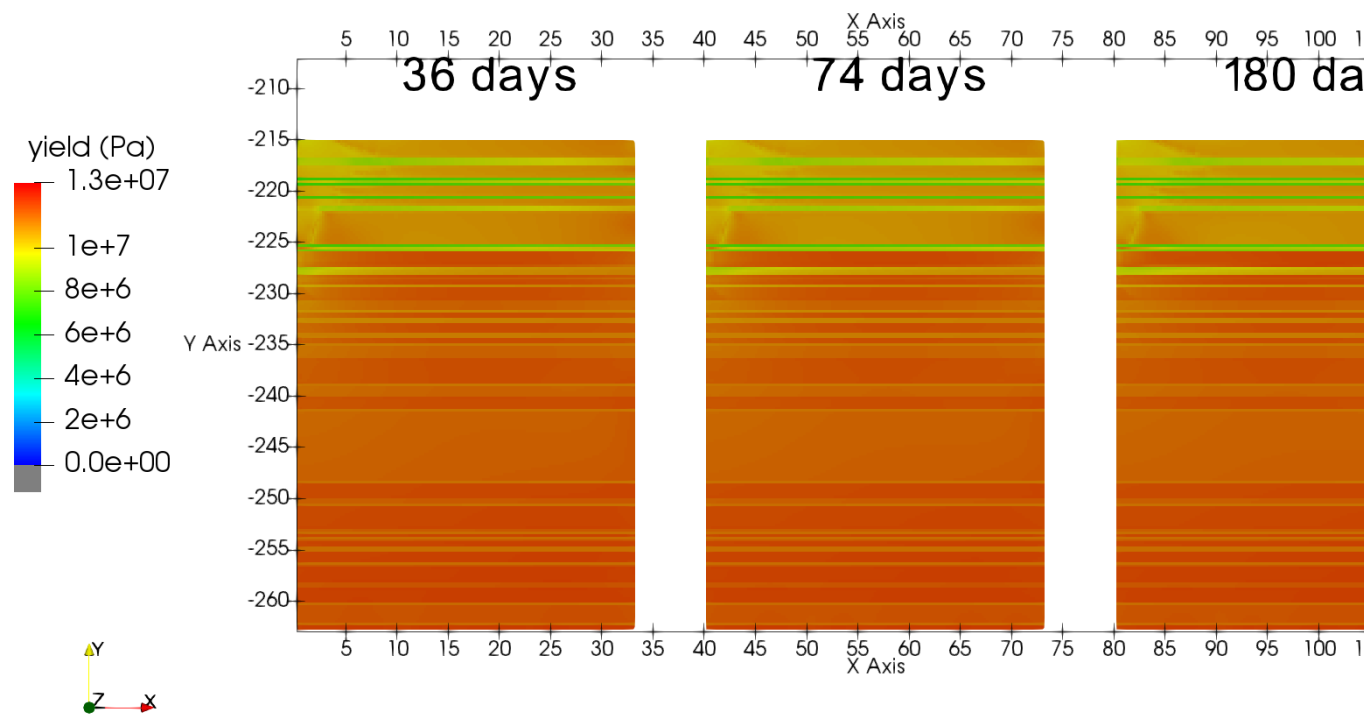
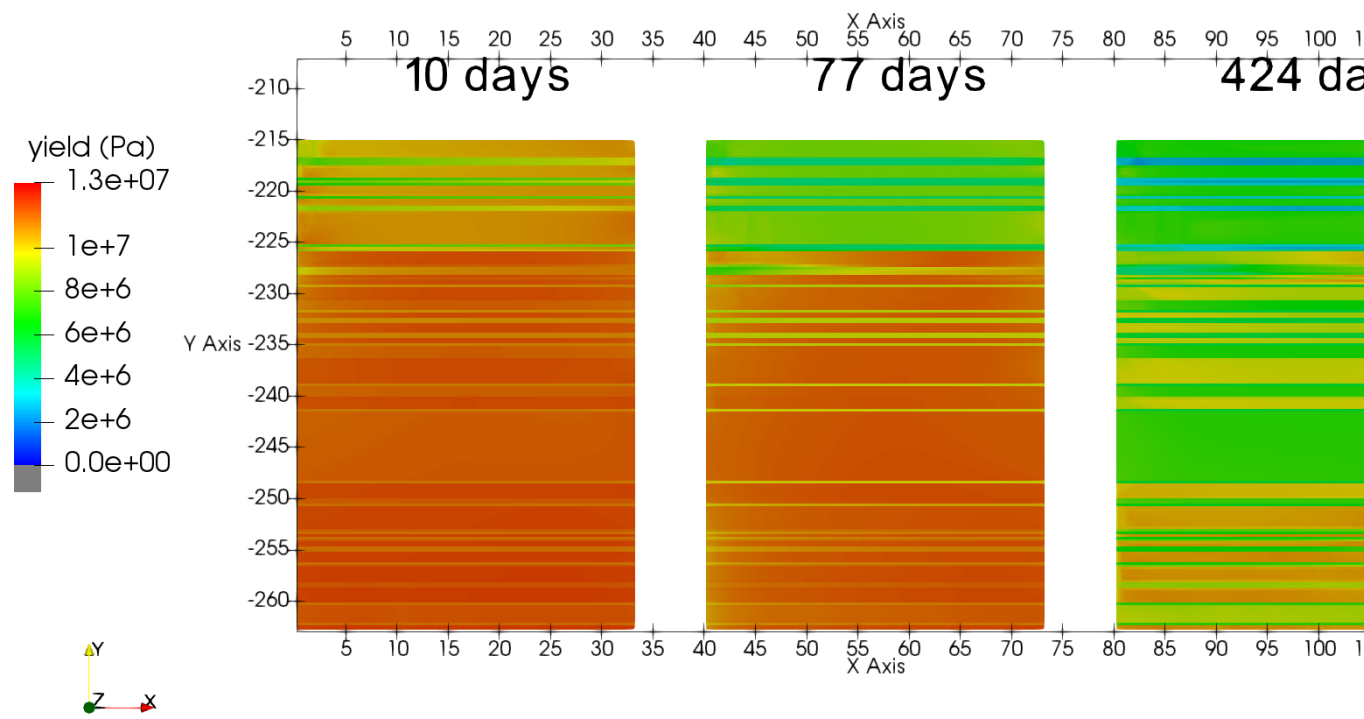


Figure 42: Evolution of the z-displacements (u_z) in Case C2 (closed system, $r = 100\text{m}$). The arrows show the direction of the displacement. The z-coordinate (Y in the labels due to the rendering software) represents elevation in meters measured from the ocean floor and the x-coordinate represents the distance from the well. The two right images are offset by 40m and 80 m, respectively.

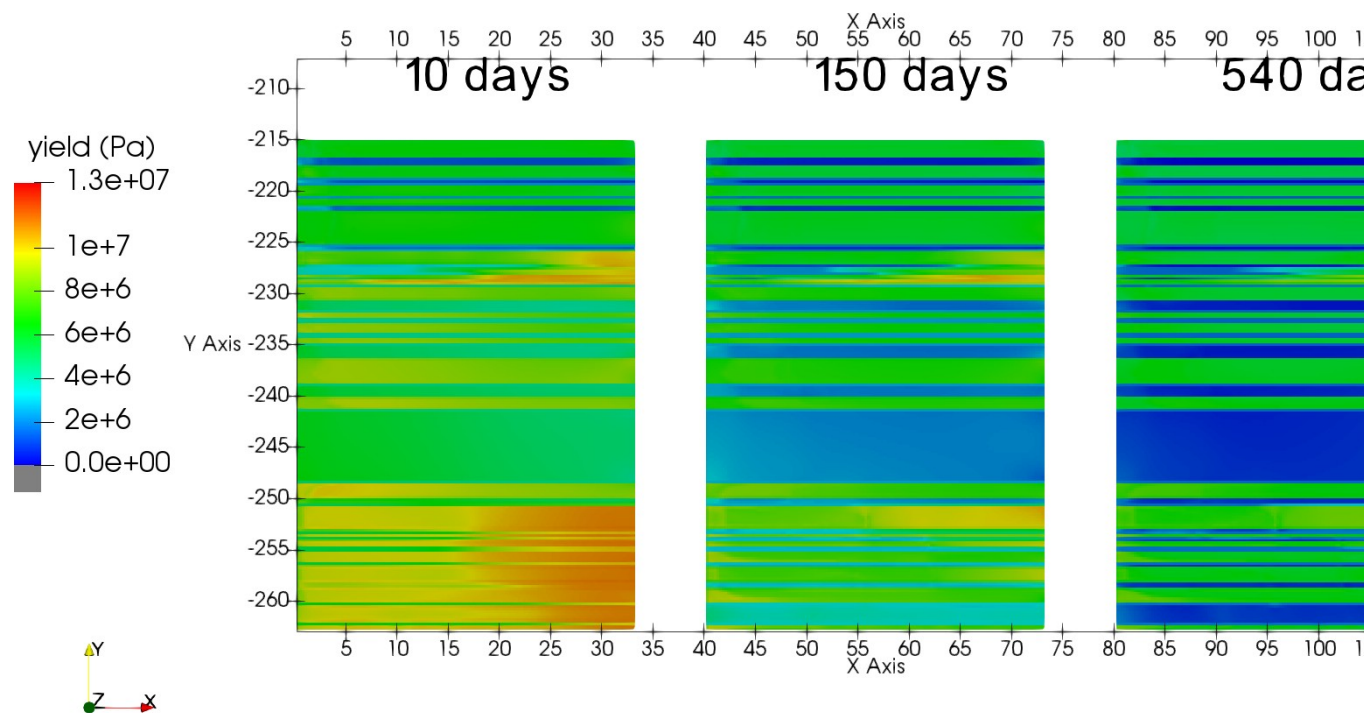
1585
1586



1587
1588Figure 43: Evolution of the Drucker Prager yield criterion in Case R (open system). The z-
1589coordinate (Y in the labels due to the rendering software) represents elevation in meters
1590measured from the ocean floor and the x-coordinate represents the distance from the well. The
1591two right images are offset by 40m and 80 m, respectively.
1592
1593



1594
1595Figure 44: Evolution of the Drucker Prager yield criterion in Case C1 (closed system, $r =$
1596500m). The z-coordinate (Y in the labels due to the rendering software) represents elevation in
1597meters measured from the ocean floor and the x-coordinate represents the distance from the
1598well. The two right images are offset by 40m and 80 m, respectively.
1599
1600
1601



1602
1603Figure 45: Evolution of the Drucker Prager yield criterion in Case C2 (closed system, $r =$
1604100m). The z-coordinate (Y in the labels due to the rendering software) represents elevation in
1605meters measured from the ocean floor and the x-coordinate represents the distance from the
1606well. The two right images are offset by 40m and 80 m, respectively. In this case, by the end of
1607the simulated production time the yield criterion goes below zero in the region encircled in red
1608and colored by gray in the color range.

1609
1610
1611
1612
1613